Universiteit Utrecht

Master of Earth Sciences, Graduate School of Geosciences

MSc Thesis - Earth Surface and Water

Hypsometric characterization of the Dutch Wadden Sea tidal systems and development of intertidal flats under relative sea-level rise

First examiner:
Prof. dr. Maarten G. Kleinhans

Candidate:
Brechtje van Amstel, 6593615

Second examiner:
Dr. Maarten van der Vegt

In cooperation with:
NIOZ

April 2024

Abstract

The Wadden Sea contains the largest contiguous area of intertidal flats in the world, stretching along the coasts of the Netherlands, Germany, and Denmark, and is marked as a UNESCO World Heritage Site due to its unique ecological value. With rising sea levels, the intertidal habitats are at risk of drowning. However, it remains unclear how the morphology within the tidal basins will react.

In this study, detailed hypsometric characterization of the Dutch Wadden Sea is carried out to gain a better understanding of the dynamics within these tidal basins. Hypsometry is the distribution of elevation over area within a morphological unit. The shape of this curve can be parameterized and area, volume, and height of depth zones can be calculated. Therefore hypsometric characterization allows for strong data reduction. In estuary research, predictability to the pattern in concavity-convexity of the curve has been found. This raises the question whether similar predictability is present for tidal basins.

Results show that curve convexity and presence of intertidal habitats increase from west to east and from the inlet to the land. The mean height of the flats decreases away from the inlet. Furthermore, the pattern of intertidal flat area shows a negative exponential relationship with basin size between and within tidal basins. These patterns provide insight into the distribution of intertidal habitats in the Dutch Wadden Sea and can be linked to changes in tidal range, sediment availability, wave energy, and basin size. This is a starting point for further temporal analysis and for finding predictability in the shape of hypsometric distributions.

Moreover, the proportion of tidal flat area is predominantly dependent on basin size, suggesting a certain degree of self-organization in the underlying formation processes leading to a scale-dependence of this proportion. This argues against the assumption that the Marsdiep and Vlie basins would grow to exhibit a proportion of intertidal flat area similar to that of the small basins in the eastern Wadden Sea under sufficient sediment supply. This is often considered an equilibrium condition and strongly influences the magnitude of predicted sediment deficits and drowning of tidal flats. Predominant scale-dependency implies lower sediment deficits and less drowning in the western Wadden Sea than assumed in previous studies.

Contents

Nomenclature

Ab Total area of basin (km^2)

Af Area of intertidal flats (km^2)

Hf Mean height of intertidal flats relative to mean low water ($+mMLW$)

MHW Mean High Water($+mNAP$)

MLW Mean Low Water ($+mNAP$)

MTR Mean Tidal Range (m)

TP Volume of tidal prism (m^3)

Vb Total volume of sand in the basin (m^3)

Vf Total volume of sand stored in intertidal flats (m^3)

1. Introduction

The interaction between water, sediment, and biological processes in the Wadden Sea creates a unique biogeomorphological system, which was listed as a UNESCO World Heritage Site in 2009. The trilateral Wadden Sea contains the largest contiguous area of tidal flats in the world. The intertidal flats are of high ecological value as they are important habitats for benthic species creating an important feeding and resting place for migratory waterbirds on the East Atlantic Flyway (Blew & Südbeck, 2005).

With rising sea levels, intertidal flats in the tidal systems of the Wadden Sea are in danger of drowning (A. J. F. van der Spek, 2018). The abundance of benthic species, and thus the abundance of nutrition for various waterbirds, depends strongly on the elevation and extent of intertidal flats (Beukema, 2002). In terms of flood protection, intertidal flats play an important role in attenuating waves and sediment trapping so that the system can keep up with the RSLR (Borsje et al., 2011; Temmerman et al., 2013). In addition, the presence of tidal flats is positively correlated with the development of salt marshes, which in turn can significantly lower wave run-up at the coast during storms (Marin-Diaz et al., 2023). It is therefore of great importance to accurately assess the development of these intertidal flats under changing environmental conditions.

Until now, this has not been analysed on a more detailed scale within the tidal basins, but only on the scale of entire tidal basins. To accurately couple changes in intertidal habitat to changes in grain size and benthic species abundance and composition, a more detailed approach is preferable. As long-term modelling tools generally focus on a larger scale of entire tidal basins, the spatiotemporal development of intertidal flats within tidal basins on a more detailed scale is under-represented in modelling as well. A commonly used modelling approach in the Dutch Wadden Sea is the ASMITA model, which uses hypsometry to determine the area, average height, and volume of different depth zones over time.

Hypsometry is used to describe the elevation distribution in a (drainage) basin. The area hypsometric curve shows the distribution of elevation over the surface of the (drainage) basin and the integral of the hypsometric curves gives the volume percentage of a certain height percentage. Variables such as mean and median elevation can be easily determined and topographic characteristics can be compared between basins

(Horton, 1932).

Recently, a method has been found to predict hypsometric curve shape for cross-sections in estuaries from the typical tidal amplitude combined with geometric characteristics of the estuary (Leuven et al., 2018). This raises the question of whether the hypsometry of (parts of) tidal basins can also be estimated from physical parameters and whether trends in hypsometric curve shape can be linked to spatiotemporally changing physical conditions.

1.1. Research area: The Dutch Wadden Sea

The Wadden Sea extends along the coasts of the Netherlands, Germany, and Denmark and is separated from the North Sea by barrier islands. The Dutch part of the Wadden Sea consists of the following major components, from west to east; Texel Inlet, Eierlandse Gat Inlet, Vlie Inlet, Ameland Inlet, Frisian Inlet, and the Ems-Dollard estuary (Fig. 1.1). The area formed during several phases of ingression due to RSLR during the Holocene and sufficient sediment supply from erosion of the adjacent coastline. The accommodation space created, combined with flood dominance, induced landward sediment transport. The increased sedimentation led to the formation of intertidal flats and the shallowing of the basin, which then reduced the importance of flood dominance in the tidal cycle and therefore reduced sediment import. As a result, sediment transport eventually became net outward through the ebb channels around 3700 BP, but sediment that was stored on the tidal flats was left behind, and the Wadden Sea system emerged (A. van der Spek, 1994).

Waves entering the Dutch Wadden Sea are generated mainly locally in the North Sea basin. This, combined with large tidal prisms, results in tide-dominated features such as deep entrance channels and large ebb-tidal deltas (Hayes & FitzGerald, 2013). However, as the influence of wind-driven currents is strong enough to impose a large variability in the residual current, and can even change direction with strong southwesterly winds, the system can be classified as a mixed energy coast with dominant tidal influences (Hayes, 1979; Duran-Matute et al., 2014). The combination of mesotidal conditions and the significant influence of wind on residual currents results in sediment transport strongly influenced by wind-driven currents (Wang et al., 2012). A complex tidal flow pattern causes the mean tidal range to increase from 1.4 m in Marsdiep to 2.5 m in the Ems-Dollard estuary (Elias et al., 2012). The combination of these

wind-driven currents and the increasing tidal range causes the tidal divides between the basins to be located east of the centre of the barrier islands (Wang et al., 2011).

1.2. Anthropogenic influences

Two major human interventions have taken place in the Wadden Sea. Firstly, the Zuiderzee was closed by the construction of the Afsluitdijk in 1932 and secondly the Lauwerszee was closed of in 1969. These interventions disturbed the morphological equilibrium in the respective basins and as a result of the changed hydrodynamics, the sedimentation rate increased drastically (Elias et al., 2012).

In the eastern part of the Wadden Sea, the adaptation to a new equilibrium was rapid (A. J. F. van der Spek, 2018). The sediment budget in the eastern part of the Wadden Sea is limited in terms of accommodation space, as can be seen from the fact that the space created by subsidence is filled again quickly. The eastern part is expected to be able to keep up with the RSLR, but only until the maximum rate of sediment import is reached, after which a sediment deficit will occur.

The construction of the Afsluitdijk also resulted in an increase in sediment import in the western part of the Wadden Sea, but a new equilibrium has not yet been reached; the net import of sediment is still much higher than needed to compensate for the accommodation space created under the current RSLR (Wang et al., 2012). At present, the long-term averaged import of sediment is not sufficient to achieve a new morphodynamic equilibrium in the western part of the Wadden Sea, and this deficit will increase with rising sea levels. This sediment deficit could then lead to drowning of intertidal flats, the extent and timing of which strongly depend on the climate scenario evolving (A. J. F. van der Spek, 2018).

Although the dynamic nature of the system shows rapid adaptation to disturbances, projected rates of sea level rise, combined with subsidence due to gas and salt extraction, are expected to result in loss of intertidal flats (Huismans et al., 2022). Furthermore, major human interventions, such as the closure of the Zuiderzee and Lauwerszee, and coastal restoration projects outside the Wadden Sea, can have unprecedented impacts on the system.

The rise in sea level has already been measured since 1850 (Wahl et al., 2013) in the Dutch Wadden Sea. The trend until 1990 was about 1.8 mm/yr and an accelerated

rate of 3mm/yr has been observed in the period between 1993-2020 (Stolte et al., 2023). Future scenarios show that sea-level rise is expected to accelerate, which will have important consequences for the morphological and ecological functioning of the Wadden Sea system.

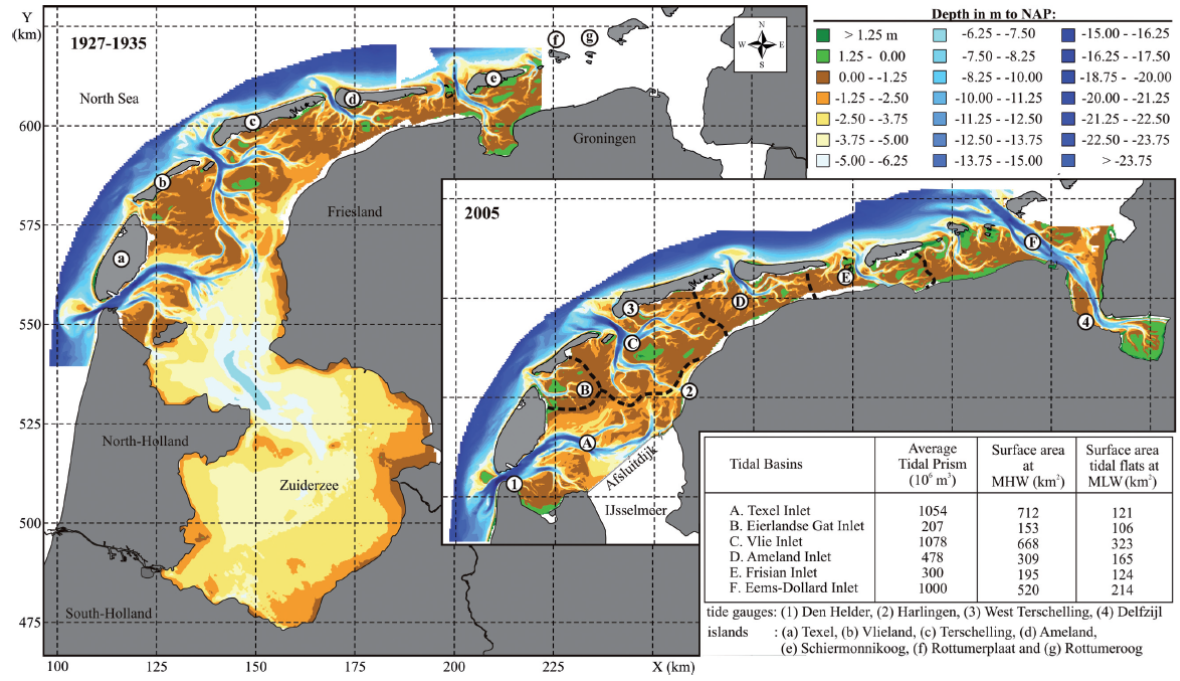

Figure 1.1: Overview map of the Dutch Wadden Sea for the years 1927-1935 in the large figure and 2005 in the smaller figure. The main characteristics are based on Louters and Gerritsen (2014).

Source: Elias et al. (2012)

1.3. Spatial patterns and future development of intertidal flats

The existence of intertidal flats depends on a delicate balance between the net sediment import and increasing accommodation space with relative sea level rise (RSLR). Changes in the relative sea level and the resulting hydrodynamics of the system will cause changes in the sediment budget. As described in A. J. F. van der Spek (2018), if the sediment budget cannot keep up with the rise in relative sea level, a sediment deficit in the system can lead to 'drowning' of the intertidal flats (Wang et al., 2012). Whether the system can keep up with rising sea level strongly depends on the rate of RSLR, in Huismans et al. (2022) this is expressed as the *critical rate of sea level rise*. The critical rate of RSLR at which this could happen may vary between basins as it depends on the morphological equilibrium and the morphological time scale in place (Lodder et al., 2019). In addition, the grain size distribution of the sediment also influences the critical rate. If the RSLR is constant and does not exceed this critical rate, a dynamic

equilibrium will be restored after a period of morphological response. However, if the rate is higher than the critical limit, 'drowning' will occur, including loss of tidal flats (Lodder et al., 2019). At different rates of RSLR, different percentages of height and area loss can be modeled, but it is still unclear how the tidal flats of the Wadden Sea will respond spatially on a more detailed scale within tidal basins to projected changes in hydrodynamics (A. J. F. van der Spek, 2018; Huismans et al., 2022).

Within the tidal basins, it is expected that the intertidal flats close to the inlet will remain intertidal, but that with distance from the inlet the drowning of the intertidal flats will be stronger due to a larger sand deficit (Huismans et al., 2022). Then a basin layout with an intertidal flood delta near the inlet surrounded by a subtidal lagoon with a possible increase in mud deposition would emerge. The mud deposition will depend on the energy conditions. In line with this hypothesis, based on knowledge of the Holocene formation of the system, intertidal flats along the western side of the watersheds are more vulnerable to drowning, as the distance from the inlet is greater (Huismans et al., 2022). However, it is also argued in Hofstede (2015) that intertidal flat drowning will start on the seaward side of the basins and continue further landward, as the larger central basin is more susceptible to drowning than the smaller sub-basins further landward. It is also mentioned that the morphodynamic developments during the early Holocene transgressions cannot be used for comparison with the current RSLR (Hofstede, 2015).

The eastern Wadden Sea shows effects of 'distance-to-inlet' close to the tidal divides; the tidal currents from the more western inlets arrive earlier at the tidal watershed than the currents from the more eastern inlet, which causes the shift of the tidal watersheds eastward (Wang et al., 2020). From satellite imagery, the western halves of the basins are described as sandy intertidal shoals with meandering channels and lower flats with more linear channels in the eastern half of the tidal basin. For the western Wadden Sea, a different history exists with stronger geological influences and underlying Pleistocene deposits that are dominant in morphology. Therefore, it is expected that there are large scale differences between the western and eastern Wadden Sea when it comes to contrasting basin halves.

A first approach to spatial variation in the development of intertidal flat area and height from hypsometric curves is presented in Grasmeijer et al. (2022) (Fig. 1.2). This

is a first step in a more detailed description of changes in intertidal flats, but the report strongly suggests that trends in the hypsometric curves, areas, and mean depths of the different depth zones should be determined on a more detailed scale for sub-sections of the basins in a structured approach.

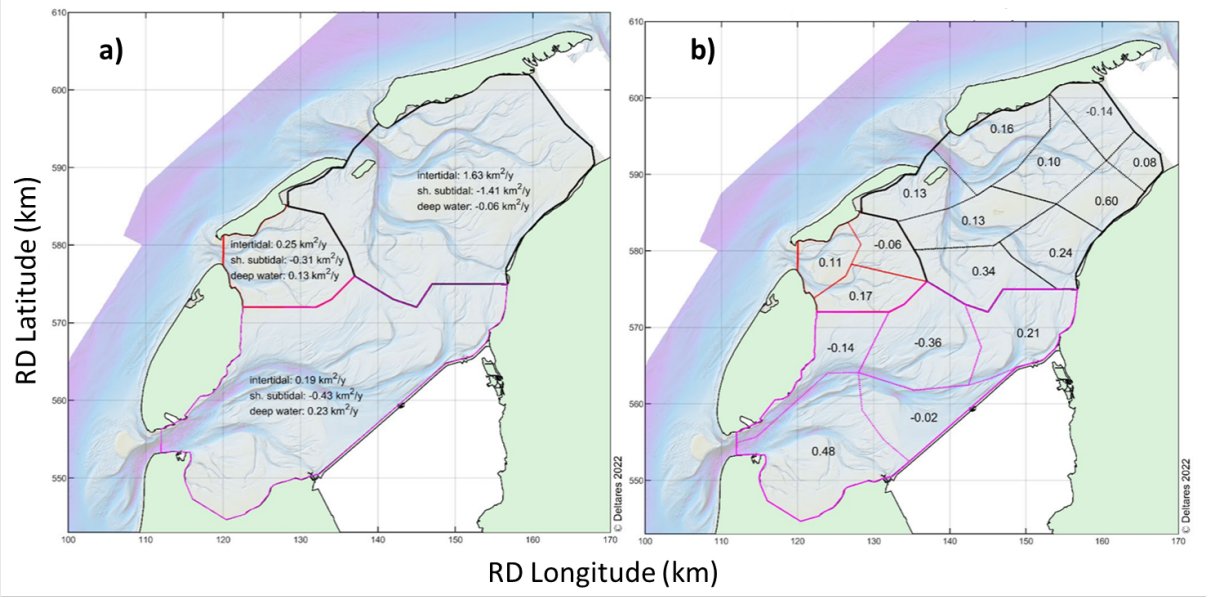

Figure 1.2: Trends (1933-2015) in area (km^2/y) per depth-zone in the western Wadden Sea for a) entire basins and b) in intertidal area for sub parts of the basins.

Source: Grasmeijer et al. (2022)

1.4. Modelling approaches in the Dutch Wadden Sea

Various modelling approaches have been developed and applied to the system to better assess the development of intertidal flats. As is often the case in modelling, the balance between computational power, complexity and comprehensibility is an ongoing struggle.

Process-based models, such as the Delft3D system (Lesser et al., 2004), can provide detailed descriptions of morphological changes based on physical processes. However, due to their high computational power requirements, these models are mostly suitable for short-term modelling. In addition, a limitation of using process-based models on longer time scales is that the behaviour of these models is complex and therefore not well understood. A problem that arises is that morphological equilibria are often not reached in long-term modelling, because there is still a knowledge gap on how to describe them physically (Wang et al., 2012). The use of process-based models therefore needs thorough validation and calibration, which requires a large amount of field data

(Elias et al., 2003).

The other main approach are behaviour-oriented models, which assume a morphological equilibrium exists and that the system will always tend to return to a state where the empirical equilibrium equations are satisfied after a perturbation. An example of such a model is the ASMITA (Aggregated Scale Morphological Interaction between Tidal inlets and the Adjacent coast) approach, which an example of reduced complexity modelling. This model, described in detail by Townend et al. (2016a, 2016b), considers morphological units and can be used to predict behaviour on large spatial scales and long time scales, which is necessary to assess developments under sea level rise. The morphological units used in the Wadden Sea model are the ebb-tidal delta, the channels, tidal flats, and salt marshes. For each unit, a state of equilibrium, volume, surface area and rates of change are described, corresponding to the absence of accommodation space (Townend et al., 2016a). Any perturbation will drive a sediment demand or supply as there will be differences in accommodation space in the prescribed units of the model (Fig. 1.3). This, in turn, will drive sediment transport and result in morphological change. Separation into units shows the aggregation in space, and since the input parameters for hydrodynamics are representative values based on long-term data, the model is also aggregated in time (Wang et al., 2018). The ASMITA model has been adapted multiple times to best fit the Wadden Sea system, and the parameters have been optimized based on various reviews and field data (Huismans et al., 2022).

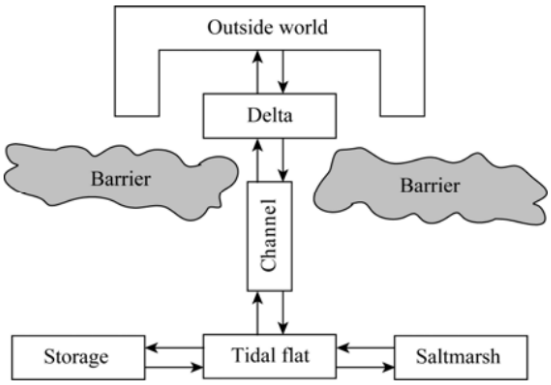

Figure 1.3: Stigmatization of an estuary or inlet into elements as used in ASMITA
Source: Townend et al. (2016a)

The ASMITA model can be applied on longer time scales due to the simplification of the system, but has a low spatial resolution, as 1D-schematisations for large parts

of the system are used (Wang et al., 2012). A 1D description of morphology is given in the form of hypsometry; the height distribution over the horizontal surface area. Hypsometric curves of tidal basins, combined with the mean low water level (MLW) and mean high water level (MHW) produce an indication of the volume, area and the height of intertidal flats that are present for each tidal basin (van Prooijen & Wang, 2013).

Changes in intertidal flat area and height from hypsometric curves produced from ASMITA modelling are predicted in Huismans et al. (2022). The described changes are based on the assumption that sediment is evenly distributed over intertidal flats and that the hypsometric curve does not change shape. With changing morphology, it is likely that the sedimentation will change across the intertidal flats and therefore the translation from volume loss to flat height and area loss is not so straightforward. In smaller basins, the tidal flats mainly show a reduction in height and in larger basins a reduction in area (Huismans et al., 2022). Furthermore, the hypsometric curves are only available for entire tidal basins, and the Pinkegat and Zoutkamperlaag basins are combined into one hypsometric curve. Therefore, only the spatial variation between entire tidal basins can be observed. Within the current ASMITA model for the Wadden Sea as used by Huismans et al. (2022), no differentiation can be made within individual basins.

The low resolution of hypsometric curves causes intertidal flats to be poorly represented in the predictions (Wang et al., 2012). It would be beneficial to incorporate a higher spatial resolution of hypsometric curves as input to the ASMITA model and to be able to predict local changes from the modelling results. For example, the schematisation morphological units in the ASMITA model can be done with a higher resolution in units. To incorporate this, empirical morphological equilibrium relations to describe smaller units are necessary (Huismans et al., 2022).

An attempt of finding such a morphological equilibrium is done by using Horton's hierarchical and fractal analysis of channel circumference (Cleveringa & Oost, 1999) to approach the channel-geometry of tidal basins in the Wadden Sea. This reveals that the basins have similar branching patterns, that also show similarity to modelled short tidal basins (Marciano et al., 2005). This fractal approach suggests that a certain level of self-organization leads to comparable channel-system geometries. If the found

channel-geometry can be considered as an equilibrium morphology, this could improve behaviour-oriented modelling of tidal systems (Cleveringa & Oost, 1999). Channel systems with a tidal prism than $55 * 10^6 m^3$ are found to deviate, which makes this not applicable on a smaller scale within the basins.

For a more detailed interpretation of the results produced by the ASMITA model on the development of the bathymetry of the Wadden Sea, beneficial to assess which variables determine the shape of hypsometric curves in tidal basins. Further analysis of the shape of hypsometric curves could also shed more light on the heterogeneity of dynamics and distribution of intertidal habitats within individual tidal basins in the Wadden Sea and between the eastern and western parts of the system.

1.5. The concept of hypsometry

The hypsometric curve summarizes the height (or volume) distribution in a (drainage) basin or morphological unit. In tidal basins, the shape of the hypsometric curve is strongly influenced by the ratio of channels and tidal flats.

The shape of hypsometric curves has been linked to various processes and influences. From Dieckmann et al. (1987); Kirby (1992); Wells and Park (1992); Yu et al. (2012) the following relations have been defined:

- Convex hypsometric curves are linked to smaller basin areas with large tidal ranges, long-term accretion trends, low wave energy, and relatively small channel area within tidal basins. Friedrichs and Aubrey (1996) shows that embayed shorelines can also decrease concavity in hypsometric curves.
- Concave-up hypsometric curves have been associated with larger basin areas, smaller tidal ranges, long-term erosional trends, high wave energy, and large relative channel area within tidal basins.

To define the shape of the hypsometric curve, theoretical definitions are often fitted to the data to summarize the shape into comparable parameters. For spatial and temporal comparison of areas, hypsometric curves are normalized ranging between 0 and 1 on both the x and y axes to which theoretical curves can be fitted. When comparing hypsometry through time of a certain unit, it is important to use the same area for the curve for each time step.

The hypsometric curve is generally normalized through calculation of the hypso-

metric integral for each point through the following equations:

$$y = \left[\frac{h - Hmin}{Hmax - Hmin} \right] \tag{1.1}$$

And

$$x = \left(\frac{a}{A} \right) \tag{1.2}$$

The original parametric definition by Strahler (1952) is defined as follows:

$$y = \left(\frac{d-x}{x} \frac{a}{d-a} \right)^z \tag{1.3}$$

in which a and d are constants and z is an exponent either positive or negative. Both axes of the hypsometric curve are defined as dimensionless parameters, which makes curve comparison possible. The y-axis is defined as the proportion of total basin height and the x-axis is defined as the proportion of total basin area ($y = h/H$ and $x = a/A$), so values x-axis represent normalized area above a certain normalized elevation (y). The curve always has an x-intercept of 0 ($x = 0, y = 1$) and a y-intercept of 1 ($x = 1, y = 0$). A model hypsometric function is shown in the figure 1.4a).

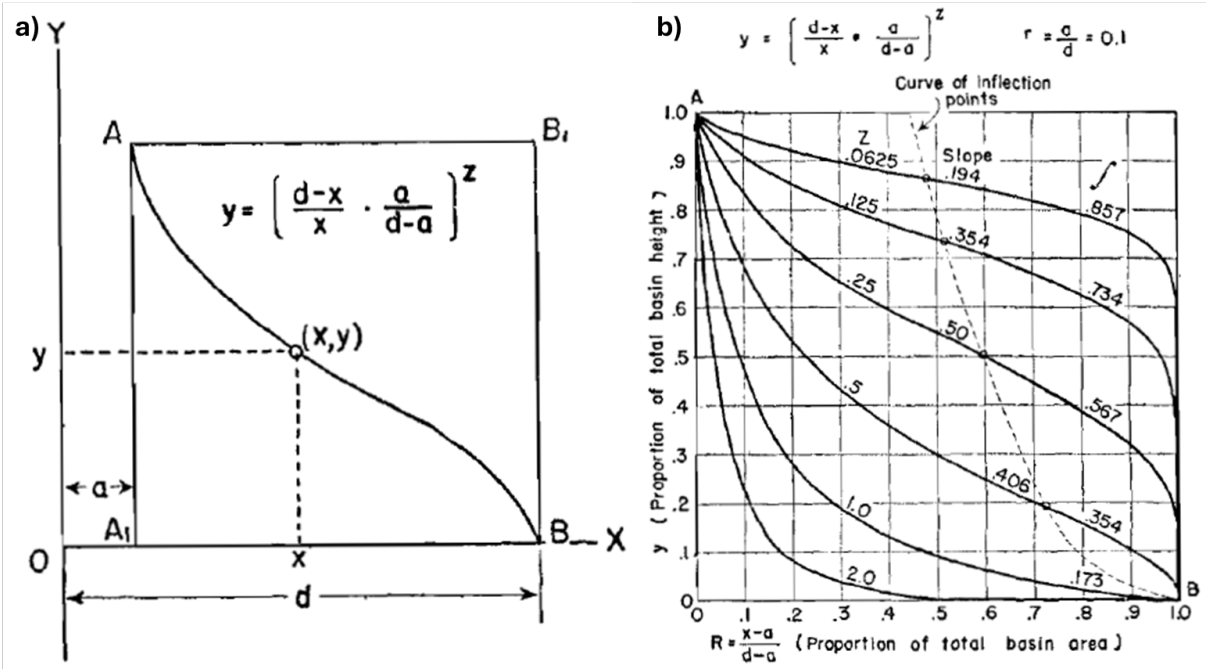

Figure 1.4: Model hypsometric function (a) and a family of curves for the value $r = \frac{a}{d} = 0.1$ (b)
Source: Strahler (1952)

The inflection point of the curve can be determined from the ratio $r = \frac{a}{d}$. Lower values for r increase the sinuosity of the curve. The exponent z determines the location of the curve (Strahler, 1952). Figure 1.4b) shows examples of the Strahler hypsometric curve and the influence of different values for the exponent z.

The hypsometric shape of an area strongly depends on channel networks and catchment (or basin) geometry (Willgoose & Hancock, 1998). It is concluded that the Strahler definition of the hypsometric curve does not account for the shape of the catchment and the scale effects that come into play when comparing different basins. Through time, multiple definitions have been found. The various approaches to defining hypsometric curves indicate that for different locations and morphological units, different theoretical hypsometric curves might best describe the volume distribution. This is predominantly the effect of varying scales and different forming processes in the units. Any function or shape of hypsometric curve can be fitted to a dataset, in order to find out which definition of the curve fits best. To find the best-fitting curve, it is suggested to fit a range of hypsometry types to the data set (Leuven et al., 2018).

For tidal basins, the number of studies that use hypsometric characterization through parameterization is scarce. An attempt was made to use a theoretical approach to area hypsometry for the tidal basins of the German Wadden Sea by Renger and Partenscky (1974). The logarithmic function found describes the relationship between the volume of water below a given height and the associated bathymetry. However, this function contains an empirical coefficient that is specific to each individual tidal basin, and the research by Yu et al. (2012) shows that hypsometry is also scale dependent. A relationship between tidal flat hypsometric concavity and tidal range is presented and it is concluded that the shape of area hypsometric curves is dependent on both basin scale and tidal range. The relationship found only focuses on the hypsometry of the area above the MLW and is not used to find descriptive parameters for the entire hypsometric curve, therefore this approach is not used in the analysis in this research.

A range of theoretical definitions of hypsometry are compared in a review by Bajracharya and Jain (2021). This shows that in most quantitative approaches to hypsometric analysis, deviations in theoretical hypsometric curves from empirically determined hypsometric curves are most pronounced in the head and toe of the defined functions. A new formulation for the estimation of hypsometric curves is proposed that includes an

additional parameter, which allows for more variation in the shape of the hypsometric curves. The newly proposed *Generalized Hypsometric Function* allows for more diverse hypsometries than the Strahler definition, but still accommodates the boundary conditions of the y-intercept at $x = 0$, $y = 1$ and the x-intercept of the curve in $x = 1$, $y = 0$ (Bajracharya & Jain, 2021). The use of hypsometric curves and linking fitting parameters to diverse shapes and physical processes is still limited, as well as efforts to test hypsometric functions in different morphological units or (drainage) basins.

The selection of hypsometric functions considered in this research is based on the review by Bajracharya and Jain (2021), Leuven et al. (2018), and Boon III and Byrne (1981) and consists of the following theoretical definitions.

- The original Strahler curve (Strahler, 1952)

$$h/H = [\frac{r}{1-r}]^z [\frac{1}{(1-r)x + r}]^z \tag{1.4}$$

  - Boundary conditions: $r \in (0, 1], z > 0$

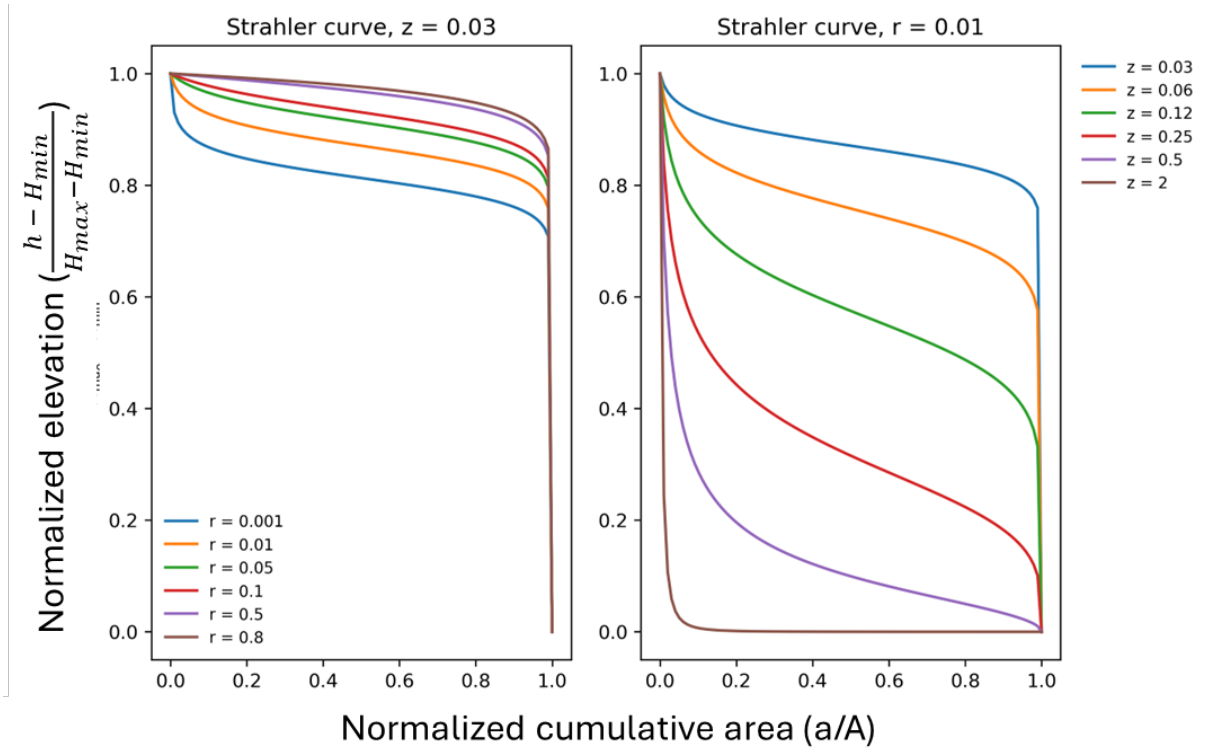

Figure 1.5: Influence of r and z parameter on the shape of the Strahler curve.

- The inverse Strahler curve (Leuven et al., 2018)

$$h/H = \frac{[\frac{[x^{\frac{1}{z}}(1-r)]}{r} + 1]^{-1} - r}{1 - r} \tag{1.5}$$

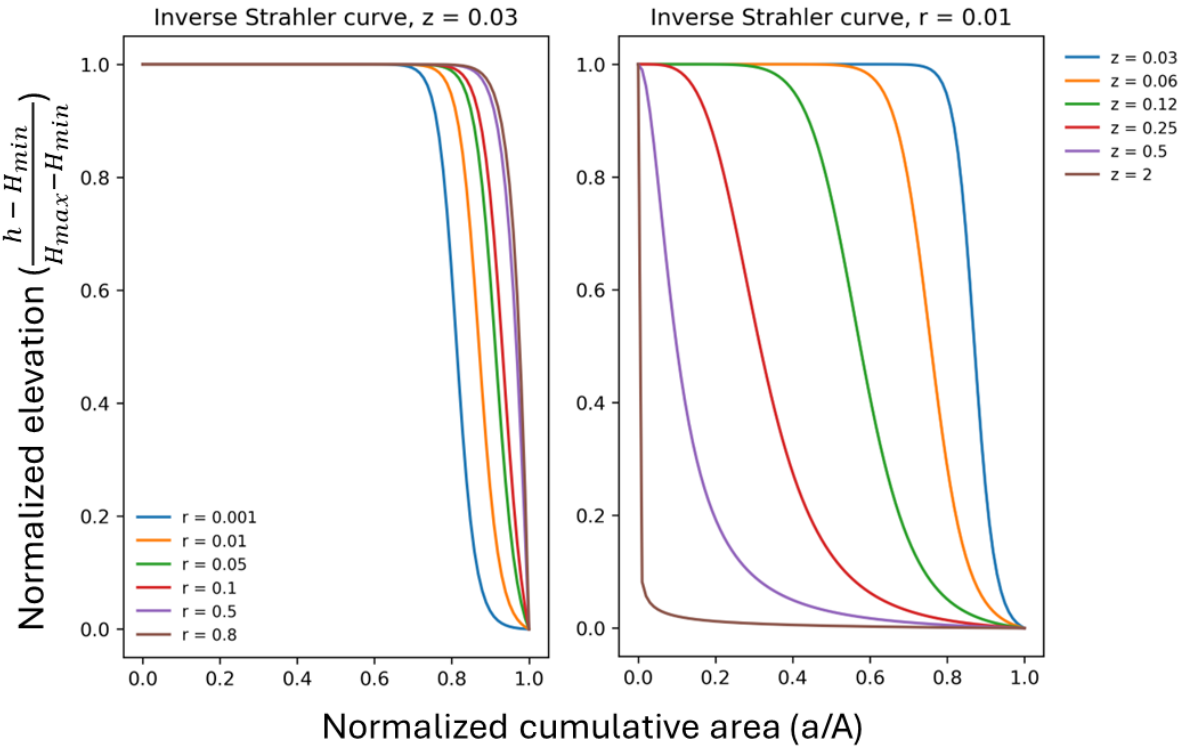

Figure 1.6: Influence of r and z parameter on the shape of the Inverse Strahler curve.

- The Sigmoidal curve (Sarkar & Patel, 2011)

$$h/H = \frac{ab + cx^d}{b + x^d} \tag{1.6}$$

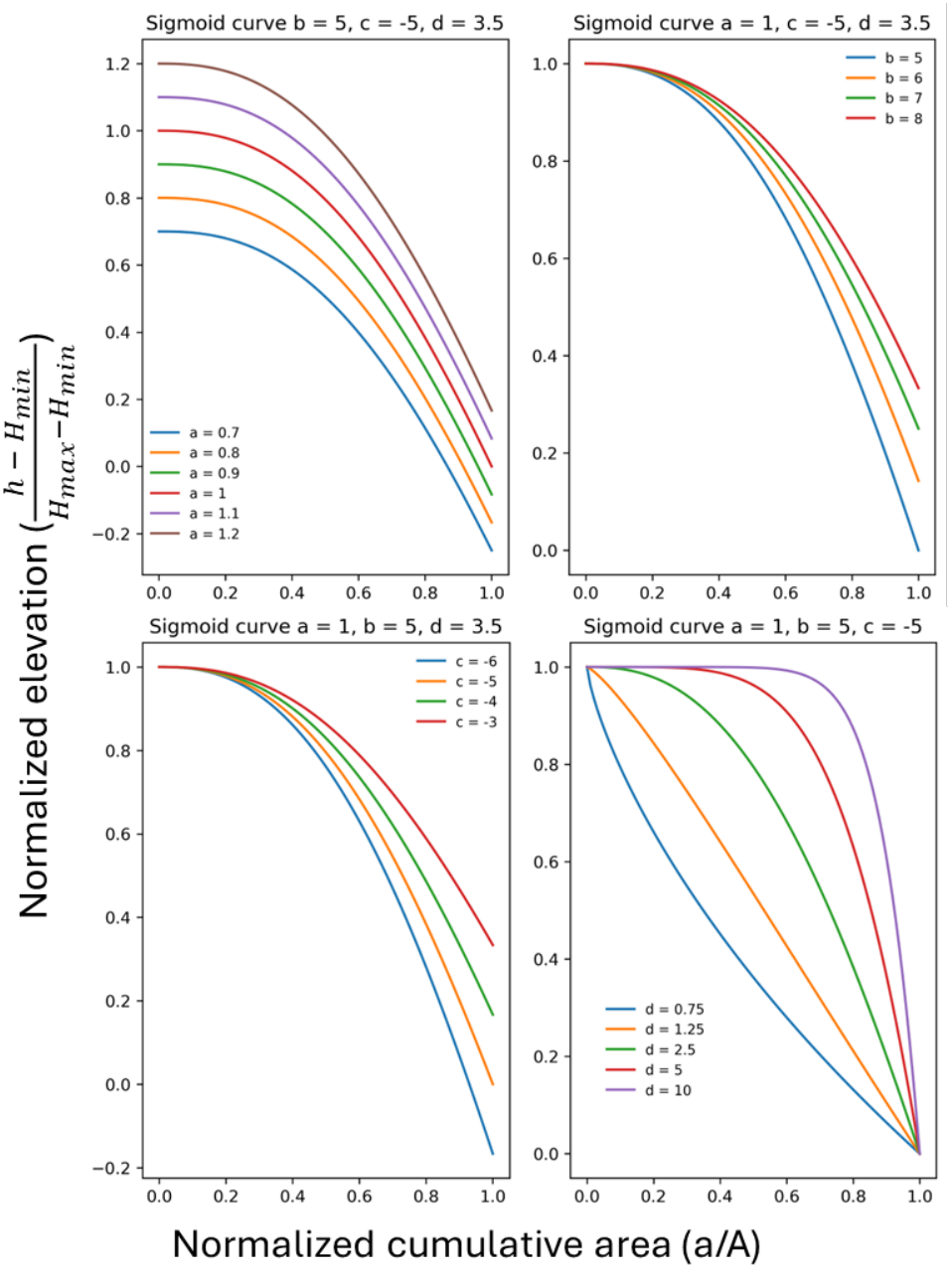

Figure 1.7: Influence of a, b, c and d parameter on the shape of the Sigmoid curve.

- Yield curve (Sarkar & Patel, 2011)

$$h/H = \frac{1}{a + b^x} \tag{1.7}$$

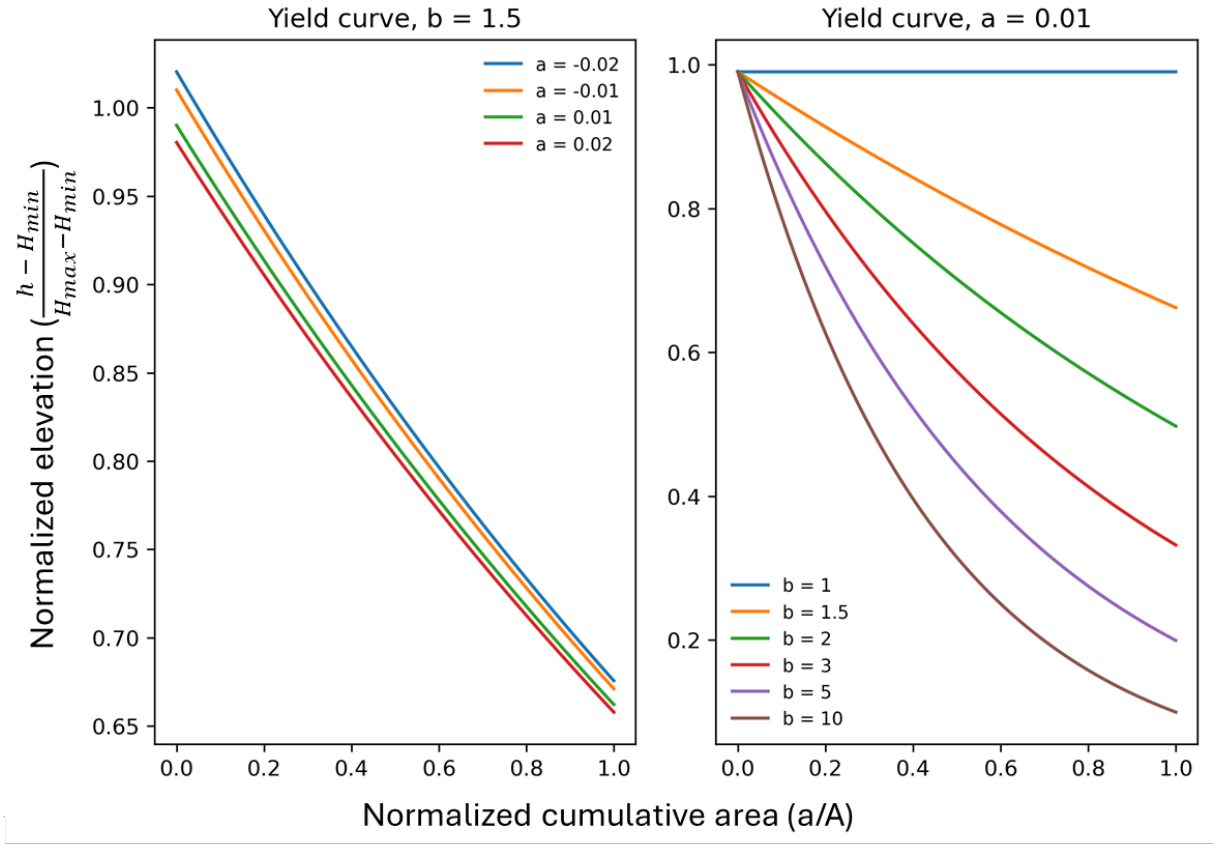

Figure 1.8: Influence of a and b parameter on the shape of the Yield curve.

- Logistic curve (Sarkar & Patel, 2011)

$$h/H = \frac{a}{1 + be^{-cx}} \tag{1.8}$$

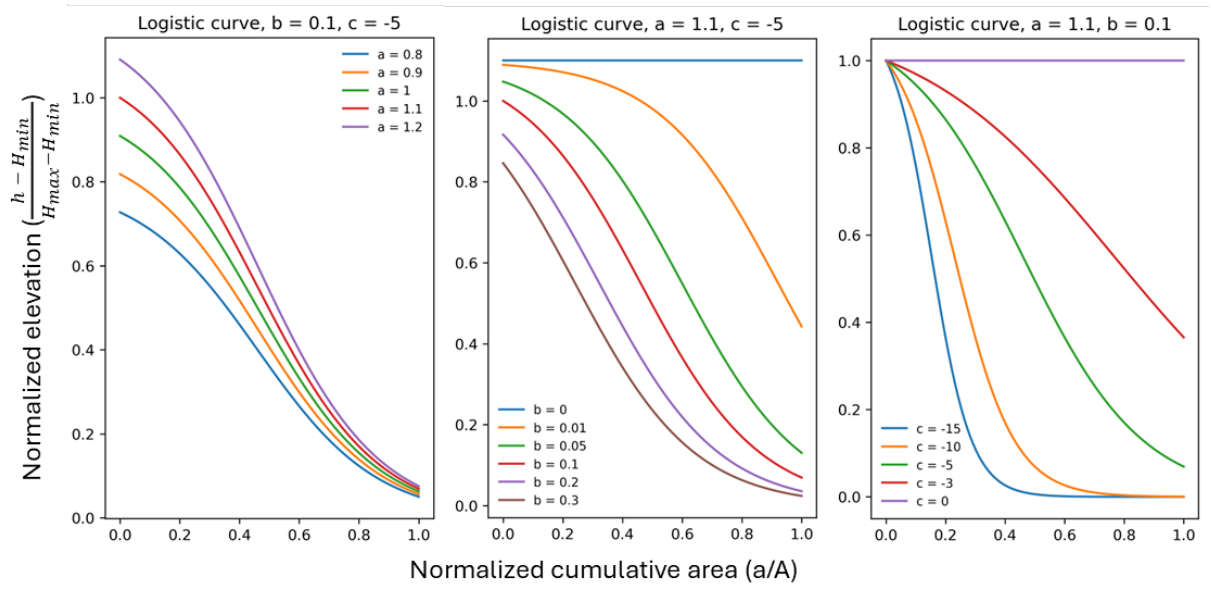

Figure 1.9: Influence of a, b and c parameter on the shape of the Logistic curve.

- The Boons curve (Boon III & Byrne, 1981)

$$\frac{a}{A} = \frac{G}{r + G * (1 - r)} \tag{1.9}$$

$$G = (1 - h/H)^{\gamma} \tag{1.10}$$

$$\gamma = 1/z \tag{1.11}$$

$$h/H = 1 - (xr^z - (x^2 * r * (1 - r))^z) \tag{1.12}$$

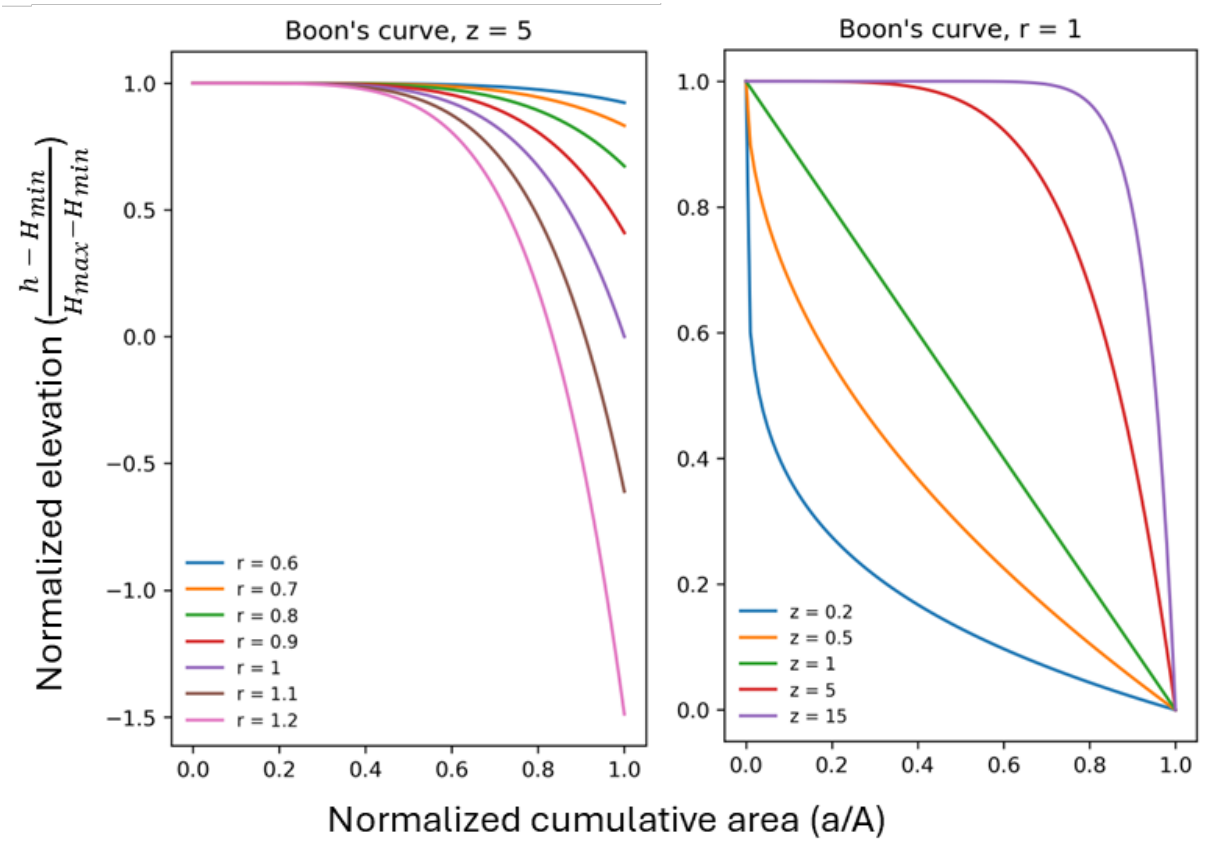

Figure 1.10: Influence of r and z parameter on curve shape for the Boon's curve (Boon III & Byrne, 1981).

- Generalized hypsometric curve (Bajracharya & Jain, 2021)

$$y = \left[\frac{r(1 - x^m)}{(1 - r)x^m + r}\right]^z \tag{1.13}$$

  - Boundary conditions: $r \in (0, 1], \quad z > 0, \quad m > 0$

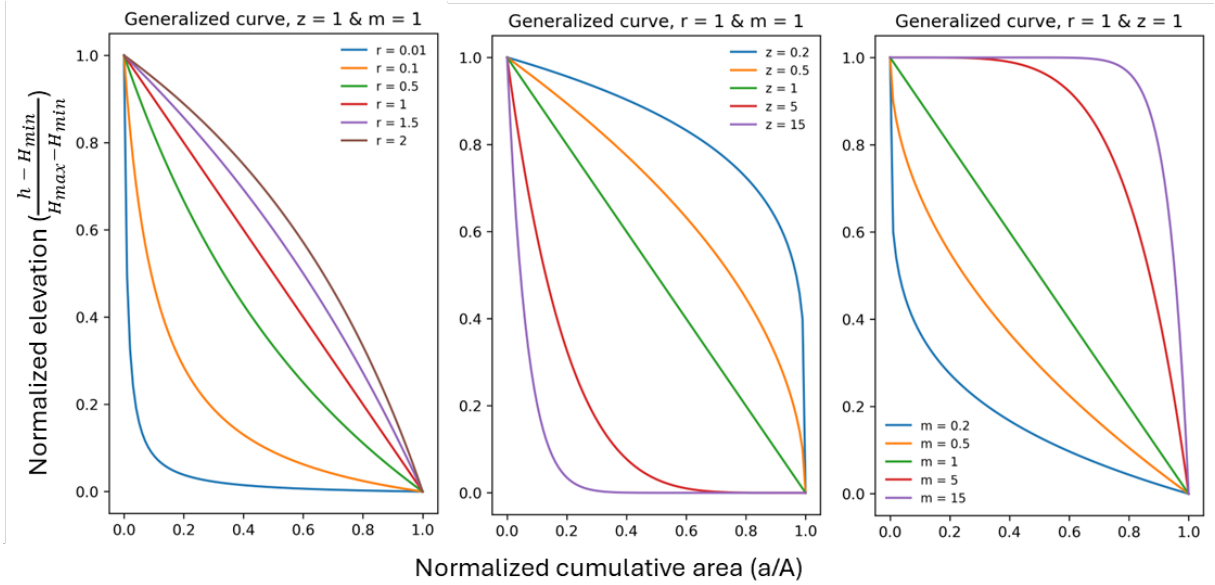

Figure 1.11: Influence of *r*, *z*, and *m* parameters on curve shape for the Generalized curve (Bajracharya & Jain, 2021).

- Rational curve (Sarkar & Patel, 2011)

$$h/H = \frac{a + bx}{1 + cx + dx^2} \tag{1.14}$$

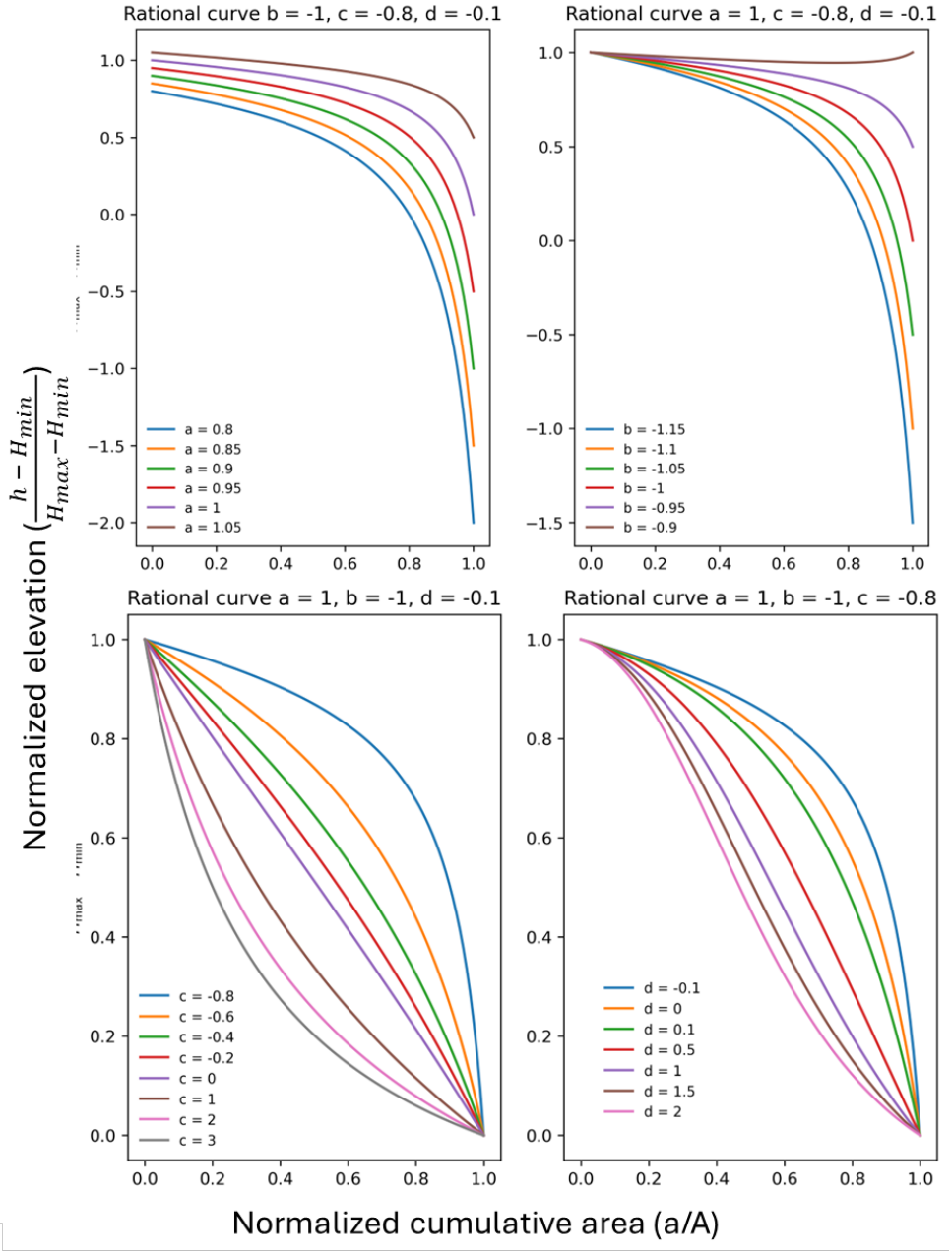

Figure 1.12: Influence of *a, b, c* & *d* parameters on curve shape for the Rational curve (Sarkar & Patel, 2011).

Concavity-convexity throughout this research is used as in Leuven et al. (2018), following the example in figure 1.13.

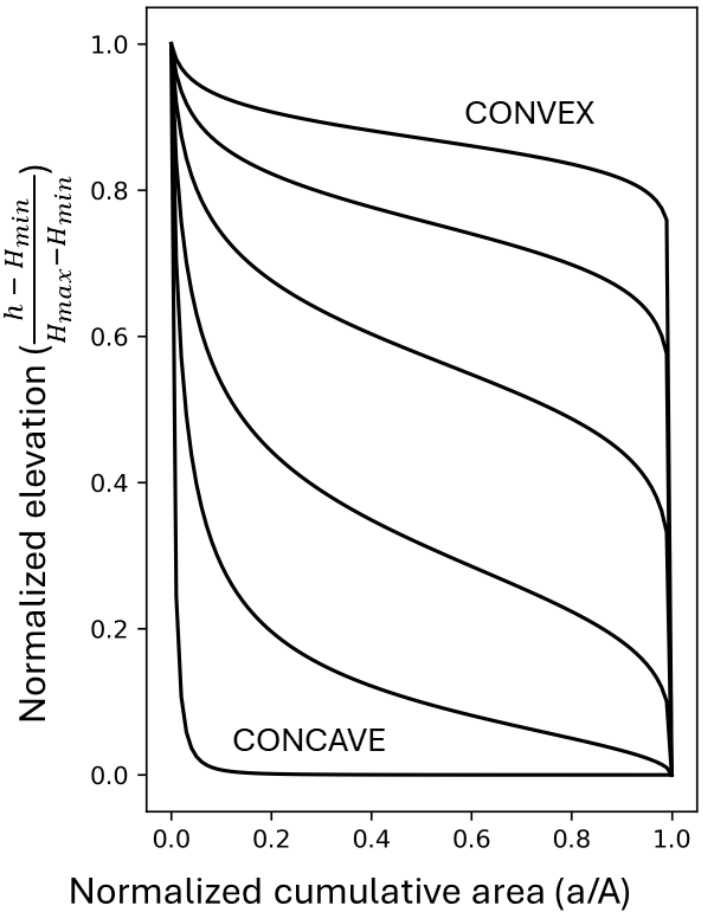

Figure 1.13: Definition of concavity-convexity in hypsometric curve shape. Example curves produced with Strahler curve as in Figure 1.5.

1.6. Aim and research questions

The aim of this research is to create a detailed hypsometric characterization of the tidal basins of the Dutch Wadden Sea. To assess spatiotemporal changes in hypsometric curve shape and intertidal area and volume within the tidal basins, I design a method of systematically dividing the full grids into sub-sections. Evaluation and comparison of the hypsometric curves provides insight on the heterogeneity morphological patterns and spatiotemporal evolution within the tidal basins of the Dutch Wadden Sea. As hypsometric curve shape has been related to various physical parameters, this analysis aims to create a better understanding of how these parameters influence the morphology within tidal basins on a more detailed scale.

The main questions of this research are:

- How can parameterization of hypsometry be applied in the Dutch Wadden Sea?

  - Which theoretical definition of hypsometry best represents the intertidal flats?
  - What is the influence of resolution differences of the grid data on hypsometry?

- What is the spatiotemporal variation in parameterized hypsometry and intertidal flats in the Dutch Wadden Sea tidal basins and how does this relate to the physical processes at play?
  - How do these variables change between the tidal basins?
  - What is the variation within a tidal basin?
    * What are the differences between western and eastern basin halves?
    * What trends are present with distance from the inlet?
- Are spatial patterns in hypsometry and intertidal flat morphology scale-dependent?
  - Do small tidal basins show comparable morphology to the landward part of large basins?

1.7. Hypothesis

Hypsometric characterization by Leuven et al. (2018) shows how the (inverse) Strahler function can be used to give a general prediction on hypsometry for different cross-sections in the Ems-Dollard estuary, so I expect it to work for annular sub-sections of the estuary as well. As the Ems-Dollard estuary is the result of different forming processes and has a distinctly different geometry from the tidal basins, I expect that it will be most suitable to use a different theoretical curve for the tidal basins.

The larger grid cells for the historic grids have a smoothing effect that will affect the shallowest and deepest parts the most, therefore I expect the effect of resolution to be most pronounced at the top and bottom of the curve. Furthermore, I expect the influence to be strongest for the smallest basins, as these have a higher heterogeneity and steep transitions between channels and flats, so the smoothing effect will be strongest.

The concavity-convexity of the hypsometric curve has been correlated with various physical parameters, so I expect that the curve shapes between and within the tidal basins in the Dutch Wadden Sea can also be related to these parameters.

From west to east, the tidal basins become smaller, wave activity becomes lower, and the relative channel area decreases. This leads to the hypothesis that convexity increases eastward. In respect to their geological history a clear difference between the western and eastern basins is expected. However, convexity/concavity is also influenced by accretional or erosional trends, geological history and human interferences, so this contrast might not be straightforward.

With distance from the inlet, I expect that a trend of increasing convexity in the hypsometric curves exists based on the earlier research by Deltares and the theories based on system knowledge. With distance from the inlet, the embayed shoreline of the mainland is closer and thus higher convexity can be expected. Additionally, with distance from the inlet, the channels become smaller, and the wave activity decreases.

Between the halves of the basin, I expect to see the result of wind-driven sediment transport within the tidal basins. The prevailing southwesterly winds in combination with the increasing eastward tidal range could lead to higher sediment availability in the (north)eastern halves of the basins and thus to more convex hypsometries. According to Wang et al. (2020) however, the flats in the eastern half would be lower and maybe less convex hypsometries exist. Overall, differences are expected between the basin halves and it is also expected that on a larger scale the western and eastern Wadden Sea show contrast in this due to their underlying history.

with respect to temporal trends in the development of the intertidal area within the tidal basins, various theories exist. Huismans et al. (2022) describe how drowning will be stronger further landward in the tidal basin, whereas in Hofstede (2015) it is argued that the comparison with Holocene transgressions is not applicable and it can be expected that the intertidal area on the seaward side of the basins will drown first. From the preliminary analysis within the tidal basins by Grasmeijer et al. (2022) it is visible that the flat area and height increase primarily on the landward side, which could point to a pattern similar to that described in Hofstede (2015).

Hypsometry in the tidal basins is predominantly dependent on scale, tidal range, and basin geometry (Yu et al., 2012; Eysink, 1993). Therefore, I expect to find this scale-dependency in the morphology of the tidal basins in the Dutch Wadden Sea. Specifically, if the forming factors in the morphology of the tidal basin lead to scale-dependent patterns, small tidal basins would be comparable to the outer part (close to

the landward boundary) of the larger basins when this part is considered as a collection of small tidal basins in itself.

2. Method

In this research hypsometric curves are created from the bathymetric data of Rijkswaterstaat, collected in the Vaklodingen program. The basin areas are based on the collection areas of the Vaklodingen program and are used to create hypsometric curves, which are normalized. The normalized curves are then summarised in comparable parameters by fitting theoretical definitions of hypsometry.

Firstly, full basin grids bounded by tidal divides are used to find the best fitting parameterization and for initial data exploration. In addition, spatiotemporal trends in the hypsometry of the entire basin and the intertidal flats are analysed.

Secondly, the newer grids are divided into smaller subsections, following the structure of analysis in Figure 2.1. To assess the differences between the basin halves, recent grids are cut in half. Annular sub-sections are created with distance from the inlet, based on the hypothesis that a trend in morphology exists with distance from the inlet. The annular decreasing basin size is designed with the aim of comparing the distribution of intertidal flats and hypsometry between the landward part of large basins and the small tidal basins. In the resulting plots, the distance from the landward boundary is therefore a proxy for increasing the basin size. This is based on the hypothesis that the outer part (close to the landward boundary) of large basins can be considered as a collection of small basins in itself.

Only the grids from 1985 onwards are included for characterisation of patterns within the tidal basins, as these grids have a higher resolution and better coverage of the basins, without losing area at the edges of the basins. This results in a more complete analysis. In addition, this choice ensures that all data have the same resolution and roughly the same time span is present for all tidal basins as the older grids do not exist for the basins to the east.

For each approach, the parameters of the best-fitting curve, the absolute and relative area (Af/Ab), the absolute and relative volume (Vf/Vb), and the mean height (Hf) of the intertidal flats are determined. Furthermore, the (inverse) Strahler curve is fitted to the annular sub-sections of the Ems-Dollard estuary for comparison with Leuven et al. (2018).

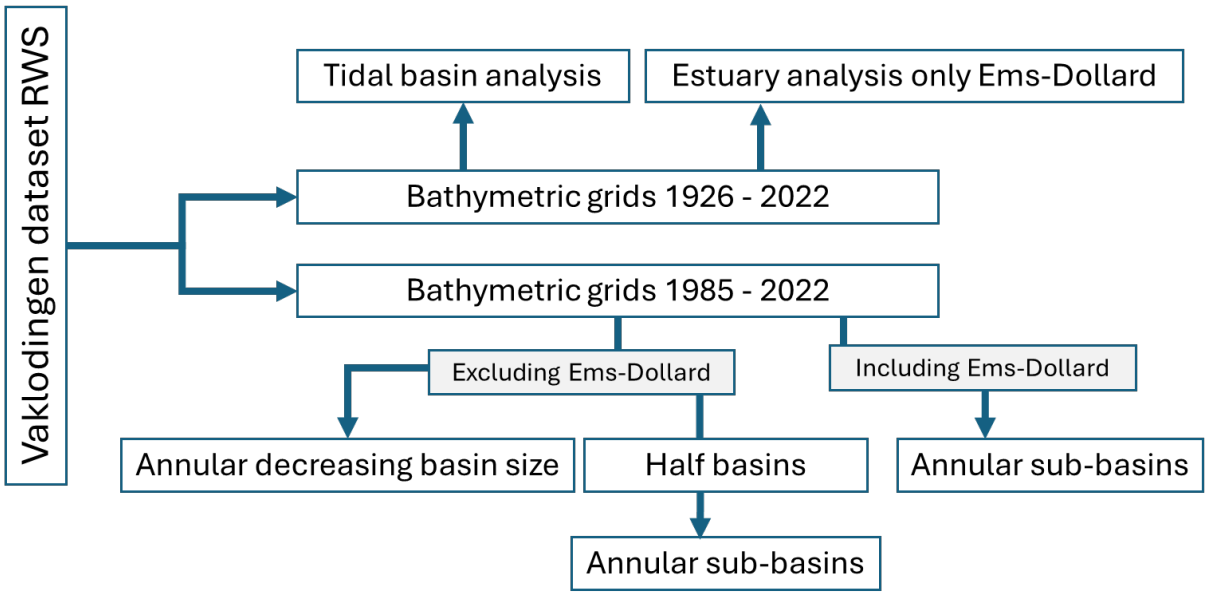

Figure 2.1: Diagram showing the structure of data analysis.

2.1. Data description and preparation

The bathymetric data used for this research are collected through the *vaklodingen* program of Rijkswaterstaat (Fig. 2.2). Data from before 1985 have been digitized with a resolution of 250x250m. For the Frisian Inlet, the historic grids before 1985 are stored with a resolution of 87.5mx87.5m. Some of these lower-resolution grids still contain spatial data gaps that must be considered when using them in analysis. Since 1985, bathymetric data have been collected in the Dutch Wadden Sea area, divided into six predefined storage basins, each of which is surveyed once every six years. Therefore, data from the different compartments were not obtained in the same years. The data is collected using sonar soundings from an single-beam echo sounder, carried by a research vessel. The research vessel sails along parallel lines (in Dutch called 'raaien') at 200m intervals. From 2003, laser altimetry was used for intertidal areas. The bathymetry and laser altimetry are spatially interpolated to cover up remaining holes in the data and combined into a grid with a resolution of 20x20 metres by Rijkswaterstaat, with an accuracy between 0.11 and 0.40m (Wiegman et al., 2005; Perluka et al., 2006). An overview of the bathymetric data that has been used within this research is given in table 2.1.

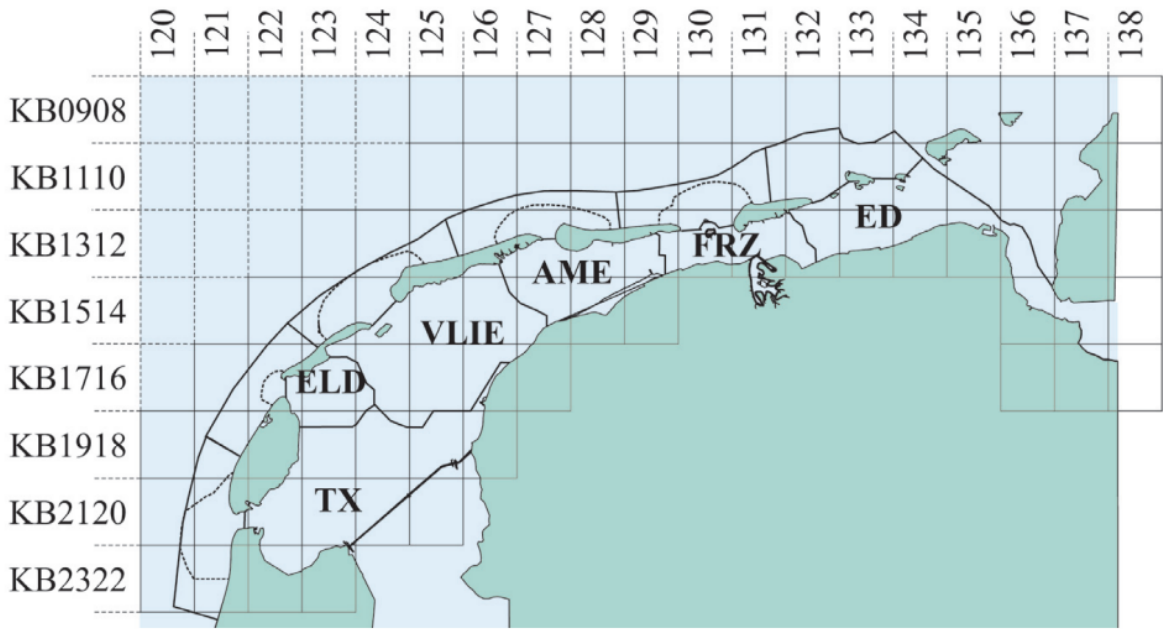

Figure 2.2: Vaklodingen blocks in the Wadden Sea. Ebb-tidal deltas are outlined by the dashed lines. The solid lines indicate the polygons used in Elias et al. (2012).

Source: Elias et al. (2012)

Table 2.1: Bathymetric data used in this research - Rijkswaterstaat. Light blue indicates low resolution data, dark blue 20mx20m resolution data.

Marsdiep	Eierlandse Gat	Vlie Inlet	Ameland Inlet	Pinkegat/ Zoutkamperlaag	Eijlanderbalg/ Lauwers/ Schild/ Sparregat	Ems-Dollard
1926 (20m)	1926 (20m)	1926 (20m)	1926 (250m)	1926 (20m)		
1933 (250m)	1933 (250m)	1933 (250m)	1927 (20m)			
1951 (250m)	1949 (250m)	1951 (250m)	1950 (250m)			
1965 (250m)	1962 (250m)	1965 (250m)	1967 (250m)	1970 (250m)		
1972 (250m)	1971 (250m)	1972 (250m)	1973 (250m)	1975 (250m)		
1977 (250m)	1976 (250m)	1977 (250m)	1978 (250m)	1979 (250m)		
1982 (250m)	1982 (250m)	1982 (250m)	1984 (250m)	1982 (250m)		
1985 (20m)	1987 (20m)	1988 (20m)	1989 (20m)	1987 (20m)	1989 (20m)	1985 (20m)
1991 (20m)	1993 (20m)	1992 (20m)	1993 (20m)	1994 (20m)	1994 (20m)	1990 (20m)
1997 (20m)	1999 (20m)	1998 (20m)	1999 (20m)	2000 (20m)	2000 (20m)	1997 (20m)
2003 (20m)	2003 (20m)	2004 (20m)	2005 (20m)	2006 (20m)	2007 (20m)	2002 (20m)
2009 (20m)	2011 (20m)	2010 (20m)	2011 (20m)	2012 (20m)	2013 (20m)	2008 (20m)
2015 (20m)	2017 (20m)	2016 (20m)	2017 (20m)		2019 (20m)	2014 (20m)
2021 (20m)		2022 (20m)				2020 (20m)

2.1.1. Interpolation to account for spatial gaps in the data

The Rijkswaterstaat dataset contains measuring inconsistencies and gaps that need to be addressed before any analysis can be done. The bathymetric grids have been used in many different reports, but most mention only a short summary of how gaps were dealt with, and no complete interpolated data set is easily accessible. Here, data preparation and interpolation for this research are described.

Firstly, the .asc files were visualized in ArcGIS (Esri, 2023) and exported for each

tidal basin, for each available year in .TIFF format, with the value 10.000 for the grid cells without data. The combination grids are cut into individual basins using the most recent separate tidal basin available as .asc file in the Rijkswaterstaat dataset. For the Huibert-Lauwers basins the grids are divided into four separate areas; the Eijlanderbalg, Lauwers, Schild, and Sparregat. The Frisian Inlet basin is divided into the Pinkegat and the Zoutkamperlaag.

Further data-analysis was done by programming in Python (Van Rossum & Drake, 2009). All grid files were imported in the Spyder console (Raybaut, 2009) using the rioxarray package. The cells with 10.000 were set to "nan". Some specific calculations were necessary as there were some differences in measuring between the grids:

- The grids that were part of the Combination grid 1 (C1) were multiplied with -1;
- For the Vlie Inlet the 2022 grid was multiplied by 100 to match the unit (cm) of the other grids;
- For the Pinkegat and Zoutkamperlaag, specific corrections were necessary;
  - The C1 grid was not multiplied by -1, but instead filtered below 20m;
  - The 1970, 1975, 1979 and 1982 grids (*Conlod* files) were multiplied by 10 to match the unit (cm) of the other grids;
- The 1994 grids for the Eijlanderbalg, Lauwers and Schild and Sparregat were filtered for values larger than -200m as these values were assumed to be incorrect.

After these corrections the low resolution grids are interpolated onto the coordinates of the higher resolution grids using dask.array and concurrent futures (see Appendix B.1) to reduce memory usage. The grids are then ordered in time and a set of three interpolation steps is performed. For this research, correction of spatial gaps in the grids is based on time interpolation. Spatial interpolation in a morphologically heterogeneous unit such as a tidal basin will result in losses of small features such as channels.

- A linear interpolation through time with the directly adjacent (t-1 and t+1) grids is carried out;
- A second linear interpolation through time with grids from t-2 and t+2 is carried out;

- Lastly the remaining holes after the first two interpolations (which are only a few cells) are directly taken from the previous and next grid in time respectively.

After these interpolations, the grids are masked to only store overlapping areas, as it is important to always compare the same area through time when using hypsometry (see 1). These georeferenced DataArrays are then saved to .TIFF files for further calculation. An example of Interpolation of a grid is shown in Figure 2.3. This is the grid with the largest holes in the whole dataset; for the rest of the grids the holes are less extreme. For each basin, the most recent interpolated grid can be found in Appendix A.1. These grids (of the most recent years) show the area that is used for each year in the hypsometric curves. For the long term analysis, the interpolation and masking is done using all grids, and for the short-term both interpolation and masking is done using only the recent grids.

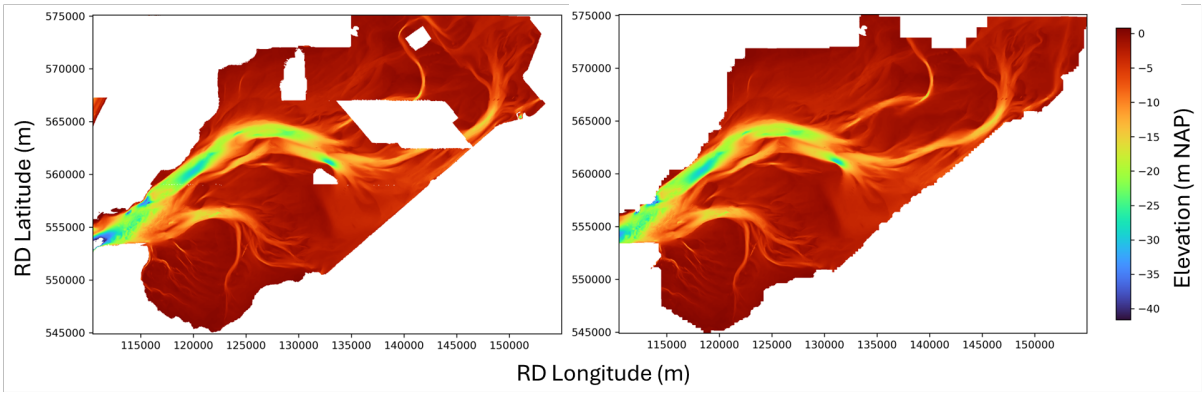

Figure 2.3: Example of a raw (a) and an interpolated grid (b). (Marsdiep, 1985)
Source: Bathymetric data Rijkswaterstaat

Scripts:

- *Interpolating_arrays_and_saving_tiffs.py*
- *Interpolating_arrays_and_saving_tiffs_short_term.py*
- *Function_nodata_tiffs.py*
- *Functions_correct_grids.py*
- *Function_upscale_lowres.py*
- *Function_interp_time.py*
- *Function_masking_arrays.py*

2.1.2. Assessment of influence of resolution

To assess the influence of resolution, the most recent high resolution (20m) grids are down scaled to resolutions of 40m (twice as low), 87.5m (matching the older grids for the Pinkegat and Zoutkamperlaag), 125m and 250m (matching all other older grids) using the rioxarray and rasterio packages (Gillies, 2019; GitHub, 2024). From these down scaled grids, hypsometric curves are created and normalized. The error in intertidal flat area is calculated and the normalized curves are visually compared. During down scaling, some area on the edges of the grids is lost, which magnifies changes in curve shapes.

Scripts:

- *Resolution_influence_basins.py*
- *Function_create_hypsometry_diffresolutions.py*

2.2. Creation of sub-sections

For the creation of the sub-sections, function are created that cut the full grids of each basin into smaller grids and save these. For each basin, the following variables are defined:

- The inlet; based on where the centre of the inlet was visually most prevalent over time
- a second point; between the inlet and this point a line is created which is used to cut the grid in halves. These lines are defined such that for basins where there is a clear split in the channels after the inlet each half contains one of them and their subsequent bifurcations. For the basins in which no clear bifurcation takes place after the inlet, this line is divined based on the temporally prevailing orientation of the main channel. In the Zoutkamperlaag and Lauwers basins, the channel exhibits a strong eastward bend. Consequently, dividing these basins into halves may be a bit more arbitrary.
- a radius; for each basin, 10 circles are cut with the inlet in the center. This gives annular dividing lines with increasing distance from the inlet, which is used for the annular sub-sections as well as for the annular decreasing basin size. In the code, 11 circles are drawn through the grid and by manually minimizing amount

of cells in the 11th circle, the radius has been maximised for the ten annular sub-sections. This means that for each grid a few grid cells are lost at the outer edges, but by maximizing the radius manually this never exceeds a loss of more than 9 cells in width (180m).

Figure 2.4 shows an example how this is done for the Marsdiep, Appendix A.1 contains maps of sub-section creation for each basin.

One script divides the grids into basin-halves based on the inlet and the second point, another creates annular sub-sections, and one script combines these approaches. The annular decreasing sub-sections are created by cutting of the smallest circle consecutively. The sub-sections are then again saved as GeoTIFFS, while keeping their original coordinate references.

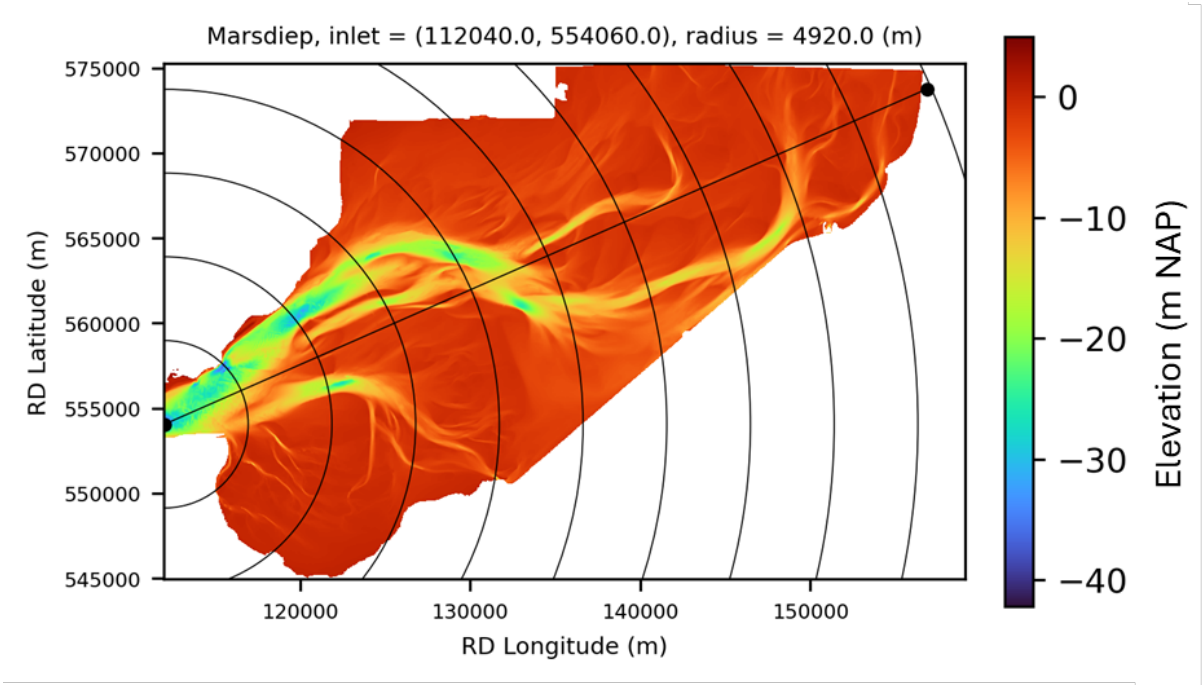

Figure 2.4: Example of how sub-sections are defined. (Marsdiep, 2021)

Scripts:

- *Creating_subbasins_half.py*
- *Creating_subbasins_annular.py*
- *Creating_subbasins_annular_halves.py*
- *Creating_subbasins_annular_decreasing_frominlet.py*

2.3. Creation of hypsometric curves

First, the hypsometric curves are created from the saved GeofTIFF files. Histograms are calculated from which the cumulative hypsometric curve is created by multiplying the count for 500 bins of height values with the resolution of the data. Creating a histogram first reduces calculation time and results in smoother curves by binning the elevation values. The counts of the histogram multiplied by the cell size then give the area of each elevation bin. Area hypsometric curves are saved to .csv files for further calculation.

Scripts:

- *Saving_hypsometry_csv_shortlong_term_full&sub.py*
- *Function_create_hypsometry.py*

2.3.1. Normalization of hypsometric curves

The normalization of the hypsometric curves is performed as in Equations 1.1 and 1.2. To make sure to exclude measuring errors and the normalization is only done for data above a maximum depth of -50m NAP and the level of MHW defined for each tidal basin. H_{min} is thus the maximum depth present in the data above -50m NAP. The values for the MTR are based on recent settings used for the ASMITA modelling and Elias et al. (2012), and can be found in table 2.2. MHW and MLW are then calculated by equations 2.1 and 2.2. Note: These values for MTR, MHW, and MLW are used for normalization for all time-steps and sub-sections. This means that in this research there is no detailed spatiotemporal variation in tidal range.

$$MHW = \frac{MTR}{2} \tag{2.1}$$

$$MLW = -\frac{MTR}{2} \tag{2.2}$$

Table 2.2: MHW values used to bound the hypsometric curves for further analysis. Based on the settings in ASMITA (Elias et al., 2012; Huismans et al., 2022)

Marsdiep	**Eierlandse Gat**	**Vlie Inlet**	**Ameland Inlet**	**Pinkegat**	**Zoutkamperlaag**
1.65	1.9	1.9	2.15	2.15	2.25
Eijlanderbalg	**Lauwers**	**Schild**	**Sparregat**	**Ems-Dollard**	
2.3	2.35	2.4	2.45	2.5	

Scripts:

- *Function_normalized_hypso_bounded.py*

2.4. Calculation of areas, volumes and mean heights of intertidal flats

From the hypsometric curves, the area, volume and height of depth zones can be determined (Wang et al., 2020). The area can be determined by the following equation:

$$A_{depthzone} = A_{max,depthzone} - A_{min,depthzone} \tag{2.3}$$

The volume of sand can then be determined by integrating the hypsometric curve between A_{MLW} and A_{MHW} using scipy.integrate.simps(), which carries out equation 2.4 following Simpson's rule. For this integration, the curve is first transformed to be above zero by adding the minimum depth to each bin and only cutting out the depth zone part of the curve.

$$V_{depthzone} = \int_{H_{\text{min, depth zone}}}^{H_{\text{max, depth zone}}} h(A)\, dA \tag{2.4}$$

The height of the depth zone is calculated relative to the minimum elevation of the depth zone:

$$H_{depthzone} = V_{depthzone} / A_{depthzone} \tag{2.5}$$

The volume of water that is in the depth zone can also be determined:

$$V_{water,depthzone} = A_{depthzone} * (H_{max,depthzone} - H_{min,depthzone}) - V_{sand,depthzone} \tag{2.6}$$

For calculations of the intertidal flats, MLW and MHW as defined in equation 2.1 and 2.2 are used for $H_{min,depthzone}$ and $H_{max,depthzone}$ respectively. Note: H_f is thus defined relative to MLW (as in Wang et al. (2020)) and **not** relative to NAP. With equation 2.6 for example the tidal prism can be determined with $H_{max} = MHW$ and $H_{min} = MLW$.

The calculations are done for all full- and sub-section grids for the intertidal flats.

Scripts:

- *Function_vol_sand_of_depth_zone.py*
- *Function_vol_water_of_depth_zone.py*
- *Function_area_of_depth_zone.py*

2.5. Fitting of theoretical curves

Fitting to the curve generated from the histogram is biased towards the deeper part of the considered curve because the density of data points is higher as they are evenly spaced on the y-axis (elevation). This is not preferable for the focus on the intertidal area in this research. Therefore, the data are linearly interpolated the data so that the curves are evenly spaced on the x-axis, causing a higher density of points in the shallow part of the hypsometric curve. This leads to a fitting that is stronger influenced by the shallow parts of the basin and therefore more applicable for representation of the intertidal flats.

Parameterization of hypsometry is done by finding the best fitting theoretical curve. A range of curves is fitted to the data using the scipy.optimize.curve_fit function (see Appendix B.1), which calculates optimal fitting parameters. The range of curves is based on the theoretical definitions mentioned in Chapter 1. For finding this curve, the full basin grids for the entire time-span present in the dataset are used.

The quality of the fits is determined by least root-mean-square error (RMSE) fitting as suggested in Leuven et al. (2018) and additionally their ability to accurately represent the intertidal area and volume is evaluated. For this second part, fitted curves are calculated back to absolute elevation values using the lower and upper boundary that were used for normalizing the curves in the first place. From these curves, the area and volume of the intertidal flats are calculated by integrating between MLW and MHW (Equation 2.4). Comparing these values with the measured values shows how accurate the theoretical curves are in representing the intertidal flats.

2.5.1. Simplification of theoretical curves

For further analysis, it is preferable to reduce the amount of free parameters in the fitting curve. This can be done through three methods. Firstly, it is possible to fit with

fixed parameters as in (Leuven et al., 2018). Alternatively, parameters can be omitted by parameter correlation; after fitting, identifying correlations between the fitting parameters might indicate linear relations, which could then be used to interchange parameters in the fitting function. Lastly, for functions with quadratic terms, it is possible to calculate the discriminant of this term as an indicator of concavity-convexity. The discriminant is calculated as follows:

$$\begin{aligned} \text{Example denominator:} \quad & Ax^2 + Bx + C \\ \text{Discriminant} \quad & B^2 - 4AC \end{aligned} \tag{2.7}$$

Higher values for the discriminant indicate higher convexity, lower values indicate concavity (Fig. 2.5). The c parameter affects the degree of curvature in the upper part of the curve, while d affects both the degree of curvature in the middle of the curve and the direction of this curvature. The complete description of the concavity-convexity of the rational curve is formed by the combination of the c parameter, d parameter, and the discriminant.

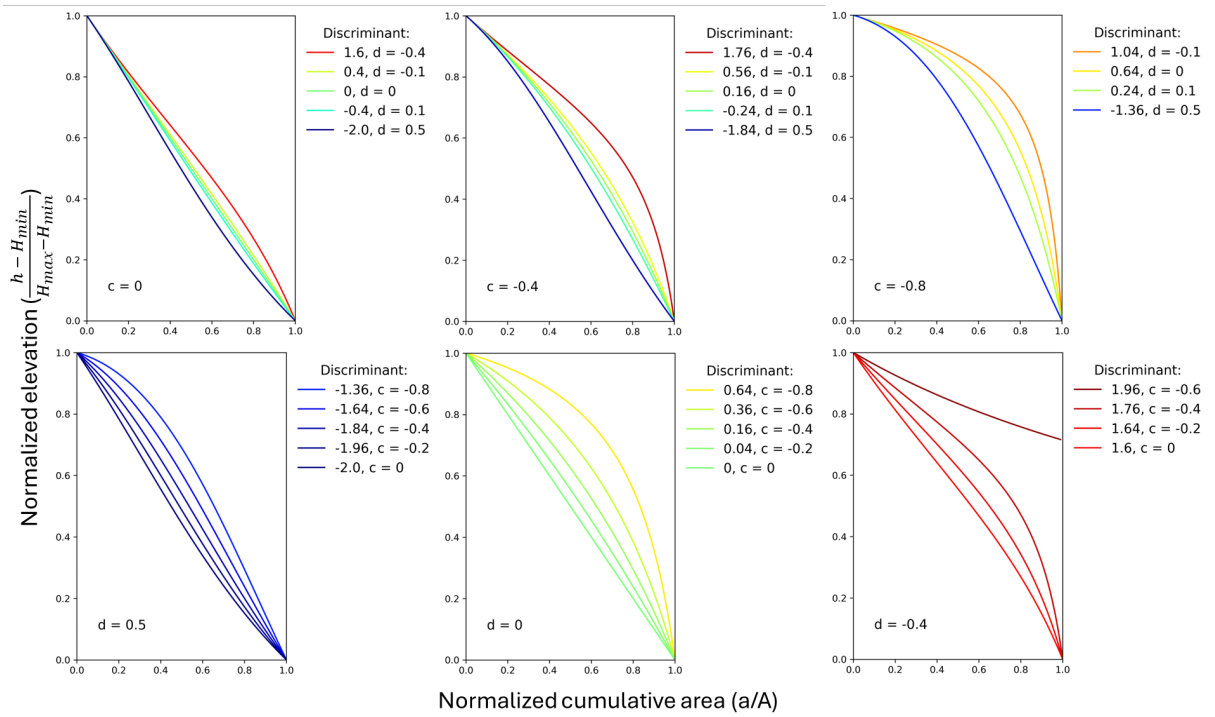

Figure 2.5: Curve concavity-convexity under changing discriminant with changing c and d parameters. Examples for the rational curve (Sarkar & Patel, 2011) with a = 1 and b = -1.

Parameterization for the sub-section hypsometry is done with the theoretical curve that best fits the full basin grids. Additionally, the Strahler curve is fitted to the Ems-Dollard estuary sub-sections to compare the results with the approach taken in Leuven

et al. (2018).

Scripts full basin fitting:

- *Function_respacing_normcurve.py*
- *Function_fitting_curves.py*
- *Function_fit_boon_curve.py*
- *Function_fit_gen_curve.py*
- *Function_fit_inv_and_strahler_curve.py*
- *Function_fit_log_curve.py*
- *Function_fit_rat_curve.py*
- *Function_fit_sig_curve.py*
- *Function_fit_yield_curve.py*
- *Function_fit_rat_curve_simplified_TB_ED.py*
- *Function_area_of_depth_zone.py*
- *Function_vol_sand_of_depth_zone.py*
- *Function_vol_water_of_depth_zone.py*
- All scripts that start with '*Fitting_...*" and contain "*long_term*"

Scripts sub-section fitting:

- All scripts that start with '*Fitting_...*" and contain "*short_term*"

2.6. Mapping the results

The outcomes are summarised into maps for spatial visualisation. To do this, dictionaries with the empirical variables (Hf, Af/Ab, Vf/Vb) from the hypsometric curves and with the parameters from the best-fitting curve are created. The mean and gradients over time of each variable are then calculated and stored in new dictionaries. Using the keys and subs in the defined dictionaries, .TIFF files of the associated (sub)grids are opened using the rasterio package (Gillies, 2019) and its bathymetric data are overwritten with the calculated variable. The sub-sections are then merged back together again and saved in the defined output folder. For the approaches where the basins are also cut in half this is done for all basins for each half and afterwards the grids for the

halves are again merged together.

Scripts:

- *Creating_resultmaps_fullandhalf_short_term_4param_rational.py*
- *Creating_resultmaps_fullandhalf_short_term_annular_4param_rational.py*
- *Merging_grids_results_half_grids_(alsoannular).py*

3. Results

The first part of the results contains examples of hypsometric curves, the influence of resolution on these curves and shortly explains the results of finding the best fitting curve and how parameterization is used in further analysis. Then, spatiotemporal patterns in hypsometry and intertidal flats between and within the tidal basins are shown. In addition, spatiotemporal trends in the Ems-Dollard estuary are presented.

3.1. Example of (normalized) hypsometric curves

An example of hypsometry is shown for the entire Marsdiep tidal basin over time. Figure 3.1(a) shows the hypsometric curve between -15 and 2m NAP. Figure 3.1(b) shows the same curve, but zoomed in on the intertidal area. Figure 3.2 shows the normalized hypsometric curve for the Marsdiep basin over time. The curves for all basins can be found in A.2 and A.3.

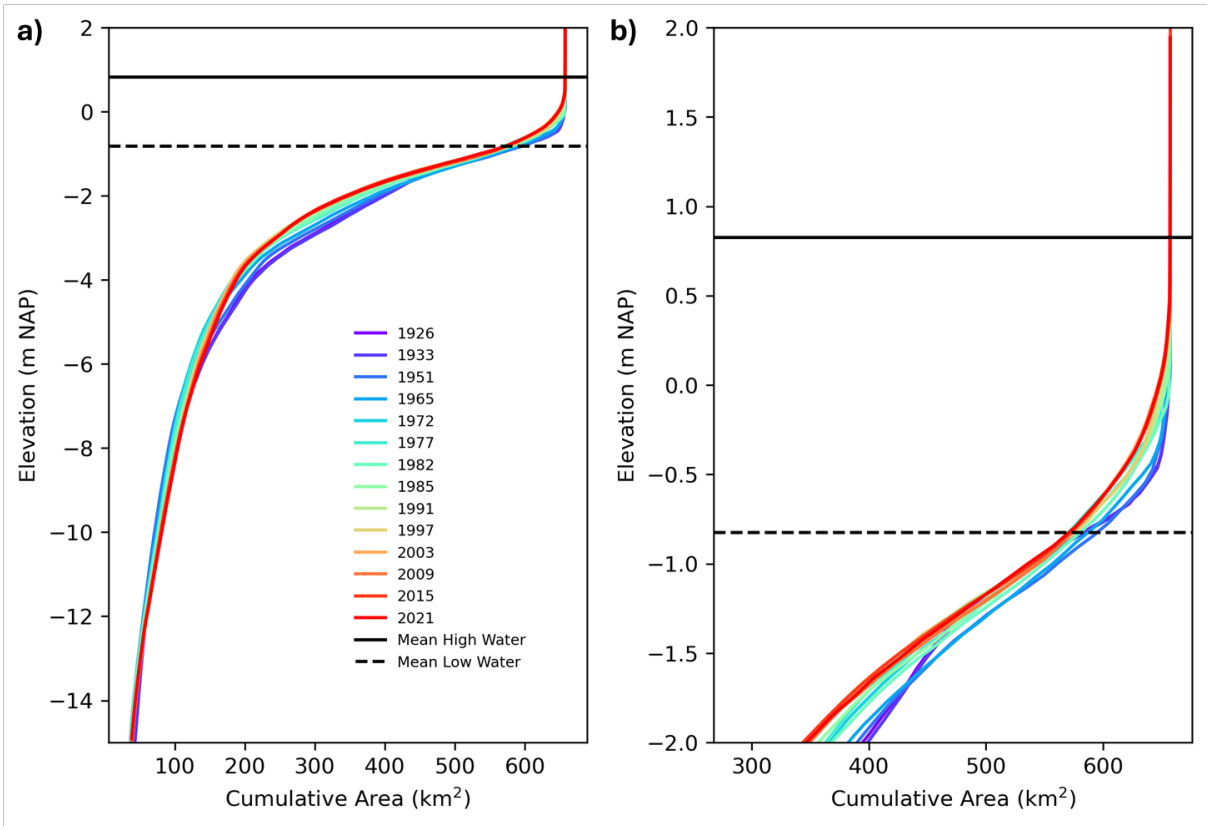

Figure 3.1: Hypsometric curve through time for the Marsdiep basin between a) -15m NAP and 2m NAP and b) -2m NAP and 2m NAP.

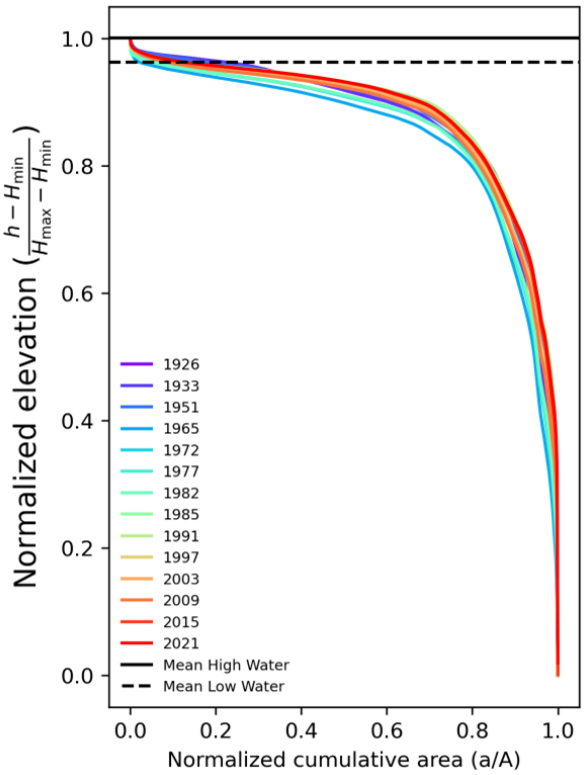

Figure 3.2: Normalized hypsometric curve between the maximum depth (>-50m NAP) and MHW for the Marsdiep basin.

3.1.1. Influence of grid resolution on hypsometric curve

The influence of grid resolution is greater for smaller basins as the smoothing effect is strongest and the small basins contain smaller elevation ranges (Fig. A.29, 3.3, 3.4). The error in the presence of area of intertidal flats is smaller with increasing basin size (Fig. 3.3), but can be up to 30% in small basins. The normalized curve shape is strongest influenced for the Eierlandse Gat, Pinkegat, Lauwers, Schild, and Sparregat basins (Fig. A.29). Influence on fitting parameters is not included, as the effect in normalized curve shape is magnified by area losses at the edges of the grid during down scaling and therefore fitting errors would not representative.

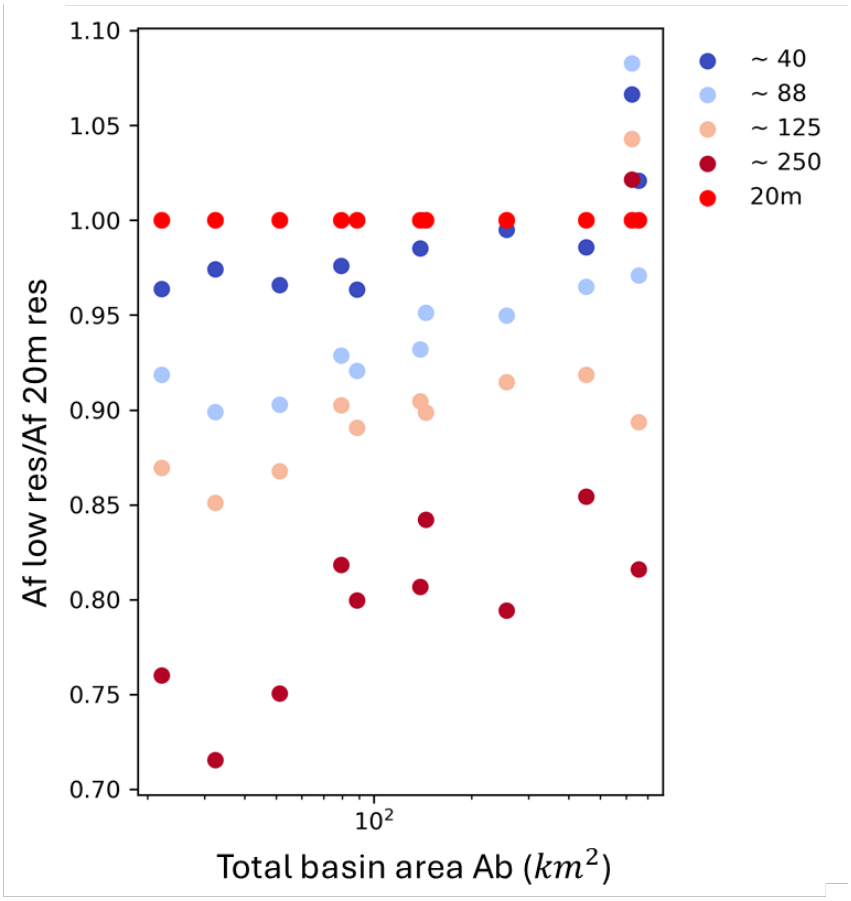

Figure 3.3: Ratio between intertidal flats down scaled resolutions and high resolution grids versus basin size.

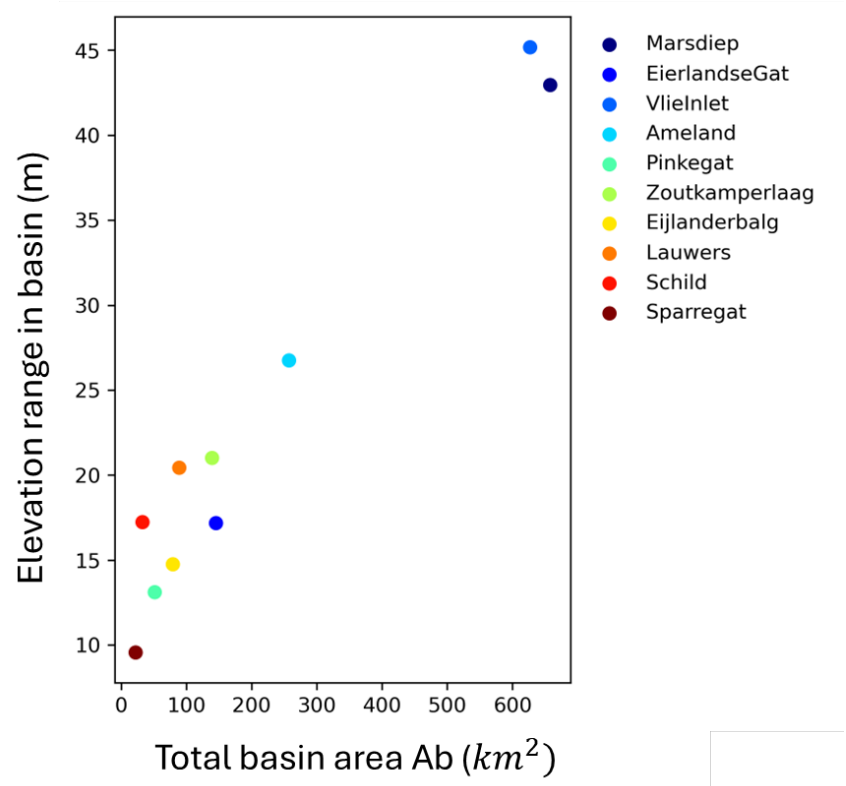

Figure 3.4: Elevation ranges hypsometry between MHW and maximum depth (>-50m) NAP versus total basin area.

3.2. Parameterization of hypsometry; finding and using the best fitting curve

The rational curve from Sarkar and Patel (2011) is the best fitting curve for the full tidal basin dataset of the Dutch Wadden Sea. Only the original Strahler curve (Strahler, 1952), the Boons curve from Boon III and Byrne (1981), the generalized curve from Bajracharya and Jain (2021), and the rational curve from Sarkar and Patel (2011) are able to produce a curve that starts at (1,0) with RMSE values below 0.1 for the full basin data set (Fig. A.34-A.37).

The rational curve is the only curve that in addition is able to approximate the area and volume of the tidal flats within a factor 2 of the measured values. The only exceptions are some volume approximations for the Marsdiep basin. Therefore, the parameters of the rational curve (Sarkar & Patel, 2011) are used in a further analysis. In general, the intertidal area is better approximated by the theoretical curves than the volume (Fig. 3.5). Furthermore, the approximation of area and volume of tidal flats is least accurate in the Marsdiep and Vlie basins.

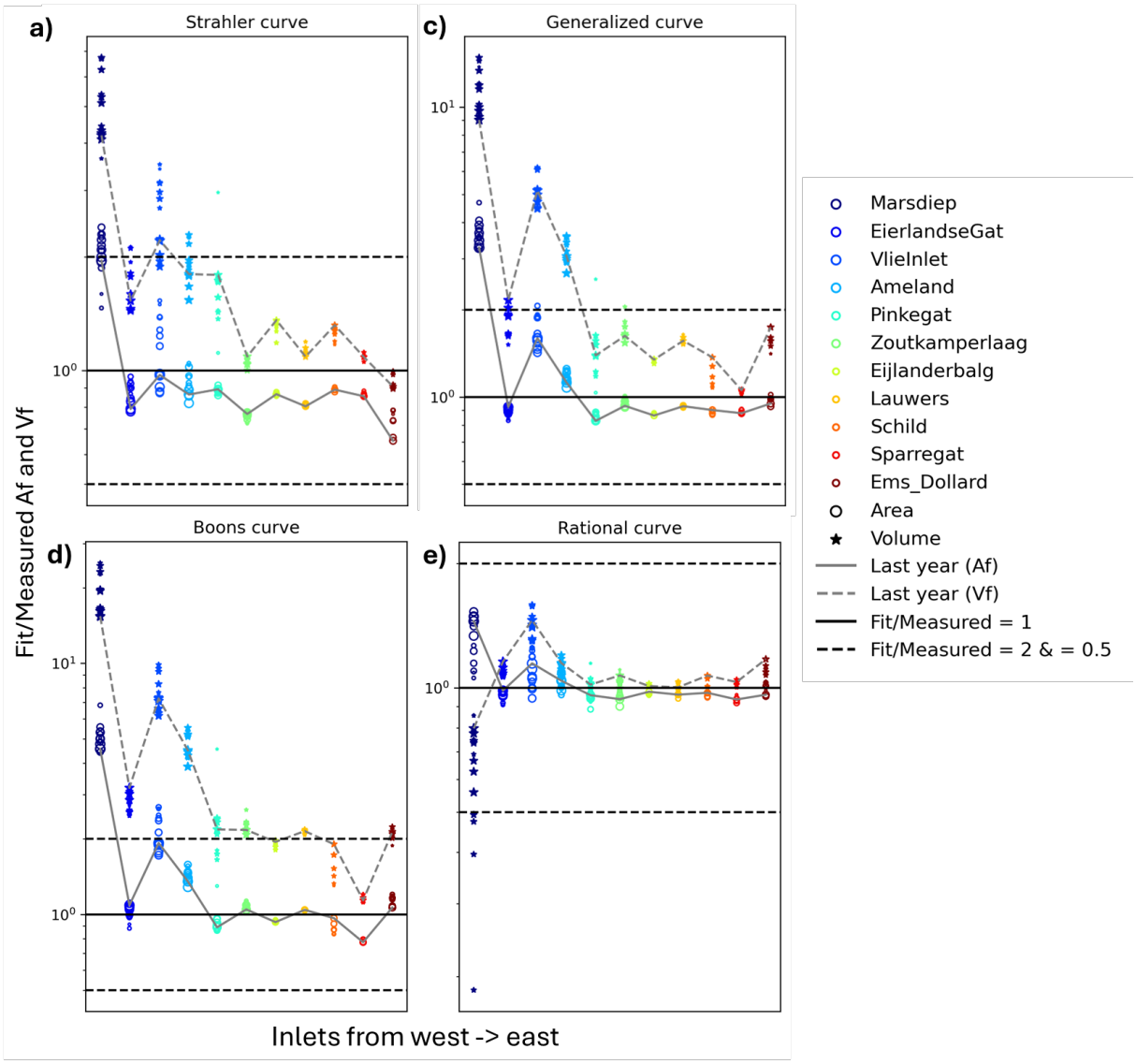

Figure 3.5: Ratio fit over measured for area and volume of intertidal depth zone. Marker size increases with time.

3.2.1. Rational curve; description and simplification

The rational curve contains four parameters, which influence the shape of the curve as in Figure 1.12. The a parameter mainly affects the vertical position of the curve without changing its shape, and b mainly affects the steepness of the curve by affecting the linear extent on the x-axis together with the minimum value on the y-axis. Higher absolute values for b indicate a steeper slope and vice versa. The a and b parameter both influence the minimal extent on the y-axis so it can be expected that after fitting to the hypsometric curves, these parameter show a correlation. The c parameter describes the linear term of the equation and influences the steepness at the top of the curve and the

degree of curvature. The *d* parameter mainly influences how pronounced the curve is in the middle and bottom of the curve and the direction of this curvature. As the parameters *c* and *d* influence both the convexity and concavity of the curve, it can be expected that they are correlated when fitting to the hypsometric curves.

Simplification of the rational curve through fitting with fixed parameters as in Leuven et al. (2018) for the full-basin grids is included in Appendix A.6.1. The *a* and *b* parameters stay rather constant for all fitting curves (Fig. A.37). However, when fixing these values to *a* = 0.98 and *b* = -0.98 for example, the approximations of the intertidal area and volume are no longer accurate for the annular sub-sections of the basins (Fig. A.39). The magnitude of these fixed values is sensitive to the underlying data, which makes it difficult to apply in fitting to sub-sections of the basins. This approach is not further included in the results of the analysis.

Through parameter correlation, the rational curve can be simplified to contain only two parameters through parameter correlation (see Appendix A.6.2 & A.6.3). The correlograms in Appendix A.6.2 and A.6.3 show linear relations between the parameters, with quality of fit indicated by R^2 and in the correlation matrices the *Pearson correlation coefficient (r)*. R^2 ranges from 0 to one and gives the proportion of the variation in the y variable explained by the variable x, whereas *r* gives the direction and strength of linearity in this relationship. Together, these give insight into which parameter correlations can best be used to simplify the rational curve. Correlations and steps in simplification can be found in appendix A.6.

Resulting simplified curves differ for the tidal basins and the Ems-Dollard estuary, indicating different hypsometries for tidal basins and estuaries. This difference is clearly visible from Figure 3.6; the Ems-Dollard estuary exhibits a distinctly more concave shape compared to the tidal basins. Therefore, further results are separated for the tidal basins and the Ems-Dollard estuary.

For the tidal basins, the most simplified version of the rational curve is this:

$$\frac{h - Hmin}{Hmax - Hmin} = \frac{a - 0.97ax - 0.02x}{1 + cx - 0.99cx^2 - 0.95x^2} \tag{3.1}$$

For the Ems-Dollard estuary, this is the most simplified equation:

$$\frac{h - Hmin}{Hmax - Hmin} = \frac{a + bx}{1 + 6.15ax - 6.90x - 7.04ax^2 + 7x^2} \tag{3.2}$$

Simplification through parameter correlation also showed to be very sensitive to the underlying data. Therefore, this approach is not applicable for fitting to curves of sub-sections of the basins. The results of the fitting with simplified curves are included only for the full-basin spatial analysis.

The third method of simplification is by calculating the discriminant of the quadratic denominator of the rational curve as mentioned in Section 2.5.1, calculated through Eq. 2.7. This discriminant gives an indication of the concavity-convexity of the fitted curve; higher values indicate greater convexity. Furthermore, the c parameter indicates the degree of curvature in the upper part of the curve and the d parameter mainly determines the degree of curvature in the middle of the curve and the direction of the curvature (Fig. 2.5). This is the only simplification for which the four-parameter rational curve can be used in a similar way for each approach of either full-basin or sub-section curve fitting. Therefore, the results in this research are based on curve simplification through the discriminant of the denominator, while additionally considering the trends in the c and d parameters. Quality of fit for sub-sections of the tidal basins can be found in Appendix A.7.

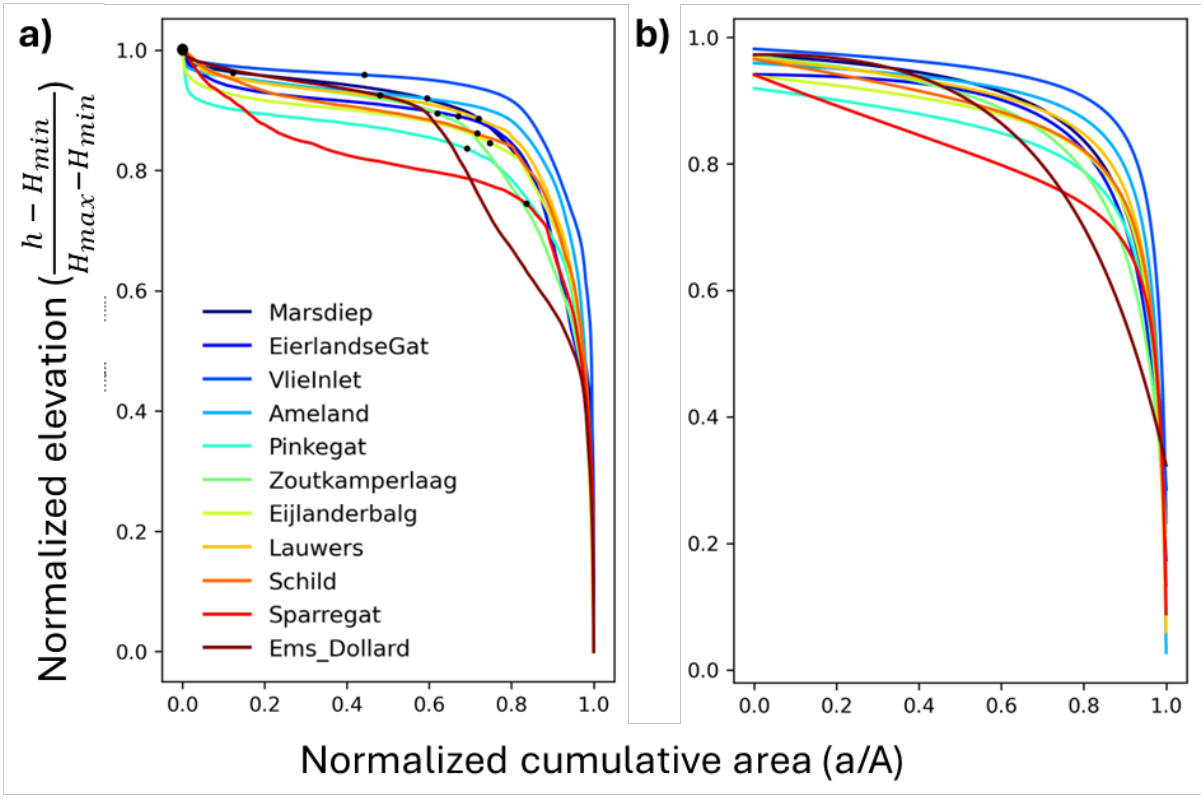

Figure 3.6: Hypsometric curves for the last time steps of each considered grid normalized between the maximum depth (>-50m NAP) and MHW (a) and the resulting fitted rational curve (b).

3.3. Spatial and temporal patterns in hypsometry between tidal basins

No clear trend is found from west to east in the fitted *a* and *c* parameters of the simplified rational curve (Fig. 3.7), whereas an increasing trend in convexity is visible from the discriminant and parameters of the four-parameter rational curve (Fig. 3.8 & 3.9). This shows that the two-parameter version does not capture the same trends as the four-parameter rational curve.

From west to east, the degree of curvature and convexity increase, which can be seen from the increases in the *c* parameter and discriminant along with a decrease in the *d* parameter (Fig. 3.8(c,d), 3.9 & 2.5). An eastward increase is also visible in intertidal flats characteristics in the basins; from west to east the tidal flats become larger in relative area, volume and mean height (Fig. 3.10). In this pattern, the Marsdiep exhibits low relative flat area and the Eierlandse Gat deviates from the general trend with a much higher *Af/Ab* (Fig. 3.10(a)). In relative flat volume, the Marsdiep is again low, but closer to the general west-east trend, whereas the Eierlandse Gat is again much higher (Fig. 3.10(b)). The eastern basins have higher flats than the basins in the western Wadden Sea (Fig. 3.10(c)).

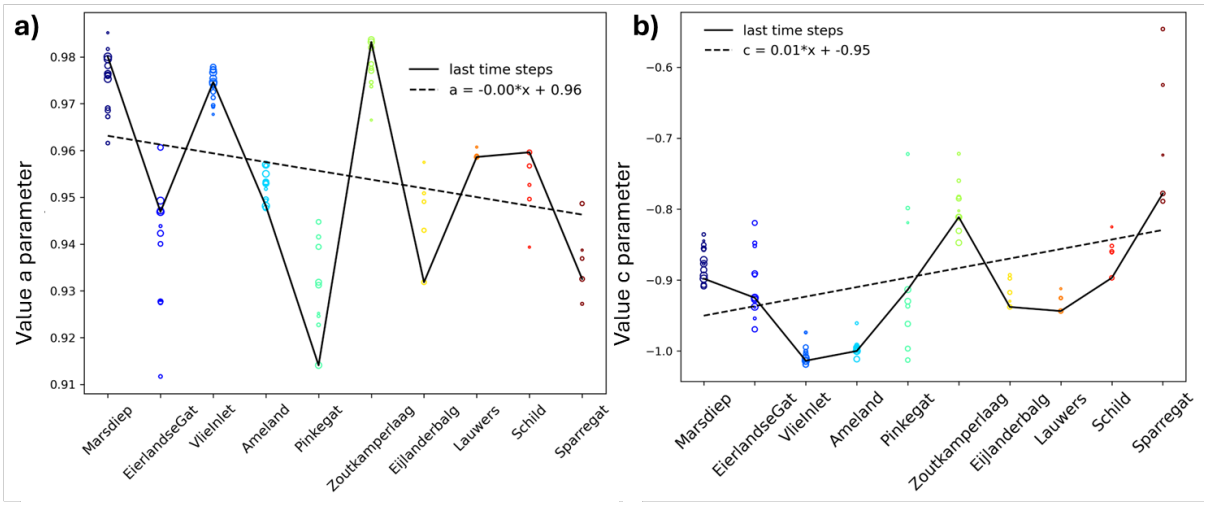

Figure 3.7: Spatial west-east trends of *a* & *c* parameters of the simplified rational curve for the full tidal basins.

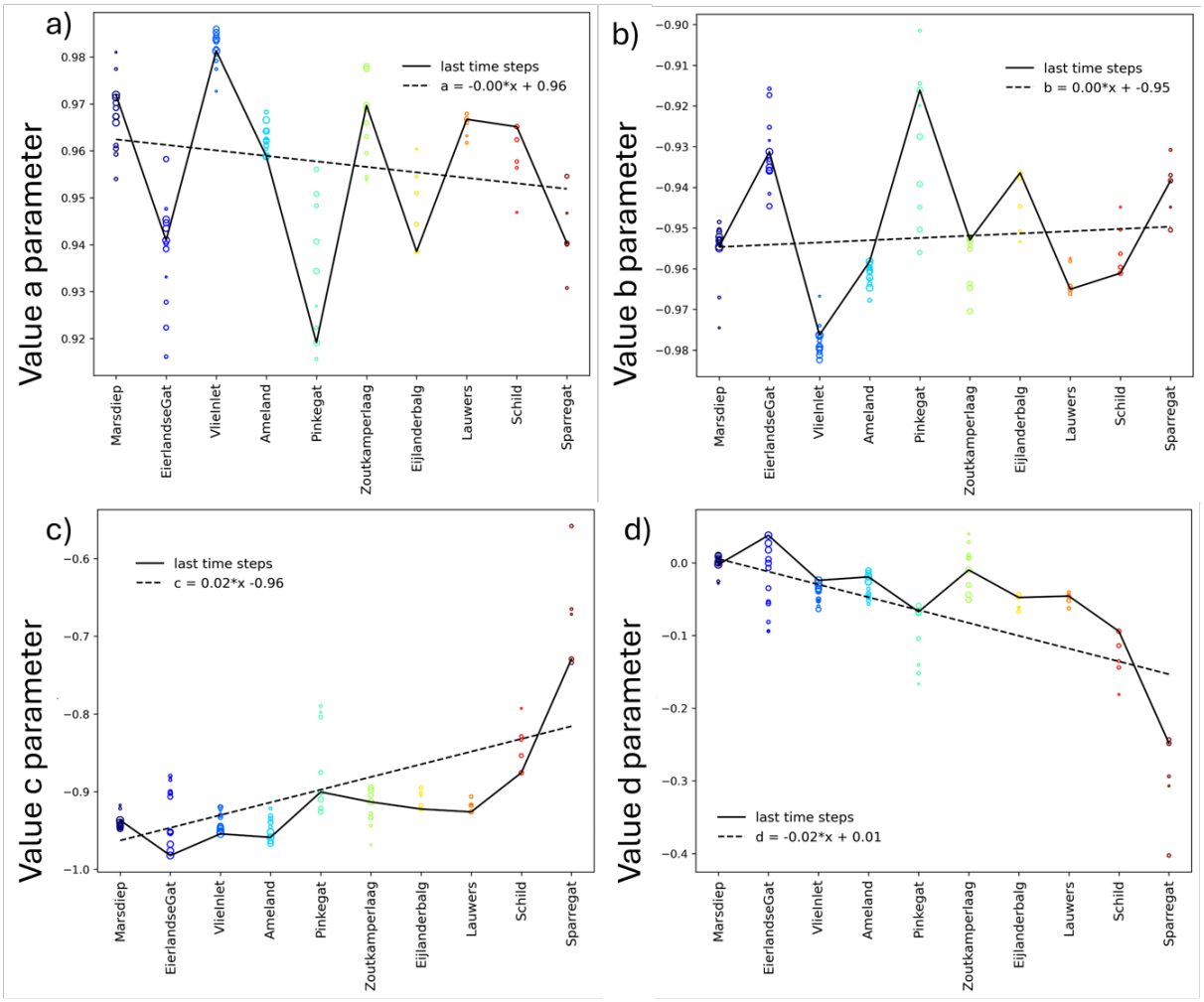

Figure 3.8: Spatial west-east trends in *a*, *b*, *c*, and *d* parameters of the four-parameter rational curve.

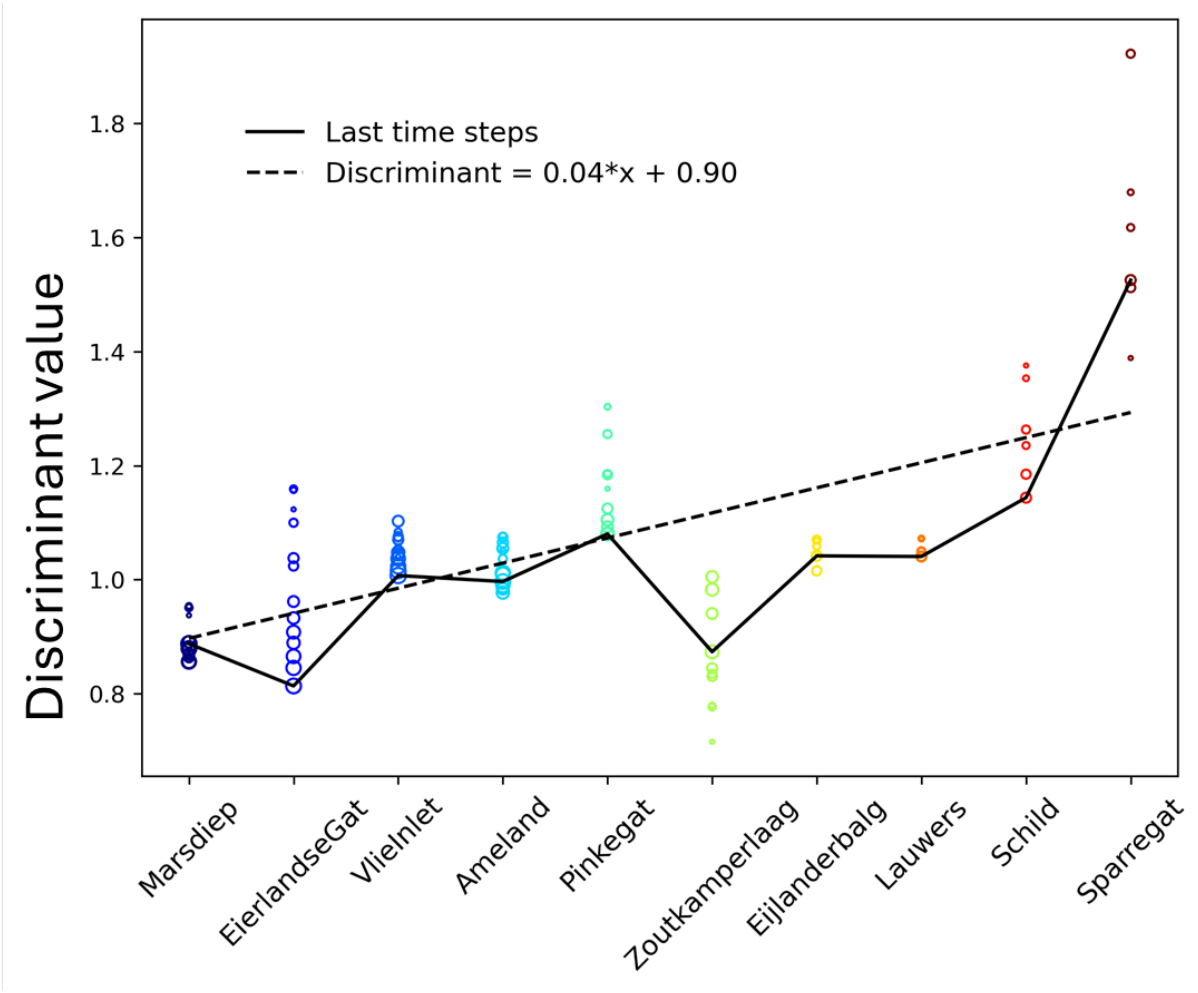

Figure 3.9: Eastward increasing convexity in the discriminant of the denominator in the four-parameter rational curve. The trend line was fitted to guide the eye, but was not intended as a further data reduction. Marker size increases with time.

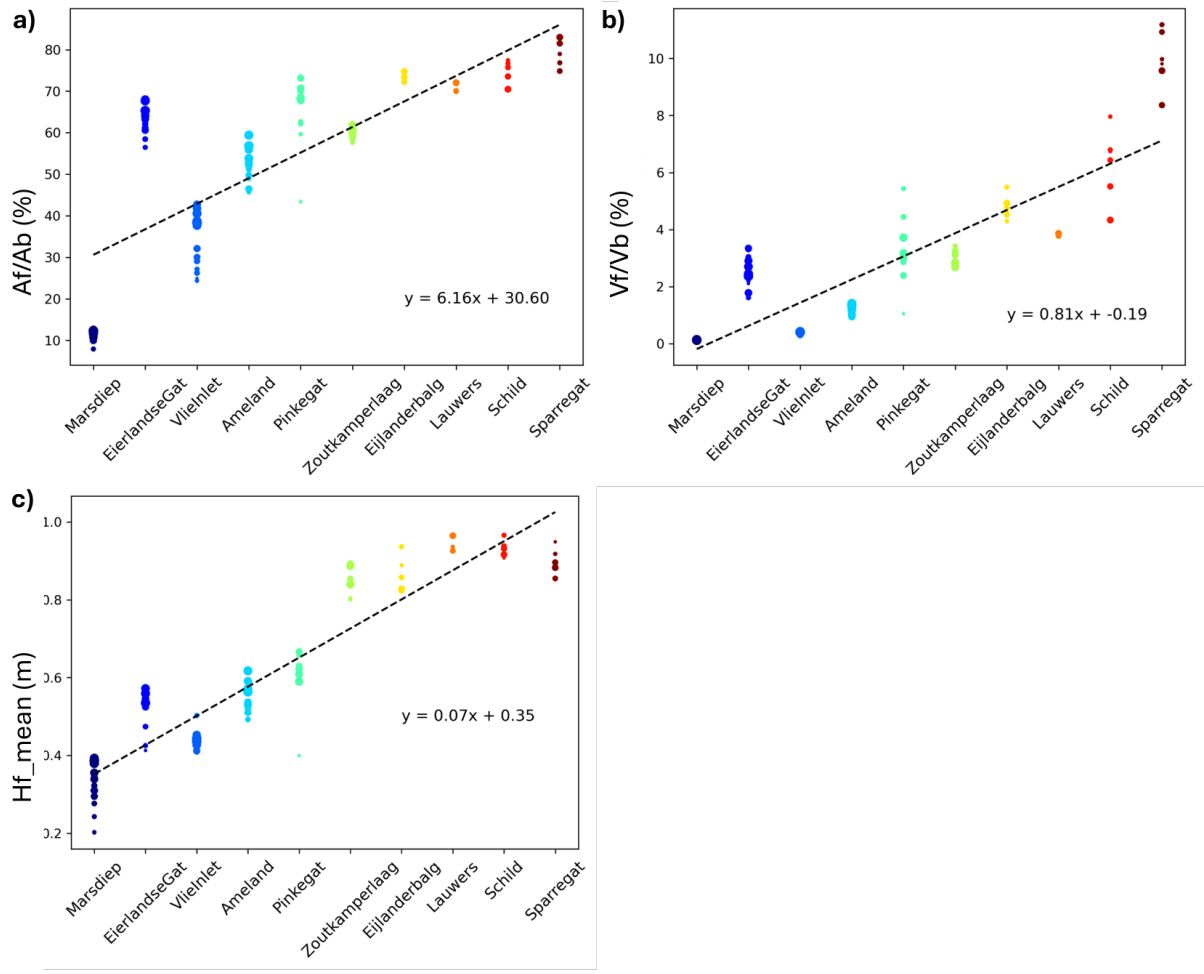

Figure 3.10: Eastward increasing trends of relative flat area (a), relative flat volume (b) and mean flat height (c) for the full tidal basins. Trend lines were fitted to guide the eye but not intended as further data reduction.

Over the past century, convexity increased or stayed rather constant over time for most basins, except for the Eierlandse Gat and Schild basins in which decreasing trends are visible (Fig. 3.11). Over time, the Eierlandse Gat, Pinkegat, Zoutkamperlaag, and Sparregat basins are most variable in curve shape, reflected in a wider spread in fitting parameters (Fig. 3.8). The hypsometric curve (Fig. 3.11) exhibits an increase in convexity over time, but the variation in curve shape is generally small for the Marsdiep basin. For the Eierlandse Gat, decreasing convexity is visible over time. This is in contrast with the increasing trends in tidal flat properties (Fig. 3.12).

The Vlie and Ameland basins show a minor initial increase in convexity until 1950, after which it stays rather constant. The Pinkegat shows an increase in convexity from 1926-1970, after which a decrease is visible, and in the most recent years the discriminant stays rather constant. The Zoutkamperlaag shows an increase over time until

2000 and a decrease in convexity in the most recent years. This decrease can also be seen in mean flat height (Fig. 3.12(c)). As a result of this increase in convexity, the Zoutkamperlaag better fits the eastward increasing trend over time.

The Eijlanderbalg and Lauwers basins are rather constant in convexity over the last 30 years. The Schild basin shows a decrease in convexity. The results for Sparregat vary strongly and do not show a clear trend, which was already visible in the fitting parameters in Figure A.37.

The tidal flat properties (relative area, relative volume and mean height) generally increase slightly over time but show a lot of variation (Fig. 3.12). Temporal variation in the intertidal flat area is greatest for the Eierlandse Gat, Vlie, and Ameland basins, which are all increasing. Conversely, the convexity is decreasing (Eierlandse Gat) or rather constant (Vlie, Ameland) over time. The mean height of the intertidal flats (*Hf*) shows a division between two groups of basins. The basins in the western Wadden Sea (Marsdiep, Eierlandse Gat, Vlie, Ameland, and Pinkegat) have lower flats around 0.5m than the basins in the east from the Zoutkamperlaag onwards ($\tilde{0}$.9m). Furthermore, the basins in the west show overall increasing *Hf* , whereas the basins in the eastern part show varying trends (Fig. 3.12(c)).

There is a discrepancy between the development of tidal flat properties and the convexity described by the rational curve (Fig. 3.11 - 3.12). An increase in intertidal flat properties does not always align with an increase in overall convexity (i.e. Vlie basin) and decreasing convexity does not always align with eroding intertidal flats (i.e. Eierlandse Gat).

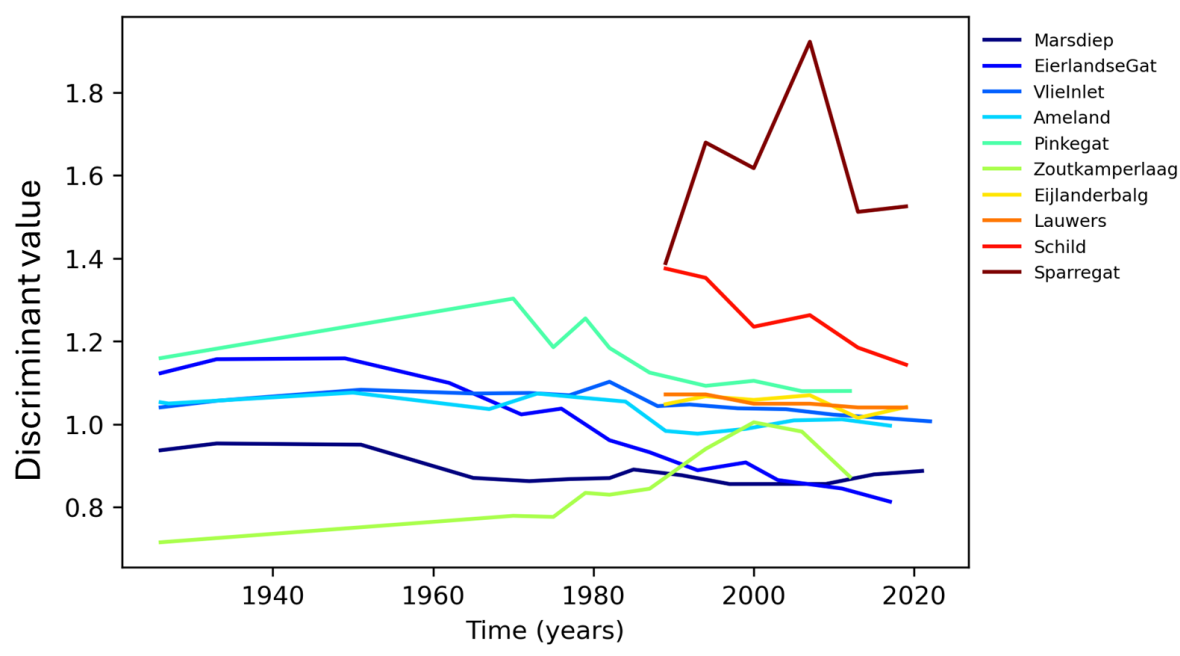

Figure 3.11: Temporal trends in discriminant of the denominator of the four-parameter rational curve.

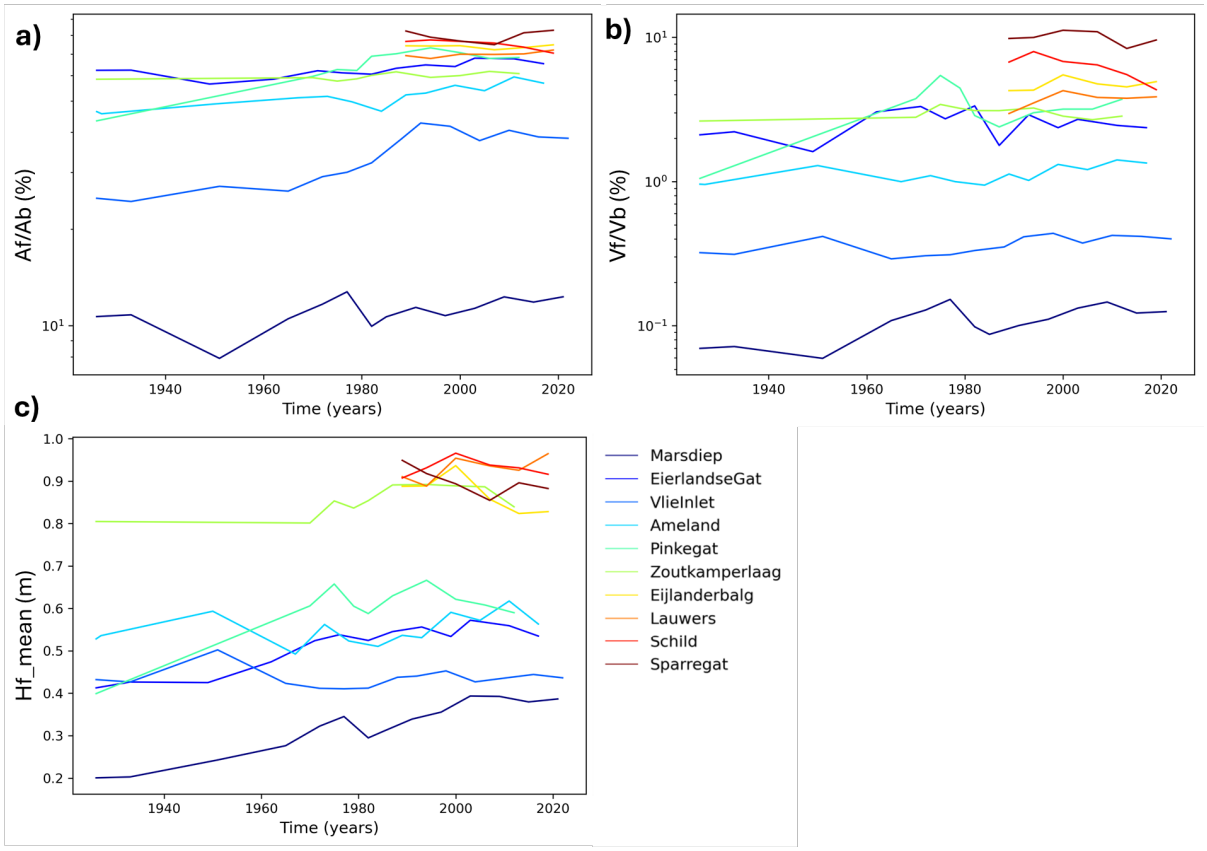

Figure 3.12: Temporal trends of relative flat area (a), relative flat volume (b) and mean flat height (c) for the full tidal basins.

3.4. Spatial patterns in hypsometry within tidal basins

3.4.1. Differences between the western and eastern halves

Differences between basin halves are larger in the eastern Wadden Sea tidal basins (Fig. 3.13). In the western basins, only the Marsdiep exhibits higher convexity in the southern basin half compared to the northern basin half.

The relative area, volume, and height of the intertidal flats is higher in the southern half of the Marsdiep basin (Fig. 3.14). The Eierlandse Gat, Vlie, and Ameland basin do not show strong differences in convexity between basin halves (Fig. 3.13). The properties of the intertidal flats are only slightly higher in the southern (Eierlandse Gat)/western (Vlie & Ameland) basin halves (Fig. 3.14).

In the eastern Wadden Sea, convexity is higher for the eastern half-basins except for the Eijlanderbalg and Sparregat basins (Fig. 3.13). For these two basins, the relative area, volume, and mean height of the intertidal flats are also higher in the eastern halves (Fig. 3.14). The Zoutkamperlaag basin shows a contrast in convexity and intertidal properties; the convexity is distinctly higher in the eastern basin half, whereas the intertidal area and volume do not differ strongly between basin halves (Fig. 3.13(c), 3.14(a,b)). The mean height of the flats is higher in the western half of the Zoutkamperlaag basin (Fig. 3.14(c)).

The relative area and volume of tidal flats is generally higher in the northern/eastern basin halves with the exception of the Marsdiep basin (Fig. 3.14(a,b)). For the mean flat height, it differs which basin half is highest (Fig. 3.14(c)).

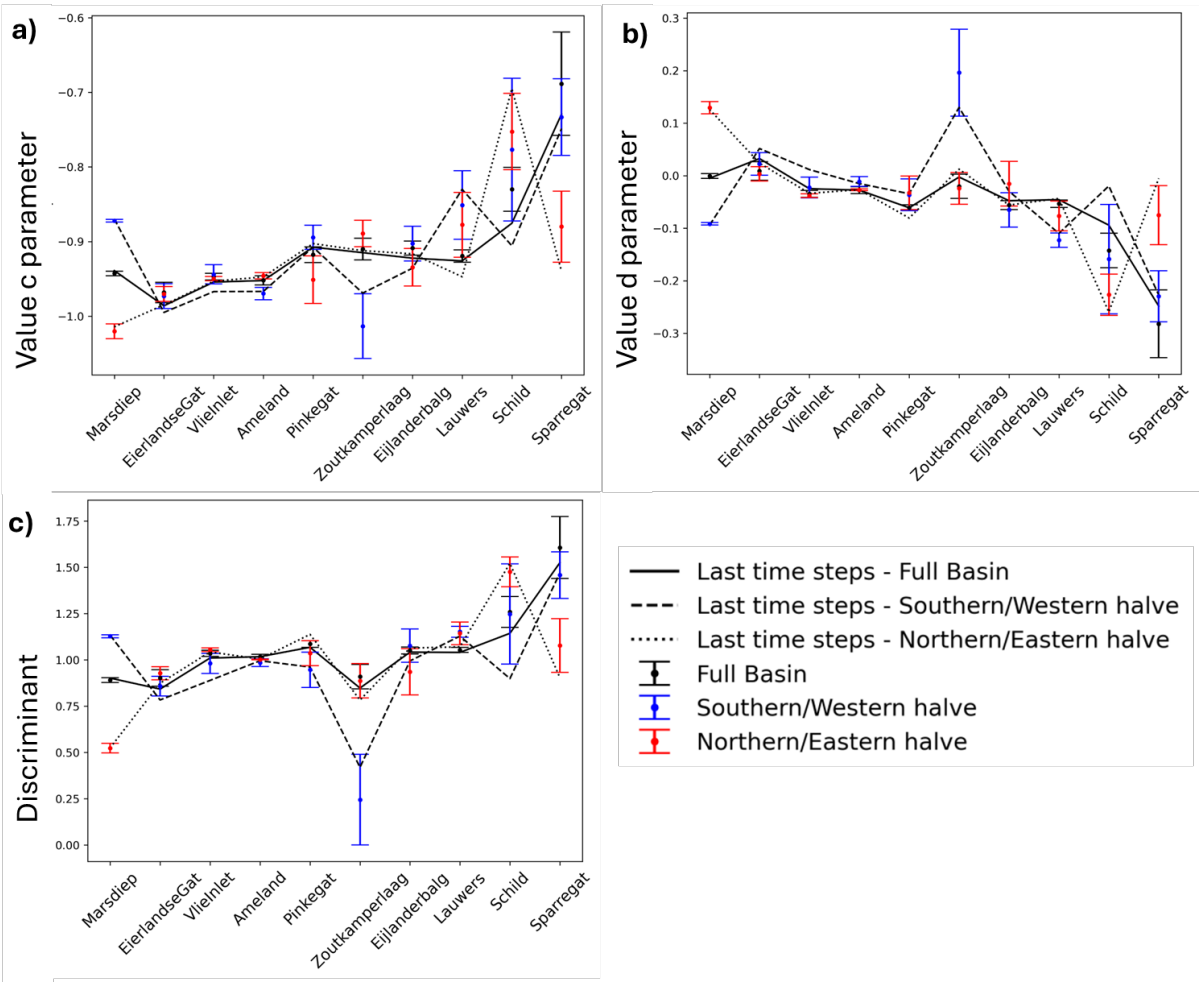

Figure 3.13: Differences between basin halves averaged over time (1985-2022) for the *c* parameter (a), *d* parameter (b), and discriminant (c).

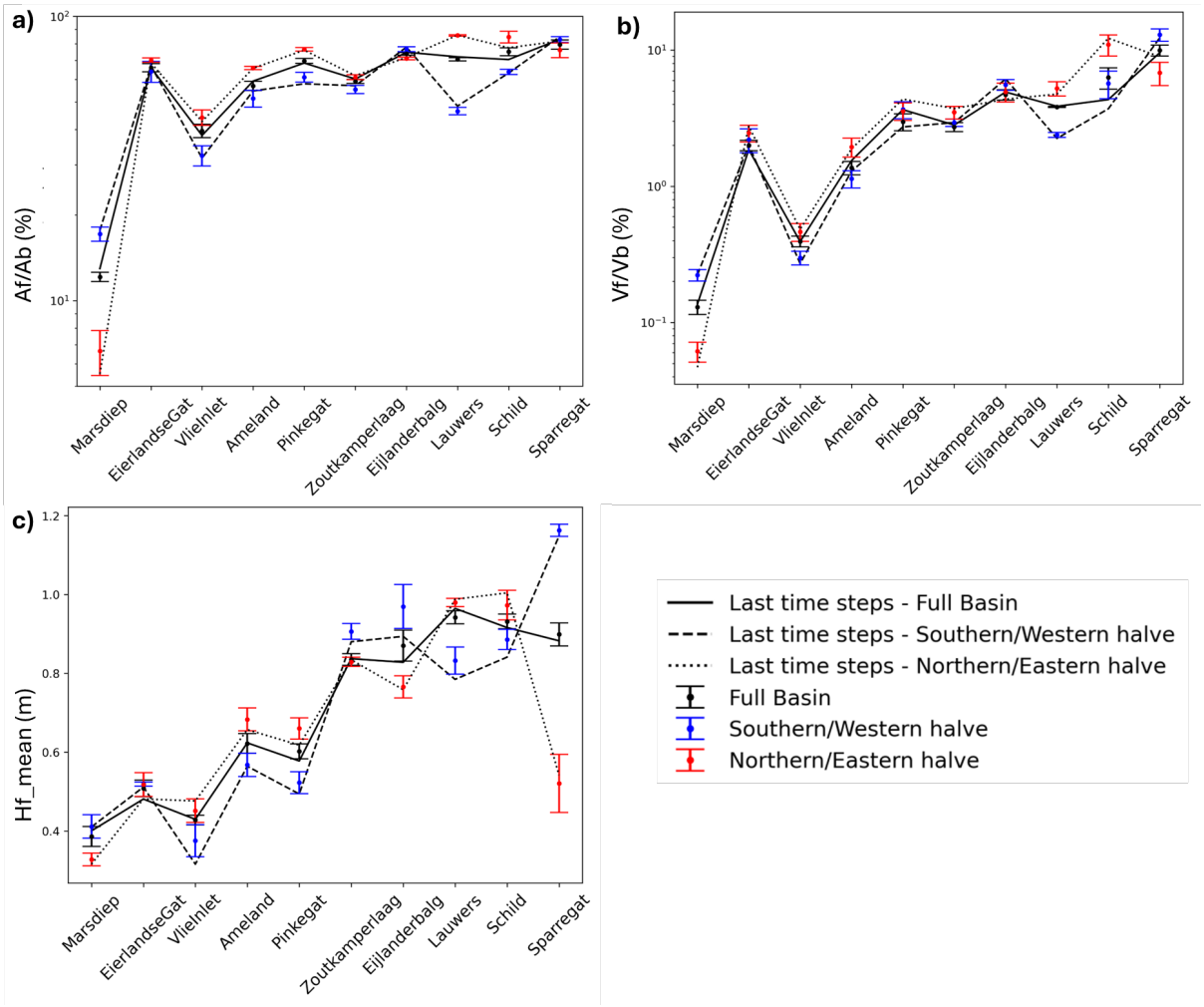

Figure 3.14: Differences between basin halves averaged over time (1985-2022), for the relative flat area (a), and relative flat volume (b), and mean flat height.

3.4.2. Trends with distance from the inlet

Convexity, relative area and volume of intertidal flats increases with distance from the inlet within the tidal basins in the Dutch Wadden Sea (Fig. 3.15 -3.17). The mean height generally decreases with distance from the inlet (Fig. 3.18). The pattern in relative flat area shows a contrasting trend compared to the mean flat height with distance from the inlet.

In terms of convexity, a general trend is observed with the c parameter increasing and the d parameter decreasing. This trend indicates that the curvature becomes stronger and the convexity increases with distance from the inlet. This is reflected in the general increase in the discriminant value with distance from the inlet.

For the Marsdiep the patterns in relative flat area and volume deviate from the

other basins (Fig. 3.16 & 3.17). At 0.1-0.2 distance from inlet/total length basin (D/L), the relative area of flats is highest. For the other annular sub-sections in the Marsdiep *Af/Ab* is below 10%. The Vlie basin also shows a somewhat deviating pattern, where *Af/Ab* stays rather constant from 0.4-0.7 D/L and *Vf/Vb* increases less strongly than compared to the other basins. A weaker increase in relative volume of the intertidal flats is also present for the first half of the Ameland basin (Fig. 3.17).

The mean height of the intertidal flats shows a general decrease with distance from the inlet, but the patterns show some more variation (Fig. 3.18). First, it again becomes visible that the western basins contain lower flats (see Section 3.3). In the Ameland basin the mean flat height increases from 0.5-0.7 D/L, after which it decreases again. For the Zoutkamperlaag, the mean flat height shows variation with distance from the inlet, with no clear trend. Mean flat height is first increasing in the Schild and Sparregat basins, after which it decreases further landward (Fig. 3.18).

The most seaward and landward annular sub-sections show larger standard deviations. The standard deviation around 0.9 D/L for the Ameland basin is much larger than the other basins. For some years, sudden changes to a concave curve shape are present for this annular sub-section.

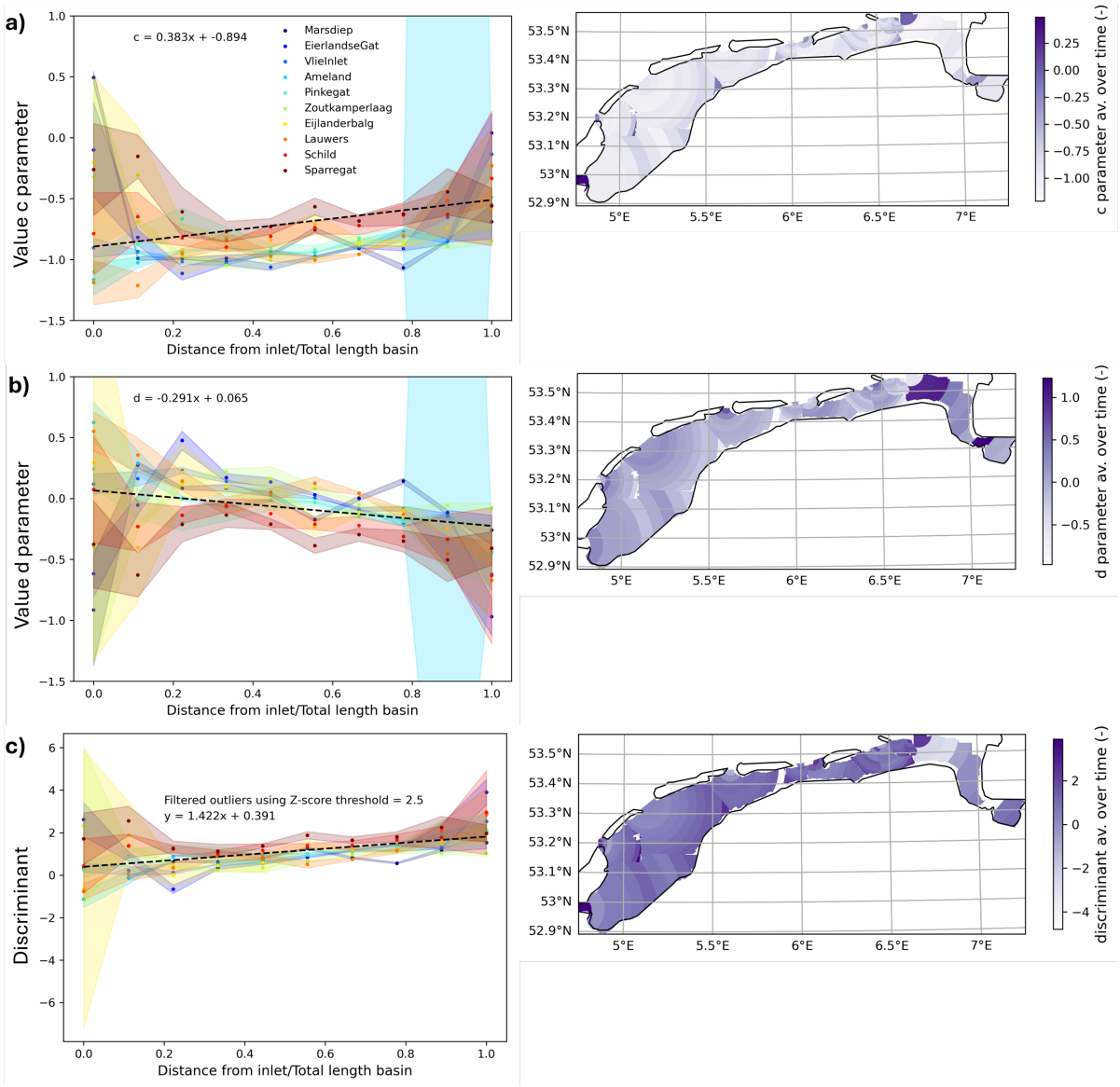

Figure 3.15: Spatial trends of increasing convexity with distance from the inlet for the tidal basins. Patterns in *c* parameter (a), *d* parameter (b), and discriminant (c) of the four-parameter rational curve. Temporally averaged for 1985-2022, shaded regions indicate standard deviations in time.

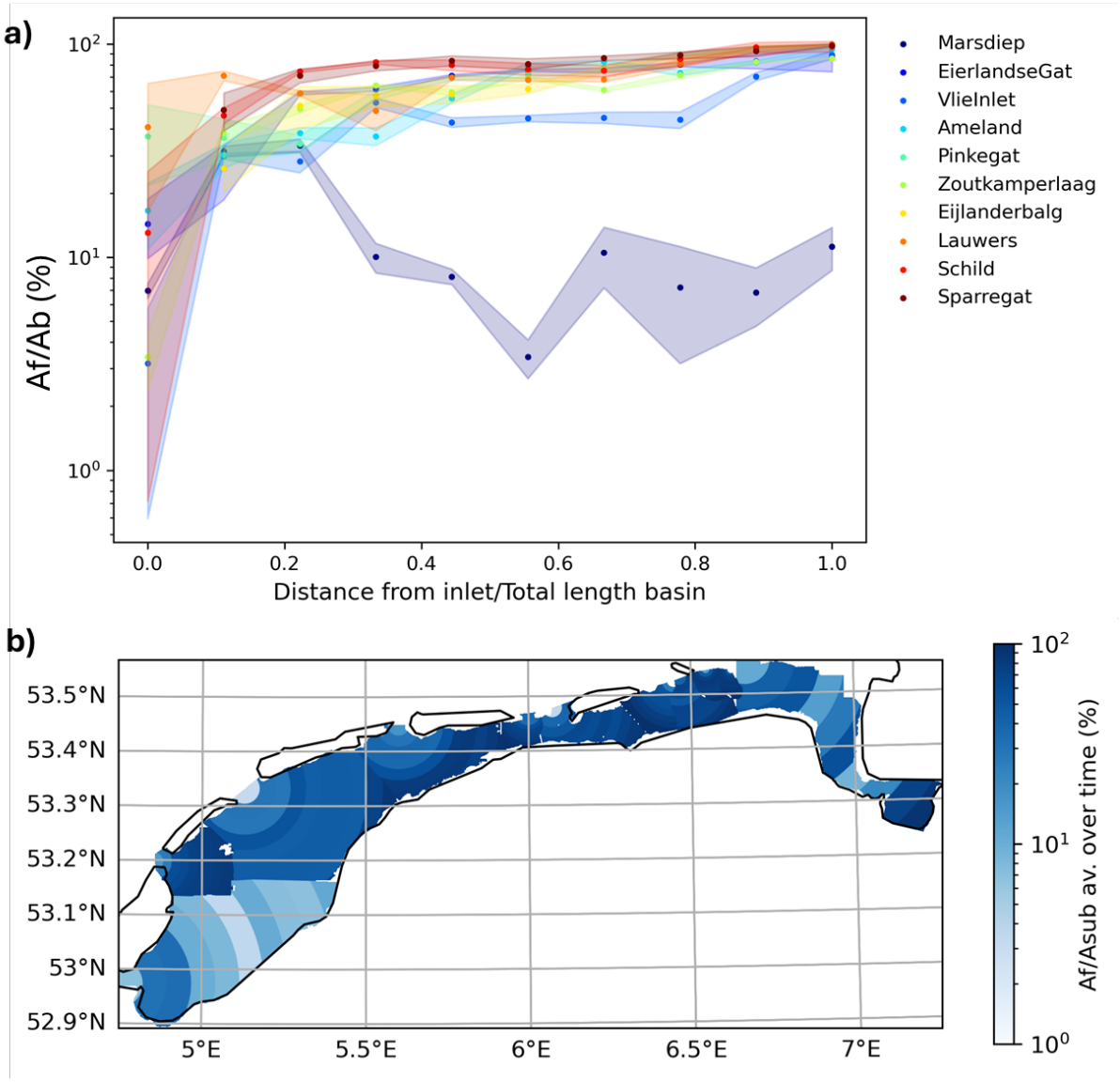

Figure 3.16: Spatial trends in relative area of intertidal flats with distance from the inlet within the tidal basins. Temporally averaged for 1985-2022, shaded regions indicate standard deviations in time.

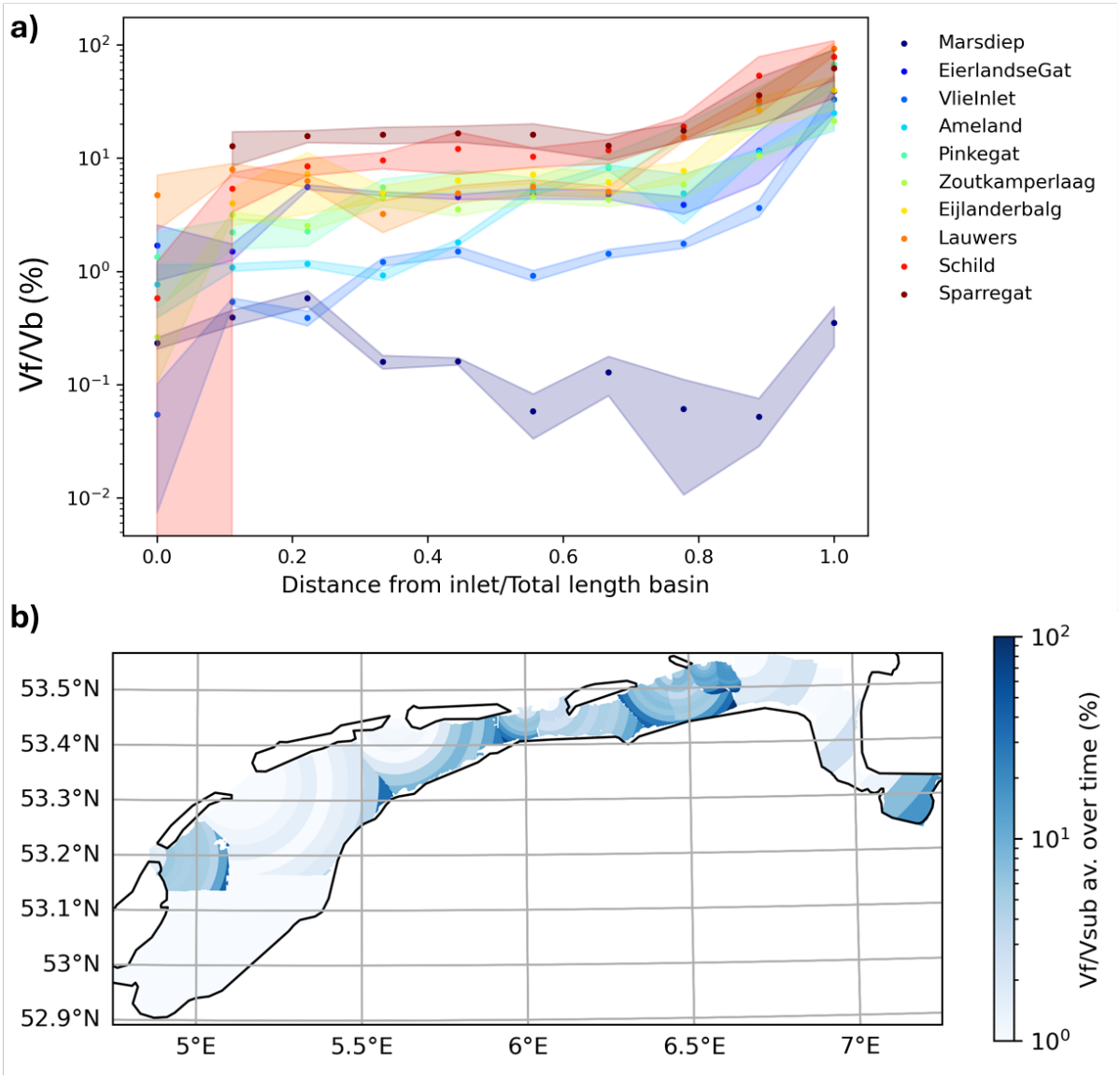

Figure 3.17: Spatial trends in relative volume of intertidal flats with distance from the inlet within the tidal basins. Temporally averaged for 1985-2022, shaded regions indicate standard deviations in time.

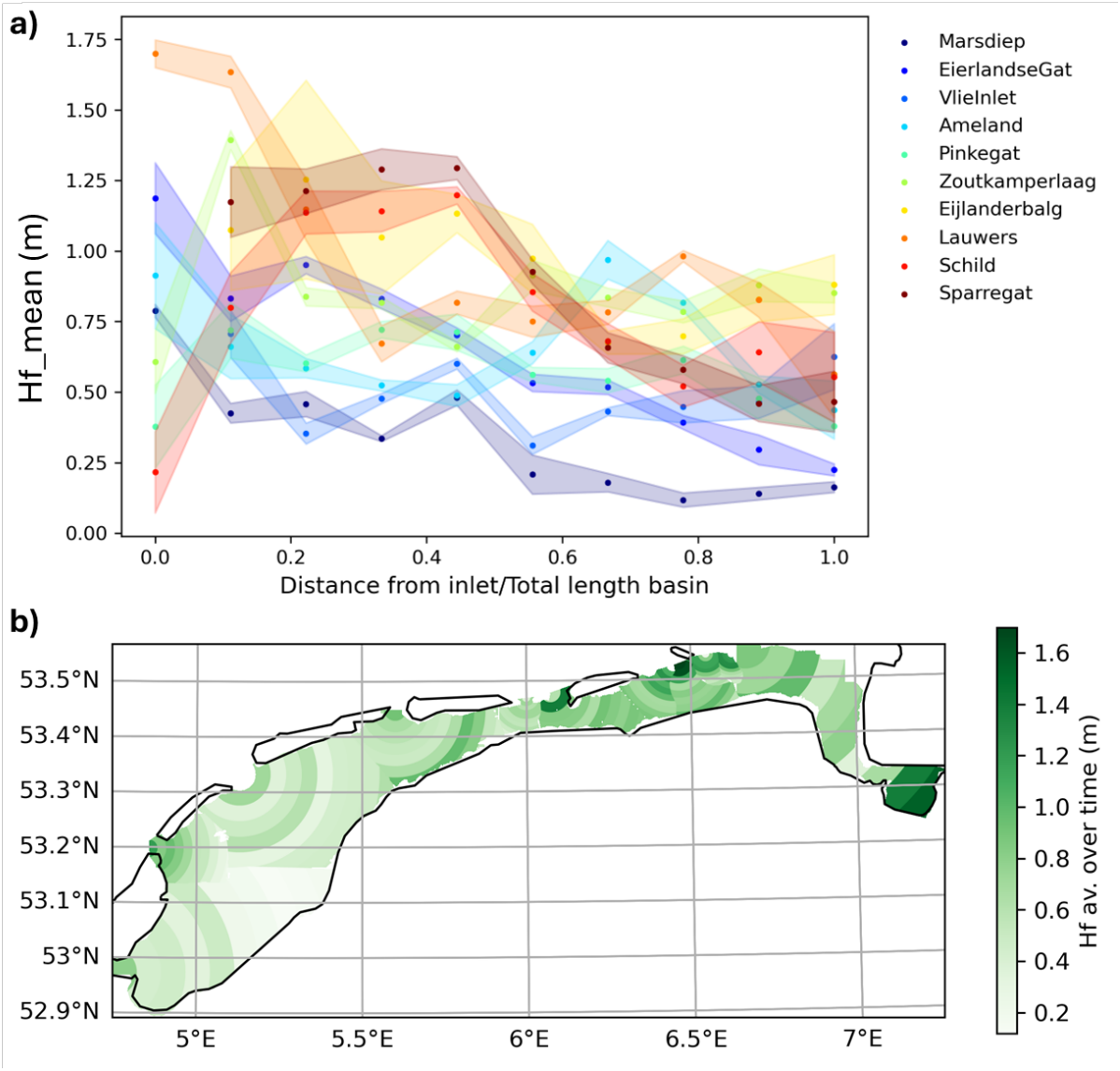

Figure 3.18: Spatial trends in mean height of intertidal flats with distance from the inlet within the tidal basins. Temporally averaged for 1985-2022, shaded regions indicate standard deviations in time.

3.5. Scale-dependency tidal basin morphology

A similar pattern in relative flat area is present for small tidal basins and the landward part of larger tidal basins, with exclusion of the Marsdiep and Vlie basins (Fig. 3.19(b)). In this approach, it is assumed that the landward part of large basins can be considered as a collection of small tidal basins in itself. Based on this assumption, the distance to inlet is a proxy for decreasing basin size. Therefore, a comparison with the full-basin scale can be made.

For all plots in Figure 3.19 and 3.20, the range of values in time is large for the first

data points. These first values are based on the most landward rings, which sometimes contain only very small portions of the basins that do not show a representative morphology. For comparing these patterns, the parts with lower spread are more reliable.

Comparison of the intertidal flat area shows a similar relation between relative flat area and basin size for full-basins and distance from the landward boundary.

The relation between basin size of entire basins and relative flat area is (Fig. 3.19(a)):

$$A_f / A_b = 128.34 * Ab^{-0.15} \tag{3.3}$$

With annular increasing basin size the downward trend in *Af/Ab* is (Fig. 3.19(b)):

$$A_f / A_b = 96.65 * D_{land}^{-0.13} \tag{3.4}$$

The mean flat height shows different patterns in each basin (Fig. 3.19(e,f)), which results in different patterns of relative flat volume between small basins and (the landward part of) large basins (Fig. 3.19(c,d)). Again the Marsdiep deviates strongly from the other basins.

In curve shape pattern, the Marsdiep, Eierlandse Gat, Pinkegat, Zoutkamperlaag, and Eijlanderbalg basin are lining up for the largest part (Fig. 3.20), but there is more variation and the pattern is different for the other basins. The Vlie and Ameland basin show higher convexity for the landward part of the basin, lining up with the Schild basin. The Lauwers and Sparregat basins show distinct patterns in convexity and do not coincide with other basins.

Correlation of the tidal prism (TP) and basin area (Ab) for the full tidal basins and annular decreasing sub-sections results in a similar relation (Fig. 3.21):

$$TP = 1.73 * Ab^{0.99 \text{ or } 1.00} \tag{3.5}$$

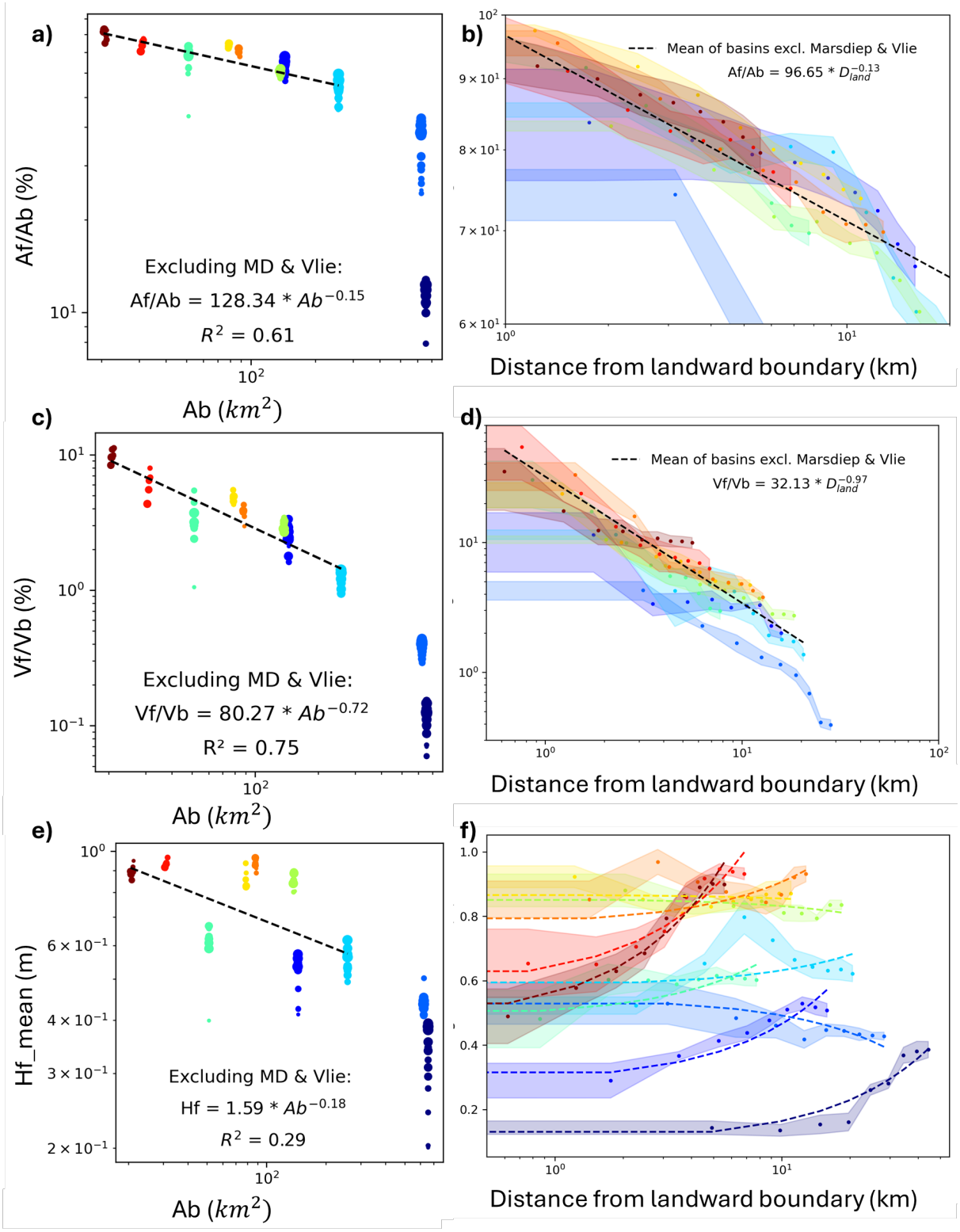

Figure 3.19: Relative area, volume and mean height as a function of basin size for the full-basins (a,c,e) and as a function of distance from the landward boundary for the annular decreasing basin sections (b,d,f). Temporally averaged for 1985-2022, shaded regions indicate standard deviations in time. Full plots for (c) and (d) can be found in Appendix A.8.

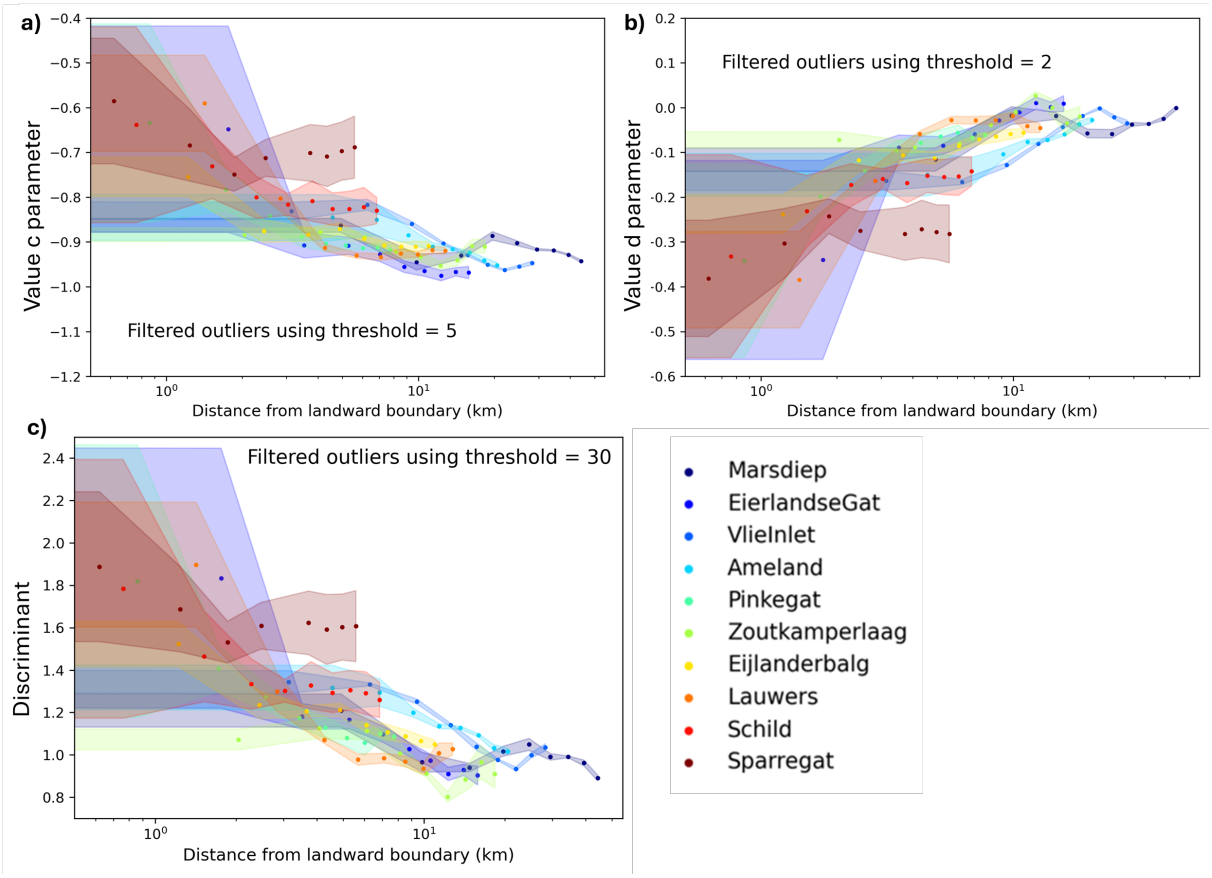

Figure 3.20: Spatial trends in *c* parameter (a), *d* parameter (b) and discriminant (c) of the four-parameter rational curve for annular decreasing basin sections. Temporally averaged for 1985-2022, shaded regions indicate standard deviations in time.

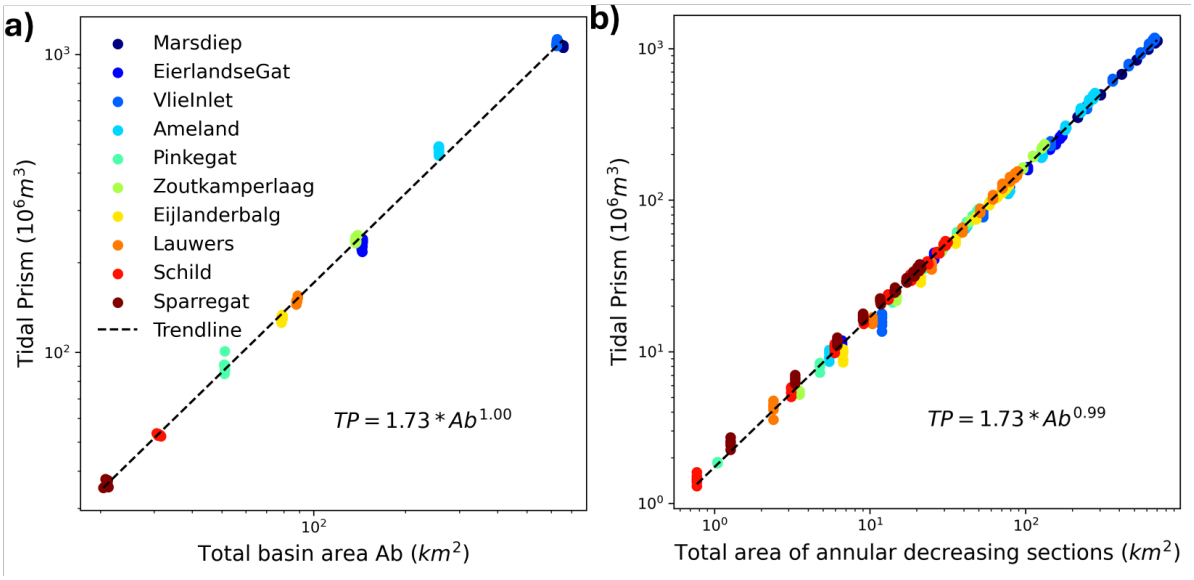

Figure 3.21: Correlation tidal prism and basin size for full tidal basins (a) and annular decreasing basin sections (b).

3.6. Temporal patterns in hypsometry Ems-Dollard estuary

The hypsometry of the Ems-Dollard estuary can be parameterised with the simplified curve as in Equation A.7, containing only the a and b parameter (Fig. A.55). The convexity increases in the intertidal zone, as indicated by the slight decrease in the a parameter, but the overall convexity of the curve decreases, as indicated by the decreasing trend in the discriminant. The increase in convexity in the intertidal zone aligns with the increase in relative area and volume of intertidal flats (Fig. 3.22). The decrease in overall convexity can also be seen from Figure A.28, as the curve is becoming less convex in the subtidal zone.

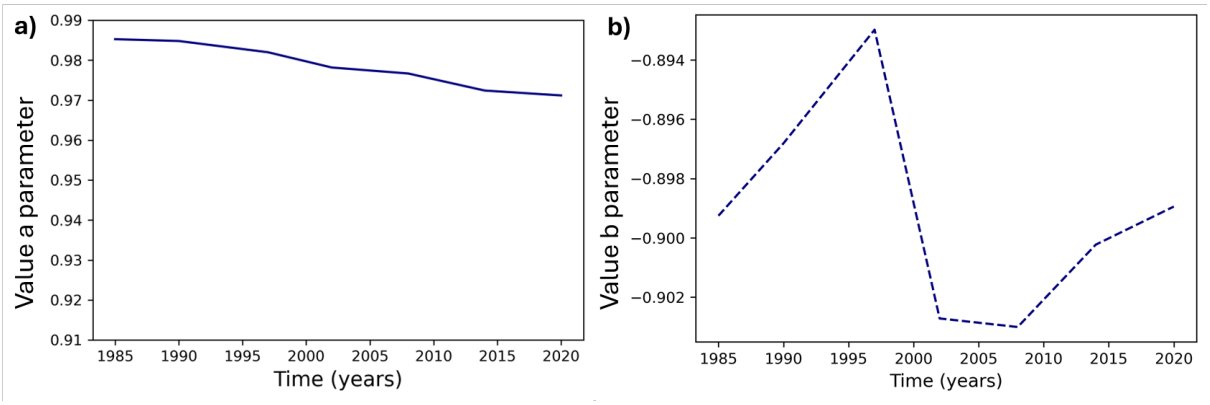

Figure 3.22: Temporal trends of a and b parameter for the simplified rational curve for the Ems-Dollard estuary (Eq. A.7).

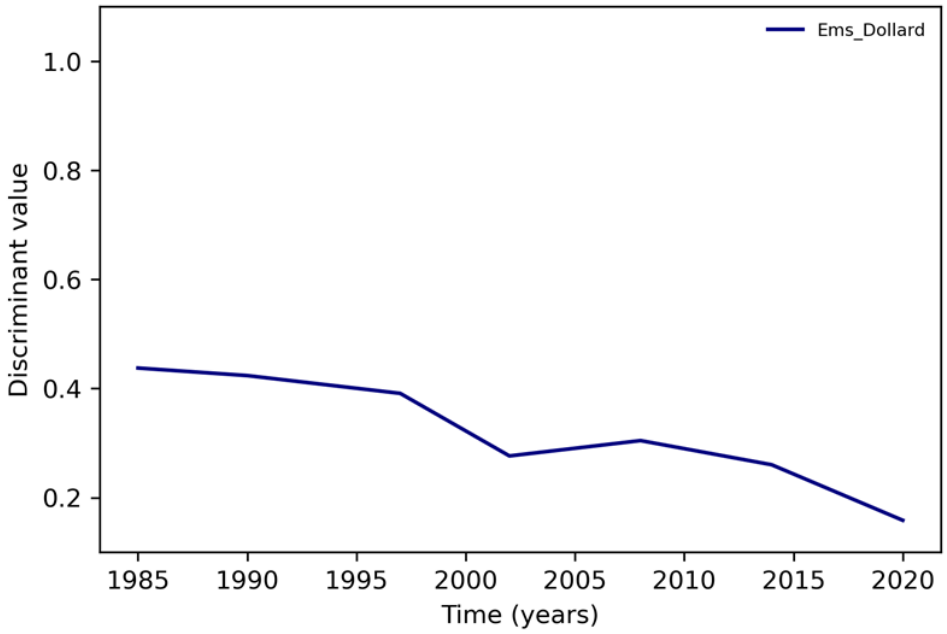

Figure 3.23: Temporal decrease of the discriminant (convexity) of the denominator in the four-parameter rational curve for the Ems-Dollard estuary.

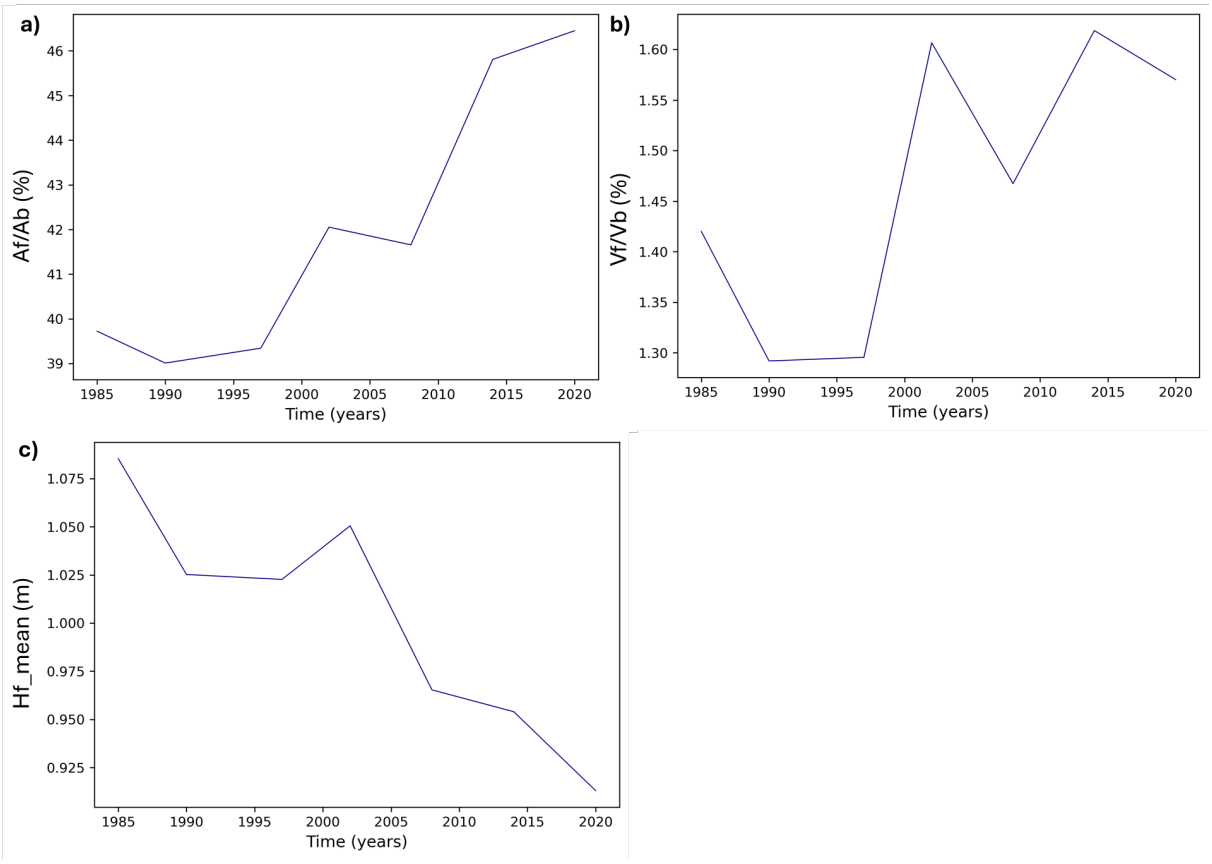

Figure 3.24: Temporal trends in relative flat area (a), relative flat volume (b) and mean flat height (c) for the Ems-Dollard estuary.

3.7. Spatial patterns in hypsometry within the Ems-Dollard estuary

No clear trend with distance from the inlet is visible in the Ems-Dollard estuary in convexity (Fig. 3.25). Instead, the fitting parameters and discriminant show varying behaviour. At D/L 0.1-0.2 & 0.7, the discriminant is negative, indicating concavity. At 0.7 D/L the relative area, volume and mean height of the intertidal flats are also low, aligning with the concave curve shape (Fig. 3.26). At 0.1-0.2 D/L however, the relative area and volume of flats is high, in contrast with the concavity of the curve shape indicated by the discriminant.

Overall, the behaviour of *Af/Ab, Vf/Vb & Hf* follow the same pattern for the Ems-Dollard estuary (Fig. 3.26), indicating higher intertidal flats with a higher ratio of intertidal area.

The result of fitting the (inverse) Strahler curve to the annular sub-sections of the Ems-Dollard estuary show that a somewhat comparable pattern to the c and d parameter (Fig. 3.25) in the z parameter is visible (see Appendix A.9). The fitted versus

measured values in A.62(d,e,f) show large scatter up to a factor of ten, indicating that in this approach the (inverse) Strahler curve is not able to approximate the intertidal flats accurately.

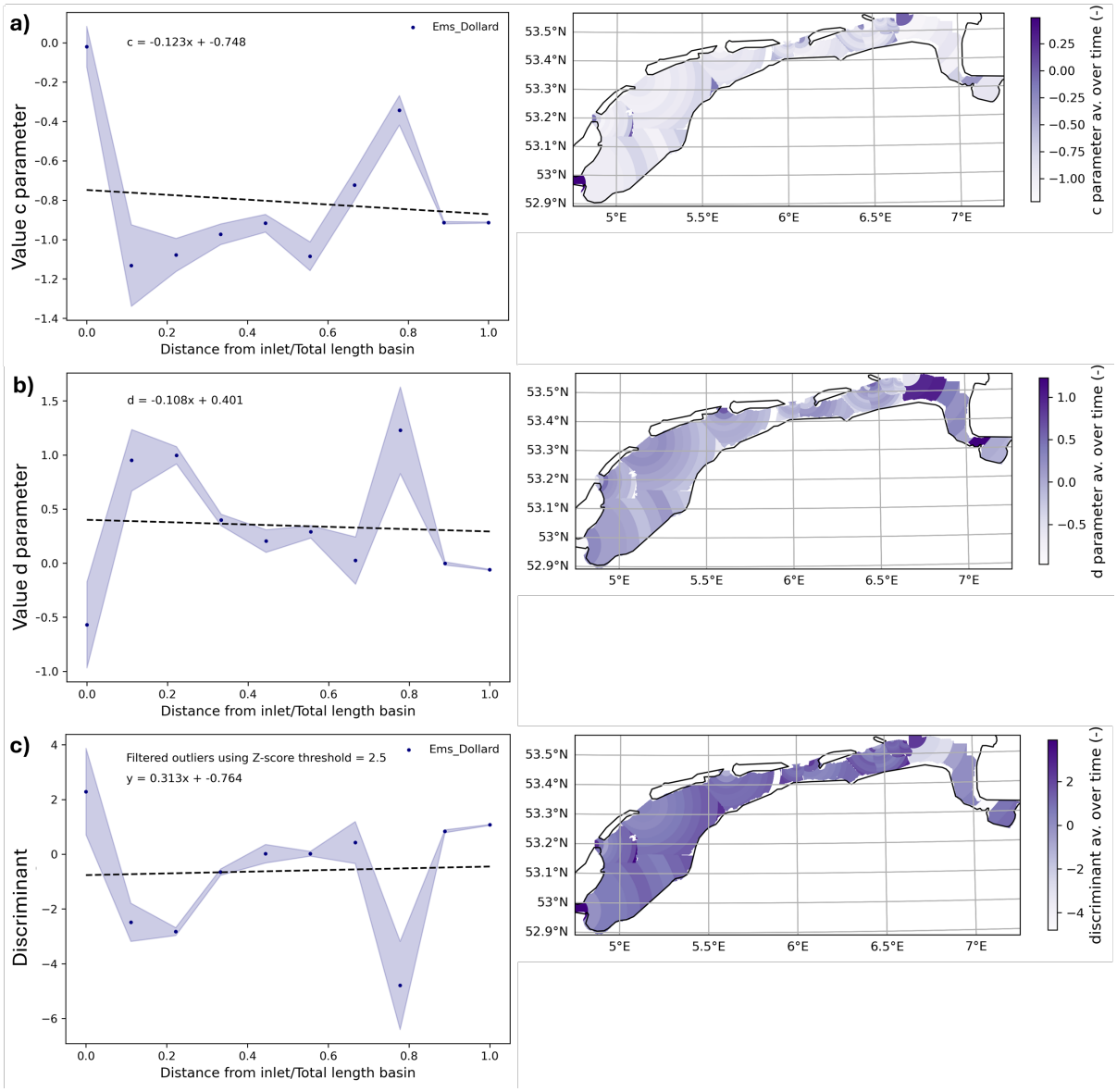

Figure 3.25: Spatial trends in concavity-convexity distance from the inlet for the Ems-Dollard estuary. Trends in *c* parameter (a), *d* parameter (b), and discriminant (c) of the four-parameter rational curve. Temporally averaged for 1985-2022, shaded regions indicate standard deviations in time.

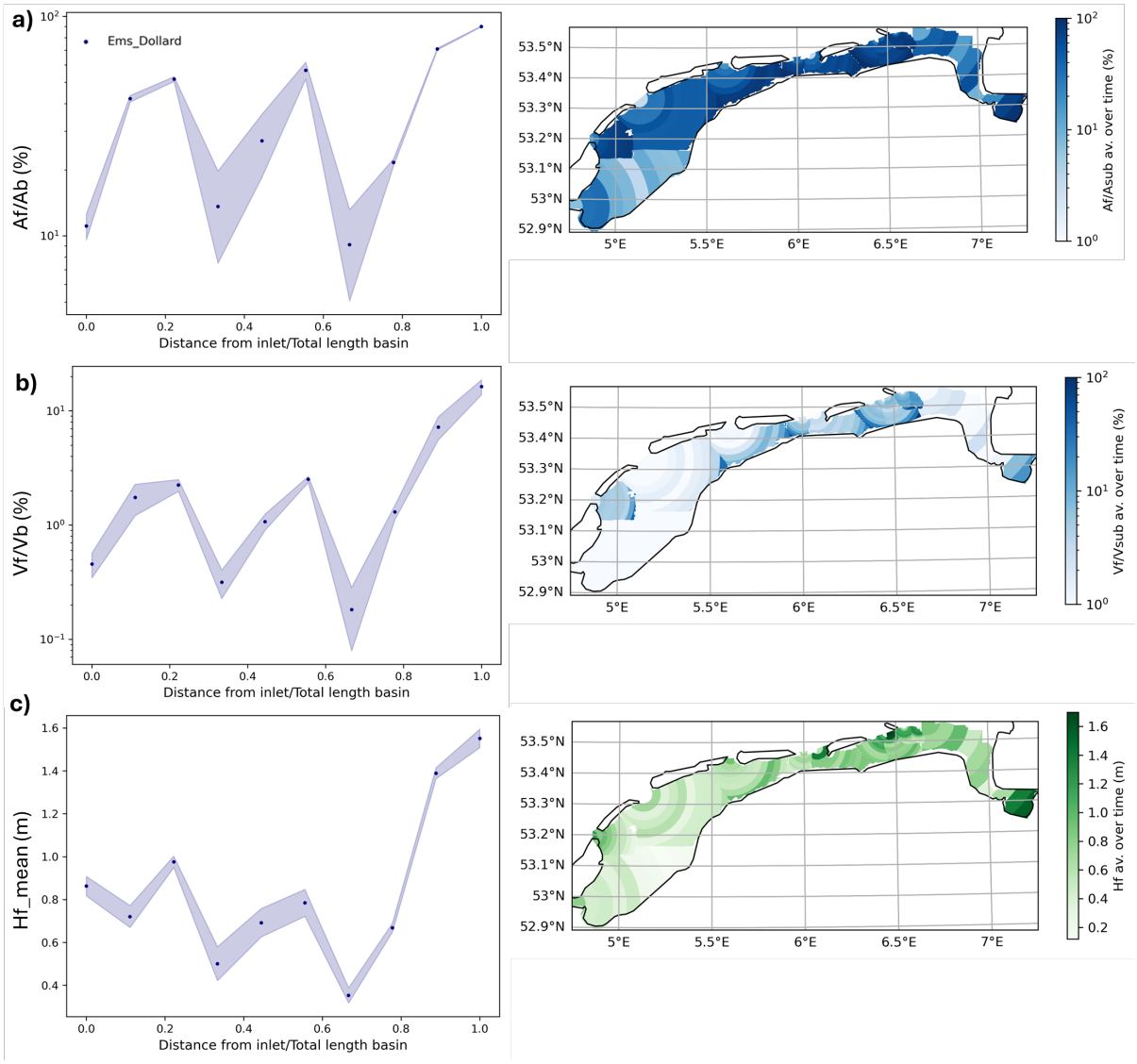

Figure 3.26: Spatial trends with distance from the inlet in relative flat area (a), relative flat volume (b) and mean height (c) for the Ems-Dollard estuary. Temporally averaged for 1985-2022, shaded regions indicate standard deviations in time.

4. Discussion

4.1. Hypsometric characterization in the Dutch Wadden Sea

From fitting a number of hypsometric definitions it is clear that a four-parameter rational curve, as used by Sarkar and Patel (2011), fits the data best. Although the (inverse) Strahler curve as used in Leuven et al. (2018) is capable of producing low RMSE values, it does not accurately represent the intertidal flats that are relevant as habitats and intertidal area.

The high variability in tidal basin hypsometry necessitates a theoretical fitting curve with high flexibility, especially at the head and toe of the curves (Willgoose & Hancock, 1998). Research conducted by Renger and Partenscky (1974) shows the dependence of hypsometry in tidal basins on scale and tidal range. Furthermore, wind-driven currents and anthropogenic influences add complexity to the hypsometry of the Dutch Wadden Sea tidal basins. Despite this complexity, the rational curve in the shape of equation 1.5 can approximate intertidal flats with low RMSE values for the range of variation found in hypsometry for full-basins as well as sub-sections of the tidal basins in the Dutch Wadden Sea.

Simplification of the rational curve based on the correlation of parameters for the full-basin scale shows that fitting with a two-parameter rational curve is possible. The correlations used for this simplification also show that the Ems-Dollard estuary and tidal basins exhibit distinctly different hypsometric shapes and the fitting based on two-parameters cannot be generalized between these two morphological units. The forming processes and scales are different (Willgoose & Hancock, 1998), which is reflected in the different curve shapes and correlations of the parameters of the rational curve. Furthermore, when fitting the rational curve to sub-sections of the basins, the correlations vary for each approach. This suggests that the complexity of hypsometry requires the use of the four-parameter rational curve to produce comparable and generalized results for analysis of sub-sections of the tidal basins. Simplification by reducing the information to the trends in the discriminant, c, and d parameters of the four-parameter rational curve can be used to define concavity-convexity in full-basin and sub-section approaches.

The approximation of intertidal flats from all fitting curves, including the rational curve is worst for the Marsdiep and Vlie basins, which stems from the lower presence of intertidal flats. This indicates that the rational curve model assumption is less suitable for basins with few intertidal flats. The Marsdiep and Vlie basin experience the largest influence of the closure of the Afsluitdijk (Elias et al., 2012), causing them to exhibit a different morphology than the other basins. The more recent grids show better fitting results with a factor lower than two for fit over measured *Af* and *Vf*, indicating that the basins approach a hypsometry more similar to the curve shapes that the rational curve is able to describe.

4.1.1. Influence of grid resolution on hypsometry

Hypsometries of small basins (Eierlandse Gat, Pinkegat, Lauwers, Schild, and Sparregat) are stronger influenced by grid resolution than larger basins in both curve shape and intertidal flat area. This is expected, as the smaller basins have a higher variability and thus the smoothing effect is stronger. With lower resolutions, the deepest depths and highest elevations are lost. This will have a relatively larger effect on smaller basin hypsometry as the range of elevations is lower for the smaller basins as the channels are shallower. The effect on curve shape shown in this research is a combined effect of the smoothing effect and loosing area at the edges of the grids during down scaling. This area loss magnifies changes in curve shape and error in intertidal flat area. Most likely, the actual influence of only grid resolution on curve shape is smaller than visualized in Figure A.29 when the same area for the hypsometric curve is captured.

4.2. Patterns of hypsometry and intertidal flats in the Dutch Wadden Sea

4.2.1. Spatiotemporal trends between tidal basins

From west to east, we see a general increase in the convexity of the hypsometry, intertidal flat area, height, and volume. These increases are to be expected with eastward increasing tidal range, higher sediment availability, lower wave activity and decreasing basin size (Dieckmann et al., 1987; Kirby, 1992; Wells & Park, 1992; Yu et al., 2012).

The Marsdiep and Eierlandse Gat basins defer from the trend in relative flat area. Furthermore, the Eierlandse Gat also defers in the other flat properties, exhibiting much higher values than expected from the west-east trend. This indicates that rel-

ative flat area cannot directly be related to an increasing tidal range, as also stated in Eysink and Biegel (1992), but is mainly governed by the size of the basin.

Over time, convexity is generally increasing or constant for the hypsometric curves in the Dutch Wadden Sea tidal basins, except the Eierlandse Gat, aligning with findings by Elias et al. (2012) and Wang et al. (2018). The erosional trends in the Eierlandse Gat are likely caused by the hydraulic changes as a result of the closure of the Zuiderzee (Elias et al., 2012), which also continues in the more recent years. This shows that the Eierlandse Gat basin continues to adapt in recent years. The Schild and Sparregat basins also defer from the general trend of increasing convexity, possibly because of increased dynamics due to their proximity to the Ems-Dollard estuary and the small elevation ranges within these basins. Small elevation ranges cause curve shape to be strongly influenced by normalization with different maximum depths in the data from different years. The seemingly sudden strong changes in trends and convexity around 1980 can partly be attributed to the change in resolution for the other basins as well.

Temporal trends in convexity do not always match the temporal trends in tidal flat properties. While a decrease in convexity in the Eierlandse Gat is observed, the properties of the tidal flat stay rather constant and the mean height shows even a small increase. In contrast, while convexity stays rather constant for the Vlie basin, the tidal flats grow in area.

The changes in parameters and the discriminant can generally be related to what is visually happening to the curve shape. While this shows that the parameterisation is suitable to describe the curve shapes, the contrasts with the developments of the intertidal zone show the importance of evaluating changes in specific depth zones for more detailed morphological analysis. For example, in Wang et al. (2018) it is mentioned that sedimentation in the Marsdiep and Vlie basins occurred mainly in the intertidal depth zone, and in the Frisian Inlet this occurred mainly over the subtidal part.

The temporal evolution of convexity does not show distinctly different trends between the western and eastern basins. The main difference that can be observed is in the intertidal flat height, where the basins in the west are generally low and the basins in the east are generally high, through time as well. For the Marsdiep, growth in convexity and tidal flats is expected as a result of adaptation to the closure of the Zuiderzee. Compared to the other tidal basins, the growth in flat properties from 1945-

1980 is stronger, but for the most recent period in the data the flat properties stay rather constant. This slow adaptation is in part due to the limited transport of sediment to the Western Wadden Sea (Wang et al., 2018), but could also mean that the flats are approaching equilibrium fractions. This would mean that a large basin such as the Marsdiep might not grow to exhibit hypsometry and tidal flat morphology similar to the smaller basins in the east, which is often assumed as an equilibrium approximation (Elias et al., 2012).

4.2.2. Spatial differences between the eastern and western halves of the tidal basins

The difference in variability between the basin halves between the western and eastern Wadden Sea shows how physical influences and geological past have a ongoing impact on morphological patterns, which aligns with the description in Wang et al. (2020).

The difference between basin halves is strongest in the eastern Wadden Sea, with overall higher convexity in the eastern halves of the basins. This is in agreement with the expectation of higher sediment availability in the eastern half due to wind-driven currents and eastward increasing tidal range. The contrasting pattern observed in the Sparregat basin can be attributed to the incorporation of sections from the Rottumeroog and Zuiderduintjes. Although hypsometry is cut off at MHW, it is likely that a more elevated intertidal area around these minor barrier islands results in higher convexity. For the Eijlanderbalg the higher convexity in the western half might have to do with the orientation of the tidal inlet, but the analysis in this research is not sufficient to determine what causes this pattern. In mean flat height, it differs which half of the basin is highest and the height pattern of the intertidal flats is not always consistent with earlier observations from satellite data, in which lower flats in the eastern halves of the basins were found due to the distance from the inlet (Wang et al., 2020).

In the western Wadden Sea, the difference in convexity between basin halves is less strong. The subsurface of the western Wadden Sea contains Pleistocene deposits, and the present-day morphology is strongly influenced by the closure of the Afsluitdijk (Wang et al., 2020). Most of the intertidal area in the Marsdiep is located in the southern half (the Balgzand) and, therefore, this half exhibits a higher convexity.

4.2.3. Spatial pattern as a function of distance from the inlet

The convexity and relative amount of intertidal flats increase with distance from the inlet, while the flats are highest near the inlet. Increasing convexity with distance from the inlet can be explained by an increasing tidal range, decreasing wave energy and a decreasing tidal prism resulting in an exponentially decreasing channel volume (Eysink & Biegel, 1992; Eysink, 1993; Cleveringa & Oost, 1999). Close to the inlet, flow velocities are high, limiting the extent of the intertidal flats, but strong breaking sea waves are able to build up high tidal flats (Eysink & Biegel, 1992). Further away from the inlet, wave energy dissipates and local wind waves reduce the height of the flats (Eysink & Biegel, 1992).

The deviating patterns in mean flat height in the Schild and Sparregat basin can be explained by the inclusion of parts of Rottumeroog and Zuiderduintjes. In the Ameland basin, the flats bordering the mainland are higher and are included in the annular sub-sections at 0.5-0.7 *D/L*, the increased height of the flats along the coast can be expected due to the embayed shoreline (Friedrichs & Aubrey, 1996). The sudden concavity of the annular sub-section at 0.9 D/L is likely the result of intense dredging close to the Holwerd harbour, as this part of the Ameland basin is included in the sub-section.

4.2.4. Scale-dependency of tidal basin hypsometry and tidal flat morphology

Patterns in relative flat area in small basins show similarity to the outer part of larger tidal basins. Furthermore, the relation between relative flat area and basin size (or distance from landward boundary as proxy for basin size) is similar for full tidal basins and annular decreasing basin sizes. Both show an exponential function with a negative exponent. Specifically, these exponents are -0.15 (full basins) and -0.13 (annular decreasing basin size); with increasing basin size, the relative area of tidal flats decreases. The similarity of this relation in both approaches points to a fundamental similarity and self-organization in underlying processes that govern the relative amount of intertidal flats relative to basin size, which leads to a dominant scale-dependency. One of the governing factors in this is the tidal prism, which shows a consistent linear relationship with absolute basin size for both the full basin and annular decreasing basin section approaches. This is expected as tidal prism is directly related to basin size and cross-sectional area of the inlet (D'Alpaos et al., 2010).

The Marsdiep and Vlie basins deviate strongly from the pattern caused to the disturbance by the Afsluitdijk. Nonetheless, the consistent scale-dependent pattern of relative flat area between and within all other basins suggests that, with sufficient sediment input, they will adjust to fit this relation as well. Assuming this points to an equilibrium relation, this means that the Marsdiep would grow to contain 41.6-48.5% (Eq. 3.3 & 3.4) of tidal flat area under sufficient sediment supply.

In relative volume of flats, the pattern differs per basin, as a result of basin specific patterns in mean flat height. In convexity and fitting parameters, variability between basins and annular decreasing basin sections are visible. This shows that the influences of different physical parameters such as prevailing southwesterly winds, eastward increasing tidal range, differences in inlet geometry and orientation, and anthropogenic influences are incorporated in the full depth hypsometric curve shape.

Despite all these factors influencing morphology in the Dutch Wadden Sea, the pattern in relative flat area continues to show a predominantly scale dependence.

4.2.5. Spatiotemporal patterns of hypsometry in the Ems-Dollard estuary

The observed increase in intertidal flats in the Ems-Dollard estuary supports the continued sedimentation trend that was already observed up until 2022 (Cleveringa, 2008). The decreasing trend in discriminant for the Ems-Dollard estuary results from decreasing convexity in the subtidal zone, but might also partly be the result of the normalization with varying maximum depths.

In the Ems-Dollard estuary, more convex hypsometries, higher relative areas of flats, and higher mean flat heights are present in the broader parts of the estuary, which is in agreement with the research by Leuven et al. (2018) and related to a larger excess width. As mentioned in Section 3.7, the convexity-concavity can be captured by the (inverse) Strahler curve, but fitting with these is not suitable to find accurate approximations of intertidal area and volume for the annular sub-sections. This again shows that when more area is included, more complex forms of hypsometry will occur that can only be described by more flexible curves.

4.3. Further work

This study presents the first parameterization of hypsometry of the tidal basins of the Dutch Wadden Sea. The patterns presented in the fit parameters and intertidal flat characteristics are input into a statistical model with grain size and changes in benthic species composition and abundance.

A predictability of concavity-convexity patterns as in Leuven et al. (2018) is beyond the scope of this study. The patterns of concavity-convexity are consistent with previously defined relationships between concavity-convexity and physical parameters, but further (spatiotemporal) analysis is needed to find a possible predictability to these patterns. For this, the separation of annular sub-sections and basin halves could be combined and further examined.

Detailed variability in tidal range, both spatially and temporally, is not included in this research. In order to accurately relate changes in tidal range to the changes observed in hypsometry, it would be beneficial to determine the pattern of tidal range in more detail.

Temporal analysis of the sub-section approaches is needed to understand how these patterns in hypsometry and intertidal flats respond to rising sea-levels. This will provide insight in the heterogeneity of vulnerability of intertidal flats to rising sea levels between and within different tidal basins. Furthermore, temporal analysis will show if the patterns are growing towards (or away from) equilibrium relations.

For the general implementation of hypsometric characterization, it is important to address two important drawbacks of this method. First of all, when using parameterized comparison of hypsometric curve shape, it is important to use the same area through time. However, in this highly dynamic system, it is preferable to include flexible wan tides as the tidal basins grow and shrink over time. This presents a challenge to the implementation of the parameterization of hypsometry. Secondly, the maximum depth present in the grid influences the curve shape after normalization, this influence is largest for grids with small elevation ranges. Variation in maximum depth is significant when data grids have varying resolutions, because lower resolutions tend to smooth out the deepest and highest elevations.

5. Conclusion

The four-parameter rational curve in the form of Equation 5.1 is most suitable for parameterization of tidal basin hypsometries in the Dutch Wadden Sea. Fitting with this curve results in RMSE values below 0.1 and an accurate representation of the intertidal flats, which are an important focus of this study due to their significance as benthic habitats. Furthermore, with the four-parameter rational curve, complexity in hypsometry of estuaries, tidal basins and sub-sections of these morphological units is possible.

$$\frac{h}{H} = \frac{a + bx}{1 + cx + dx^2} \tag{5.1}$$

The c parameter, d parameter, and discriminant indicate concavity-convexity, reflecting the degree of basin filling. Additional examination of the intertidal depth zone of the hypsometry demonstrated that there can be discrepancies with the concavity-convexity of the curve. Therefore, to get a full picture of changing morphology, it is important to consider specific depth zones in addition to the parameterized curve shape.

The hypsometric curve is sensitive to grid resolution. Small basins with high heterogeneity and smaller elevation ranges show the largest effects. These effects are relevant for areas where spatial resolution varies through time. Parameterization of hypsometry is most reliable for datasets with consistent spatial resolution and consistent temporal elevation ranges.

The Marsdiep and Vlie basins show deviations from the patterns found in hypsometry and intertidal flats, as they are still adapting to the closure of the Zuiderzee.

The results of this study show that changes in the concavity-convexity of hypsometry can be related to changing physical parameters. In general, convexity and presence of tidal flats increase with increasing tidal range, higher sediment availability, lower wave energy and decreasing basin size.

Increasing convexity and proportions of tidal flats are present from west to east and with distance from the inlet. Differences between western and eastern basin halves exist mainly in the eastern Wadden Sea and for the Marsdiep basin. In the eastern halves of the basins, hypsometry is generally more convex, tidal flats are generally higher and exist in larger proportions. The height of the intertidal flats increases eastward,

but decreases with distance from the inlet due to limited sediment import and erosion by local wind waves.

The outer part part of large basins shows a similar pattern in relative flat area as small tidal basins. The relation between annular decreasing basin size and the relative area of flats is similar to the scale-dependent pattern of relative flat area for the full tidal basins; with increasing basin size, the relative area of tidal flats decreases exponentially. The similarity of patterns in relative flat area at different scales argues for a fundamental similarity and self-organization in the underlying processes governing the relative area proportion of tidal flats, resulting in predominantly scale-dependent patterns in the relative area of the intertidal flats. This dependence on scale is further supported by the deviation of the Eierlandse Gat from the west-east trend, which is related to the size of the basin (Eysink & Biegel, 1992; Yu et al., 2012).

Predominant scale-dependency in tidal flat area argues against the interpretation that the Marsdiep and Vlie basins would grow to similar proportions of tidal flat area as the smaller basins to the east under sufficient sediment supply, as is often assumed for equilibrium conditions. This implies that the magnitude of sediment deficits and tidal flat drowning are smaller than under previous assumptions.

References

Bajracharya, P., & Jain, S. (2021). Characterization of drainage basin hypsometry: A generalized approach. *Geomorphology*, *381*, 107645.

Beukema, J. (2002). Expected changes in the benthic fauna of wadden sea tidal flats as a result of sea-level rise or bottom subsidence. *Journal of Sea Research*, *47*(1), 25–39.

Blew, J., & Südbeck, P. E. (2005). Migratory waterbirds in the wadden sea 1980–2000. *Wadden Sea Ecosystem No. 20.*.

Boon III, J. D., & Byrne, R. J. (1981). On basin hyposmetry and the morphodynamic response of coastal inlet systems. *Marine Geology*, *40*(1-2), 27–48.

Borsje, B. W., van Wesenbeeck, B. K., Dekker, F., Paalvast, P., Bouma, T. J., van Katwijk, M. M., & de Vries, M. B. (2011). How ecological engineering can serve in coastal protection. *Ecological Engineering*, *37*(2), 113–122.

Cleveringa, J. (2008). Ontwikkeling sedimentvolume eems-dollard en het groninger wad: Overzicht van de beschikbare kennis en gegevens. *Rapport A2269R1r3, Deltares*.

Cleveringa, J., & Oost, A. P. (1999). The fractal geometry of tidal-channel systems in the dutch wadden sea. *Geologie en Mijnbouw*, *78*(1), 21–30.

D'Alpaos, A., Lanzoni, S., Marani, M., & Rinaldo, A. (2010). On the tidal prism–channel area relations. *Journal of Geophysical Research: Earth Surface*, *115*(F1).

Dask Development Team. (2016). Dask: Library for dynamic task scheduling [Computer software manual]. Retrieved from `http://dask.pydata.org`

Dieckmann, R., Osterthun, M., & Partenscky, H.-W. (1987). Influence of water-level elevation and tidal range on the sedimentation in a german tidal flat area. *Progress in Oceanography*, *18*(1-4), 151–166.

Duran-Matute, M., Gerkema, T., De Boer, G., Nauw, J., & Gräwe, U. (2014). Residual circulation and freshwater transport in the dutch wadden sea: a numerical modelling study. *Ocean Science*, *10*(4), 611–632.

Elias, E., Stive, M., Bonekamp, H., & Cleveringa, J. (2003). Tidal inlet dynamics in response to human intervention. *Coastal engineering journal*, *45*(04), 629–658.

Elias, E., van der Spek, A. J. F., Wang, Z. B., & De Ronde, J. (2012). Morphodynamic development and sediment budget of the dutch wadden sea over the last century. *Netherlands Journal of Geosciences*, *91*(3), 293–310.

Esri. (2023). *ArcGIS Pro.* Retrieved from https://www.esri.com/en-us/arcgis/products/arcgis-pro/overview

Eysink, W. (1993). Isos*2 project: Impact of sea level rise on the morphology of the wadden sea within the scope of its ecological function, phase 4. *Delft Hydraulic report H1300*, 95pp.

Eysink, W., & Biegel, E. (1992). Isos*2 project: Impact of sea level rise on the morphology of the wadden sea within the scope of its ecological function, phase 2: Investigations on empirical morphological relations. *Delft Hydraulic report H1300*, 95pp.

Farber, R. (2011). Chapter 2 - cuda for machine learning and optimization. In *Cuda application design and development* (p. 33-61). Boston: Morgan Kaufmann. doi: https://doi.org/10.1016/B978-0-12-388426-8.00002-1

Friedrichs, C. T., & Aubrey, D. (1996). Uniform bottom shear stress and equilibrium hyposometry of intertidal flats. *Mixing in estuaries and coastal seas*, *50*, 405–429.

GDAL/OGR contributors. (2024). GDAL/OGR geospatial data abstraction software library [Computer software manual]. Retrieved from https://gdal.org doi: 10.5281/zenodo.5884351

Gillies, S. (2019). rasterio documentation. *MapBox, July*, *23*.

GitHub. (2024). rioxarray: Geospatial raster extension for xarray. *GitHub*.

Grasmeijer, B., Jaksic, L., & Vroom, J. (2022). Verkenning morfologische ontwikkeling westelijke waddenzee. *Rapport Deltares*.

Harris, C. R., Millman, K. J., van der Walt, S. J., Gommers, R., Virtanen, P., Cournapeau, D., … Oliphant, T. E. (2020). Array programming with NumPy. *Nature*, *585*, 357–362. doi: 10.1038/s41586-020-2649-2

Hayes, M. O. (1979, 01). Barrier island morphology as a function of tidal and wave regime. *Barrier islands: from the Gulf of St. Lawrence to the Gulf of Mexico*, 1 - 27.

Hayes, M. O., & FitzGerald, D. M. (2013). Origin, evolution, and classification of tidal inlets. *Journal of Coastal Research*(69), 14–33.

Hofstede, J. L. A. (2015, 09). Theoretical considerations on how wadden sea tidal basins may react to accelerated sea level rise. *Zeitschrift für Geomorphologie*, *59*(3), 377-391. doi: 10.1127/zfg/2014/0163

Horton, R. E. (1932). Drainage-basin characteristics. *Transactions, American geophysical union*, *13*(1), 350–361.

Huismans, Y., van der Spek, A., Lodder, Q., Zijlstra, R., Elias, E., & Wang, Z. B. (2022). Development of intertidal flats in the dutch wadden sea in response to a rising sea level: spatial differentiation and sensitivity to the rate of sea level rise. *Ocean & coastal management*, *216*, 105969.

Hunter, J., & Dale, D. (2007). The matplotlib user's guide. *Matplotlib 0.90. 0 user's guide*.

Kirby, R. (1992). Effects of sea-level rise on muddy coastal margins. *Dynamics and exchanges in estuaries and the coastal zone*, *40*, 313–334.

Lesser, G. R., Roelvink, J. v., van Kester, J. T. M., & Stelling, G. (2004). Development and validation of a three-dimensional morphological model. *Coastal engineering*, *51*(8-9), 883–915.

Leuven, J. R., Selaković, S., & Kleinhans, M. G. (2018). Morphology of bar-built estuaries: empirical relation between planform shape and depth distribution. *Earth Surface Dynamics*, *6*(3), 763–778.

Lodder, Q. J., Wang, Z. B., Elias, E., van der Spek, A. J., de Looff, H., & Townend, I. H. (2019). Future response of the wadden sea tidal basins to relative sea-level rise—an aggregated modelling approach. *Water*, *11*(10), 2198.

Louters, T., & Gerritsen, F. (2014). The riddle of the sands; a tidal system's answer to a rising sea level. *Rijkswaterstaat, National Institute for Coastal and Marine Management RIKZ*, *RIKZ-94.404*, 69 pp.

Marciano, R., Wang, Z. B., Hibma, A., de Vriend, H. J., & Defina, A. (2005). Modeling of channel patterns in short tidal basins. *Journal of Geophysical Research: Earth Surface*, *110*(F1).

Marin-Diaz, B., van der Wal, D., Kaptein, L., Martinez-Garcia, P., Lashley, C. H., de Jong, K., ... Bouma, T. J. (2023). Using salt marshes for coastal protection: Effective but hard to get where needed most. *Journal of Applied Ecology*.

McKinney, W., & Team, P. (2015). Pandas-powerful python data analysis toolkit. *Pandas—Powerful Python Data Analysis Toolkit*, *1625*.

Met Office. (2010 - 2015). Cartopy: a cartographic python library with a matplotlib interface [Computer software manual]. Exeter, Devon. Retrieved from `https://scitools.org.uk/cartopy`

Pedregosa, F., Varoquaux, G., Gramfort, A., Michel, V., Thirion, B., Grisel, O., ... Duchesnay, E. (2011). Scikit-learn: Machine learning in Python. *Journal of Machine Learning Research*, *12*, 2825–2830.

Perluka, R., Wiegmann, E., R.W.L., J., & Swart, L. (2006). Opnametechnieken waddenzee. *AGI-Rapport: AGI-2006-GPMP-004*.

Raybaut, P. (2009). Spyder-documentation. *Available online at: pythonhosted. org*.

Renger, E., & Partenscky, H.-W. (1974). Stabilitätsverhalten von watteinzugsgebieten. *Die Küste*, *25*, 73–86.

Sarkar, A., & Patel, P. P. (2011). Topographic analysis of the dulung r. basin. *Indian J Spat Sci II (1)*, *2*.

Stolte, W., Baart, F., Muis, S., Hijma, M., Taal, M., Le Bars, D., & Drijfhout, S. (2023). Zeespiegelmonitor 2022. *Project nr. 11209266 Deltares*.

Strahler, A. N. (1952). Hypsometric (area-altitude) analysis of erosional topography. *Geological society of America bulletin*, *63*(11), 1117–1142.

Temmerman, S., Meire, P., Bouma, T. J., Herman, P. M., Ysebaert, T., & De Vriend, H. J. (2013). Ecosystem-based coastal defence in the face of global change. *Nature*, *504*(7478), 79–83.

Townend, I., Wang, Z. B., Stive, M., & Zhou, Z. (2016a). Development and extension of an aggregated scale model: Part 1–background to asmita. *China Ocean Engineering*, *30*, 483–504.

Townend, I., Wang, Z. B., Stive, M., & Zhou, Z. (2016b). Development and extension of an aggregated scale model: Part 2—extensions to asmita. *China Ocean Engineering*, *30*, 651–670.

van der Spek, A. (1994). *Large-scale evolution of holocene tidal basins in the netherlands* (Ph.D. thesis). Utrecht.

van der Spek, A. J. F. (2018). The development of the tidal basins in the dutch wadden sea until 2100: the impact of accelerated sea-level rise and subsidence on their sediment budget–a synthesis. *Netherlands Journal of Geosciences*, *97*(3), 71–78.

van Prooijen, B. C., & Wang, Z. B. (2013). A 1d model for tides waves and fine sediment in short tidal basins—application to the wadden sea. *Ocean Dynamics*, *63*(11-12), 1233–1248.

Van Rossum, G. (2020). *The python library reference, release 3.8.2*. Python Software Foundation.

Van Rossum, G., & Drake, F. L. (2009). *Python 3 reference manual*. Scotts Valley, CA: CreateSpace.

Virtanen, P., Gommers, R., Oliphant, T. E., Haberland, M., Reddy, T., Cournapeau,

D., ... SciPy 1.0 Contributors (2020). SciPy 1.0: Fundamental Algorithms for Scientific Computing in Python. *Nature Methods*, *17*, 261–272. doi: 10.1038/s41592-019-0686-2

Wahl, T., Haigh, I. D., Dangendorf, S., & Jensen, J. (2013). Inter-annual and long-term mean sea level changes along the north sea coastline. *Journal of Coastal Research*(65), 1987–1992.

Wang, Z. B., Elias, E., van der Spek, A. J., & Lodder, Q. J. (2018). Sediment budget and morphological development of the dutch wadden sea: impact of accelerated sea-level rise and subsidence until 2100. *Netherlands Journal of Geosciences*, *97*(3), 183–214.

Wang, Z. B., Hoekstra, P., Burchard, H., Ridderinkhof, H., De Swart, H., & Stive, M. (2012). Morphodynamics of the wadden sea and its barrier island system. *Ocean & coastal management*, *68*, 39–57.

Wang, Z. B., Huismans, Y., & van der Spek, A. (2020). Morphological development of the tidal inlet systems in the wadden sea. *Project nr. 11203724-012 Deltares, commissioned by Rijkswaterstaat*.

Wang, Z. B., Vroom, J., van Prooijen, B. C., Labeur, R. J., Stive, M. J., & Jansen, M. H. (2011). Development of tidal watersheds in the wadden sea. *River, Coastal and Estuarine Morphodynamics*, *RCEM2011*.

Waskom, M. L. (2021). seaborn: statistical data visualization. *Journal of Open Source Software*, *6*(60), 3021. Retrieved from `https://doi.org/10.21105/joss.03021` doi: 10.21105/joss.03021

Wells, J. T., & Park, Y.-A. (1992). Observations on shelf and subtidal channel flow: Implications of sediment dispersal seaward of the keum river estuary, korea. *Estuarine, Coastal and Shelf Science*, *34*(4), 365–379.

Wiegman, N., Perluka, R., Oude Elberink, S., & Vogelzang, J. (2005). Vaklodingen: de inwintechnieken en hun combinaties. vergelijking tussen verschillende inwintechnieken en de combinaties ervan. *AGI-Rapport: AGI-2005-GSMH-012*.

Willgoose, G., & Hancock, G. (1998). Revisiting the hypsometric curve as an indicator of form and process in transport-limited catchment. *Earth Surface Processes and Landforms: The Journal of the British Geomorphological Group*, *23*(7), 611–623.

Yu, Q., Wang, Y., Flemming, B., & Gao, S. (2012). Modelling the equilibrium hypsometry of back-barrier tidal flats in the german wadden sea (southern north sea).

Continental Shelf Research, 49, 90–99.

A. Appendix

A.1. Study areas for hypsometric curves and sub-section creation

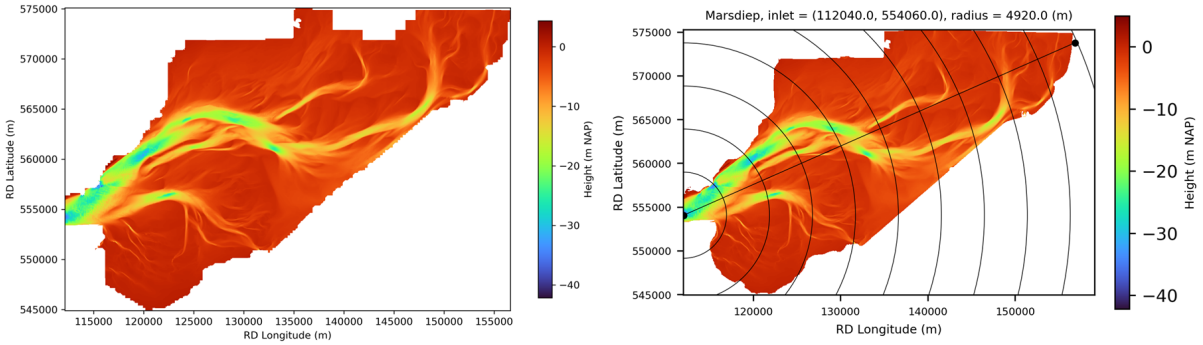

Figure A.1: Marsdiep entire tidal basin (2021 grid) & sub-section creation.

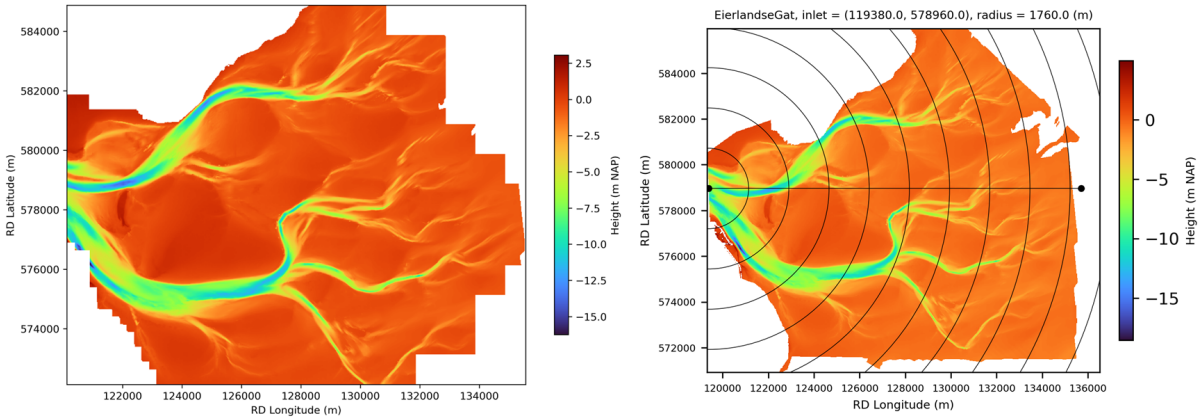

Figure A.2: Eierlandse Gat entire tidal basin (2017 grid) & sub-section creation.

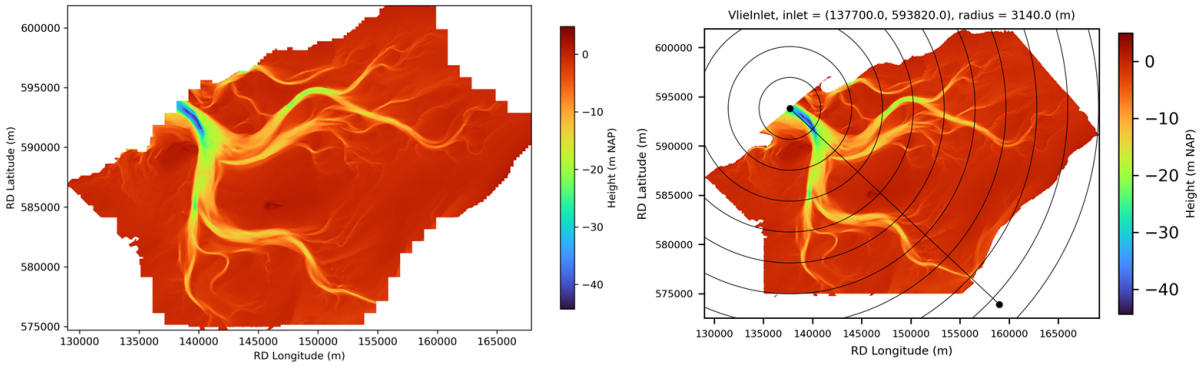

Figure A.3: Vlie Inlet entire tidal basin (2022 grid) & sub-section creation.

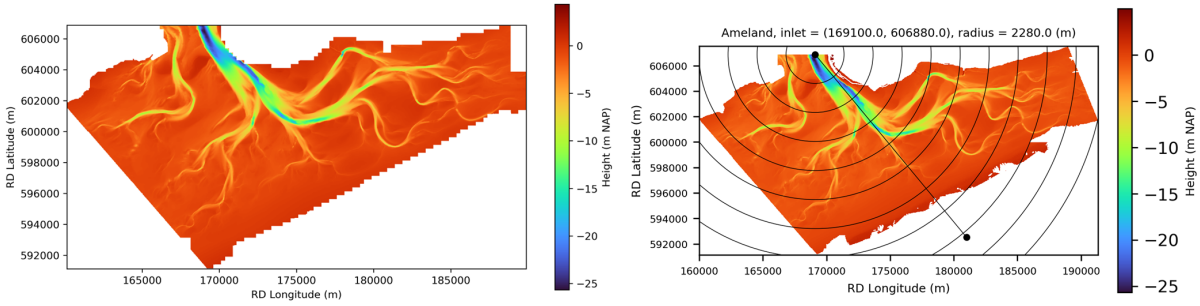

Figure A.4: Ameland entire tidal basin (2017 grid) & sub-section creation.

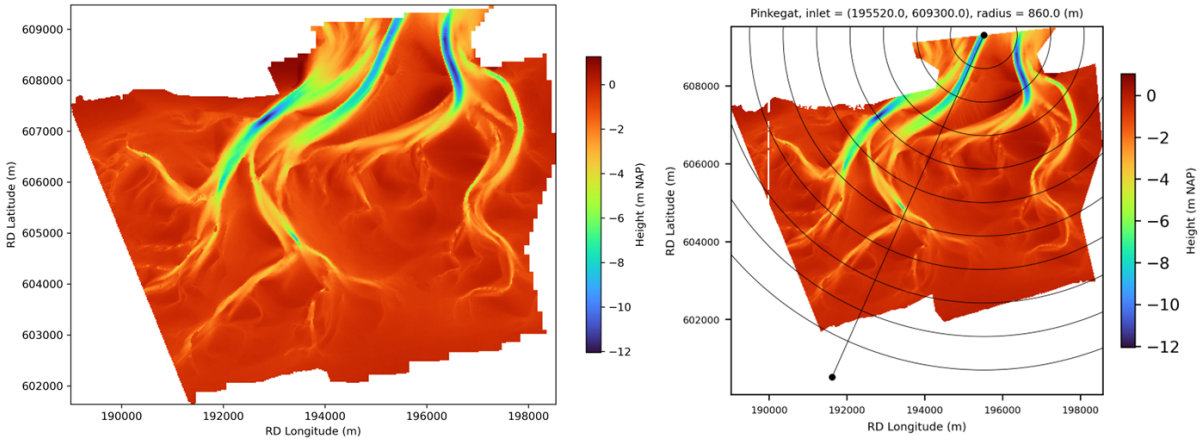

Figure A.5: Pinkegat entire tidal basin (2012 grid) & sub-section creation.

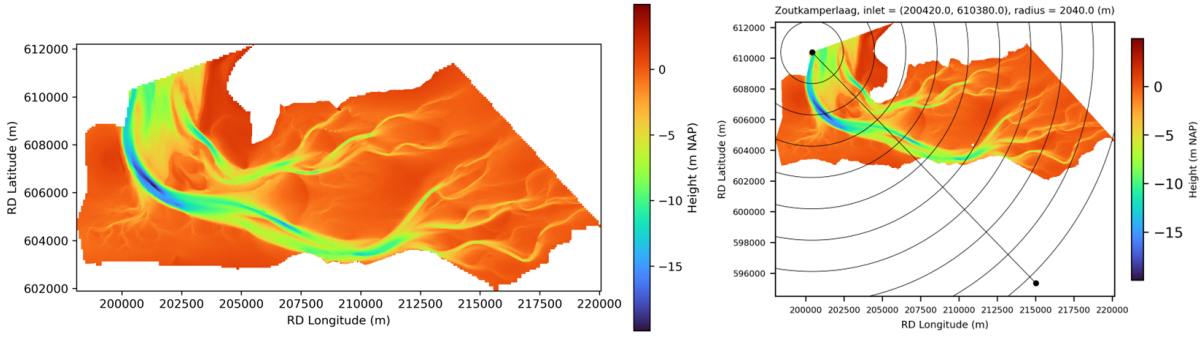

Figure A.6: Zoutkamperlaag entire tidal basin (2012 grid) & sub-section creation.

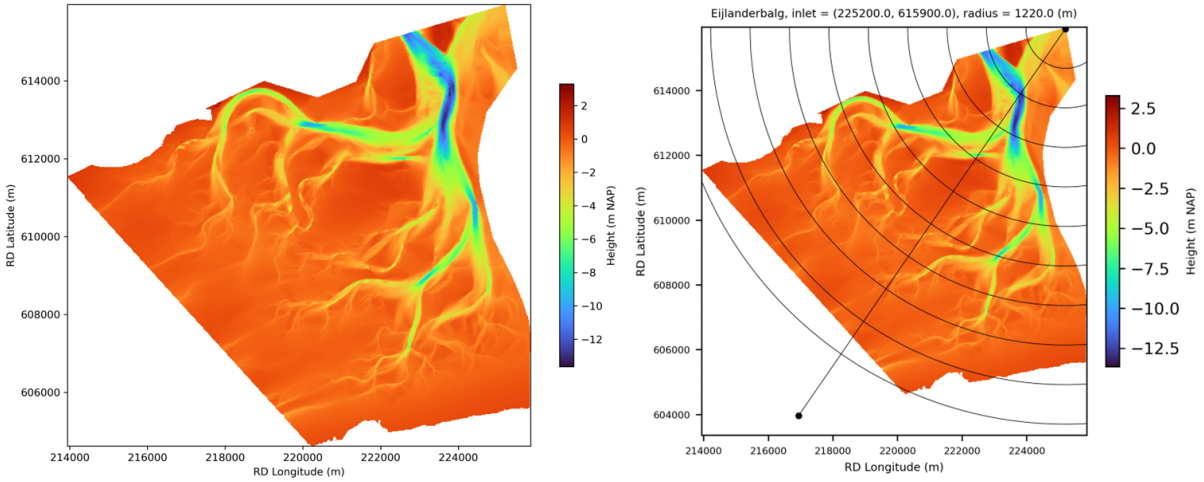

Figure A.7: Eijlanderbalg entire tidal basin (2019 grid) & sub-section creation.

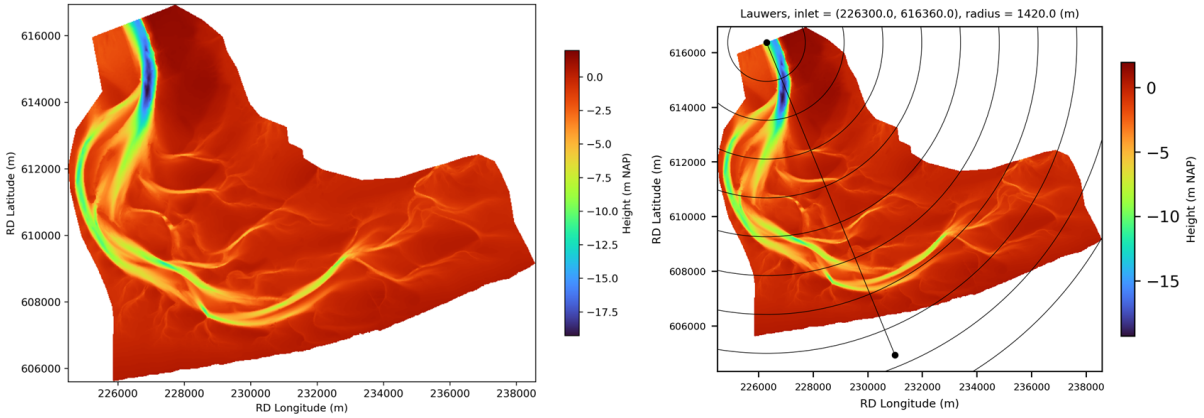

Figure A.8: Lauwers entire tidal basin (2019 grid) & sub-section creation.

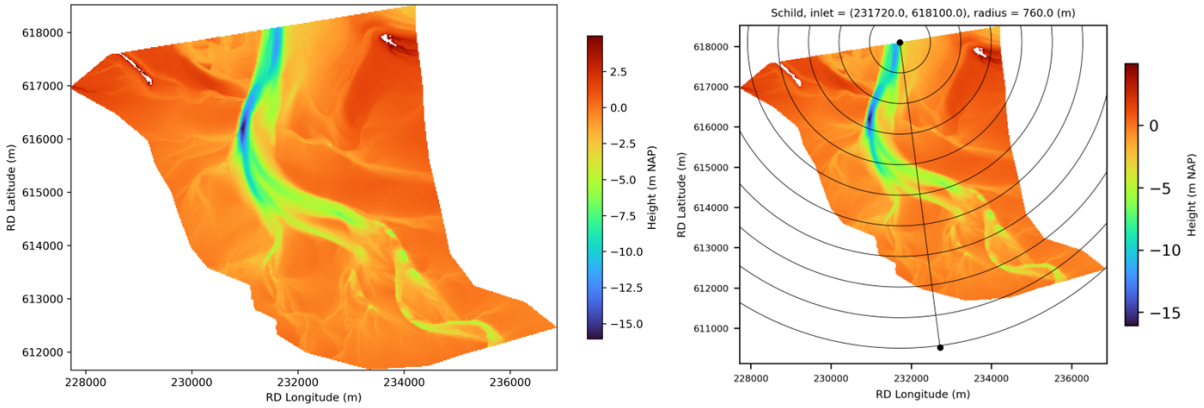

Figure A.9: Schild entire tidal basin (2019 grid) & sub-section creation.

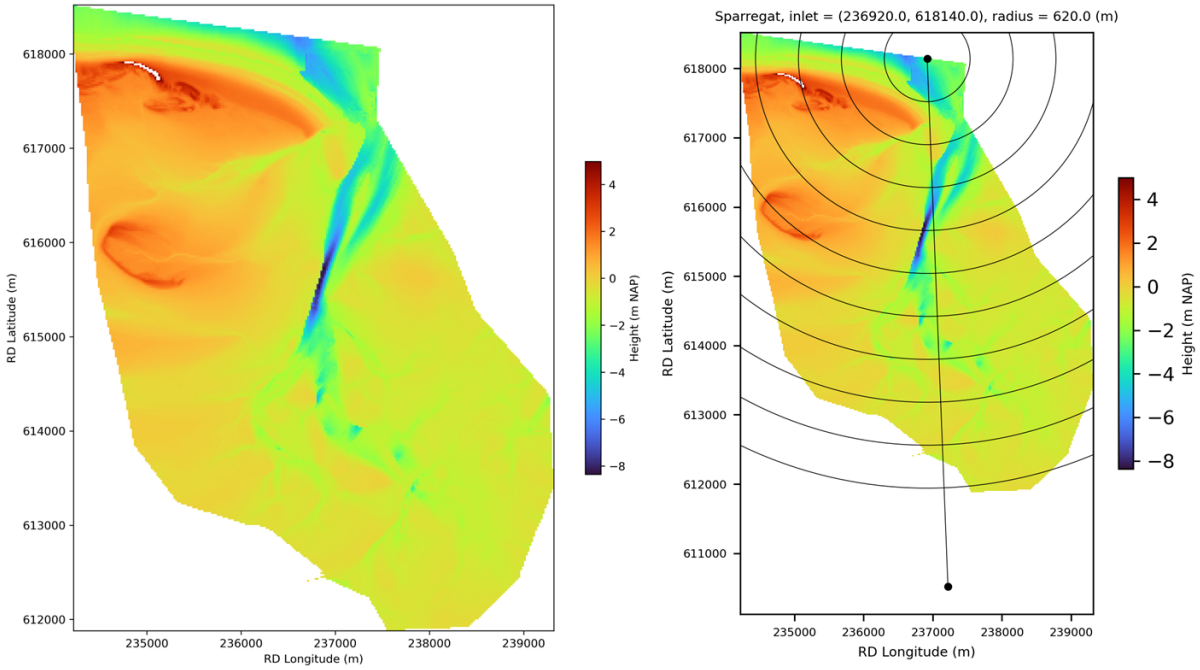

Figure A.10: Sparregat entire tidal basin (2019 grid) & sub-section creation.

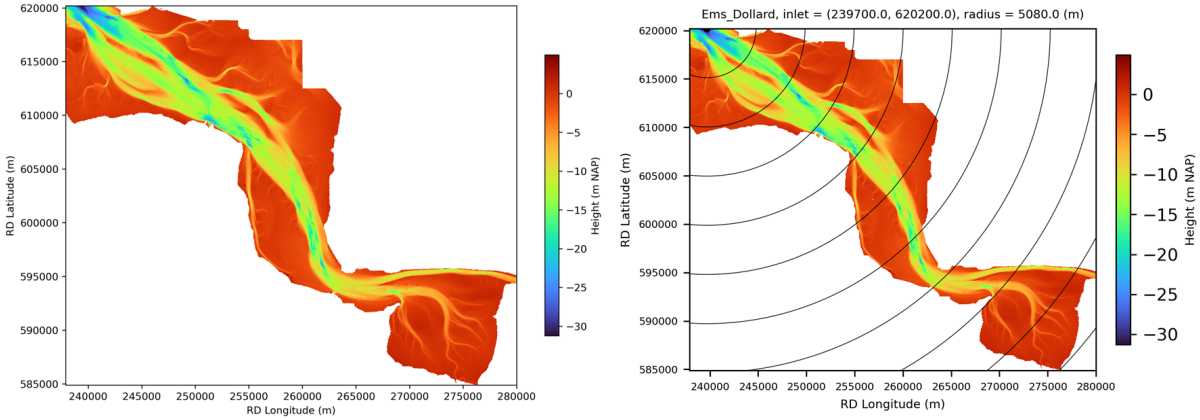

Figure A.11: Ems-Dollard entire estuary (2020 grid) & sub-section creation.

A.2. Hypsometric curves entire basins

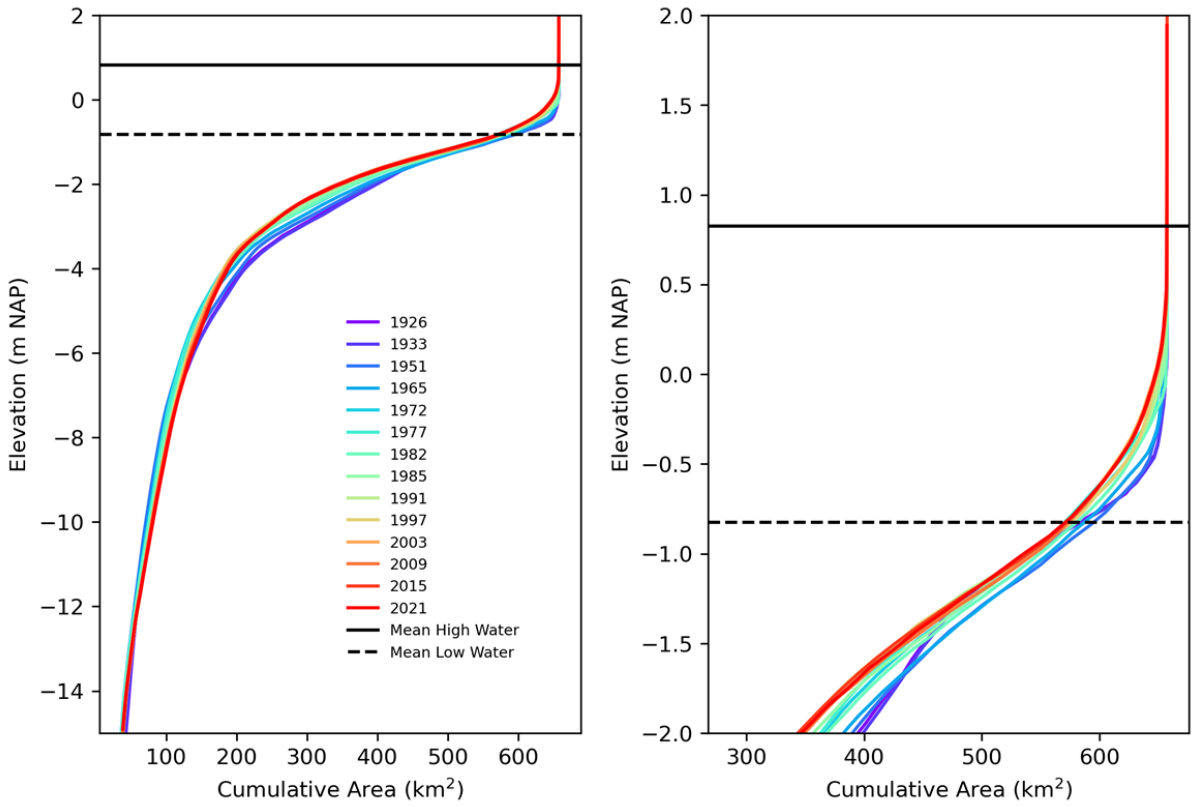

Figure A.12: Area hypsometric curve for the Marsdiep basin between -15m NAP and 2m NAP and between -2m NAP and 2m NAP.

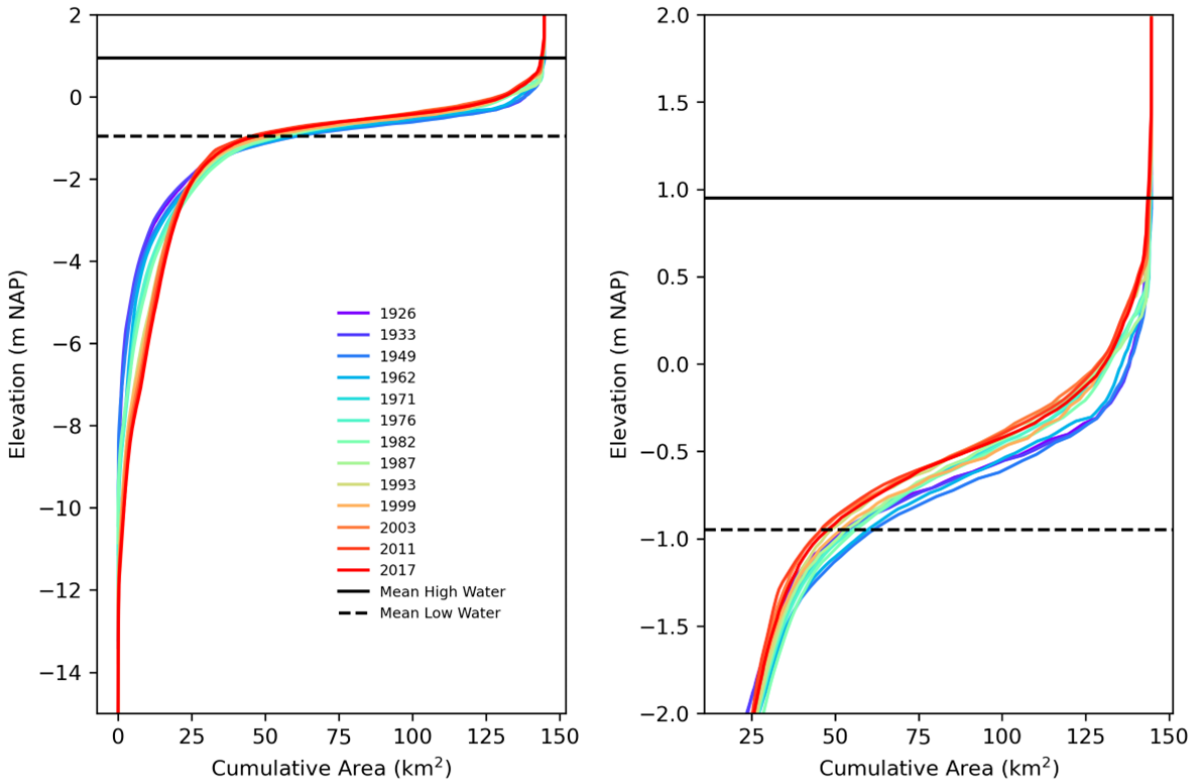

Figure A.13: Area hypsometric curve for the Eierlandse Gat basin between -15m NAP and 2m NAP and between -2m NAP and 2m NAP.

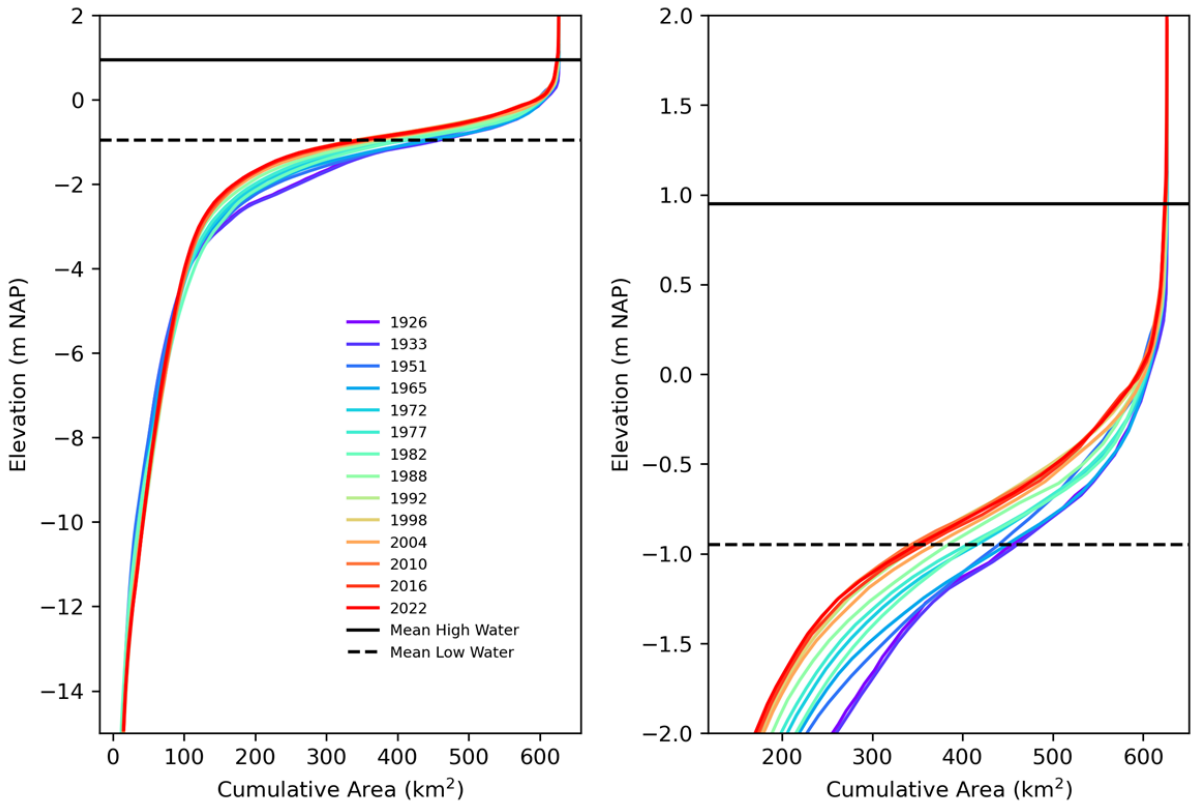

Figure A.14: Area hypsometric curve for the Vlie Inlet basin between -15m NAP and 2m NAP and between -2m NAP and 2m NAP..

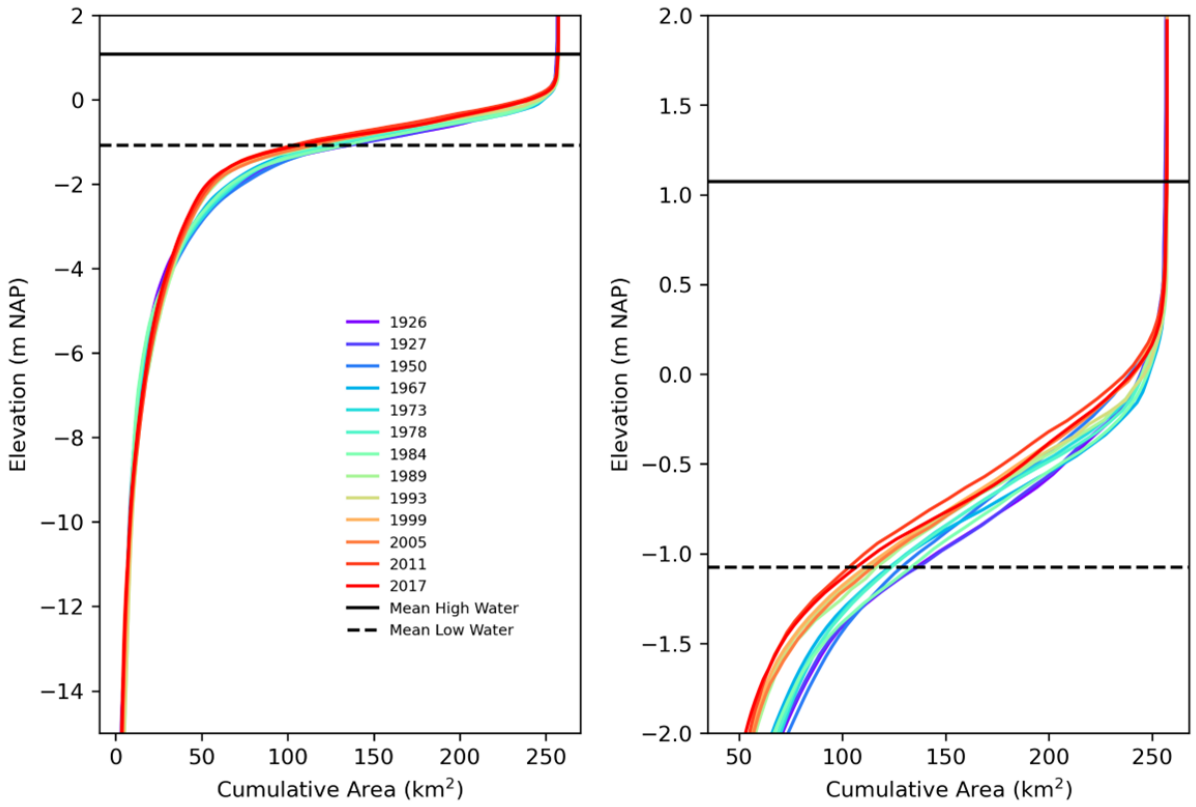

Figure A.15: Area hypsometric curve for the Ameland Inlet basin between -15m NAP and 2m NAP and between -2m NAP and 2m NAP.

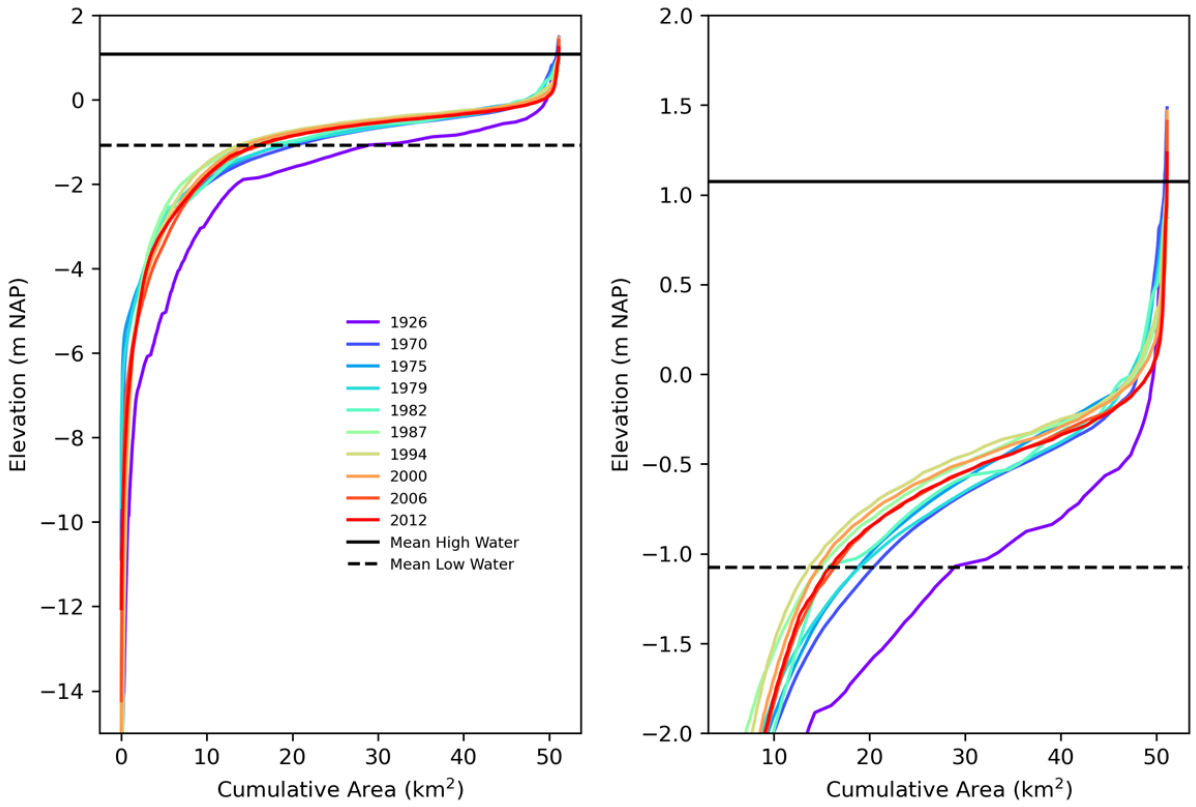

Figure A.16: Area hypsometric curve for the Pinkegat basin between -15m NAP and 2m NAP and between -2m NAP and 2m NAP.

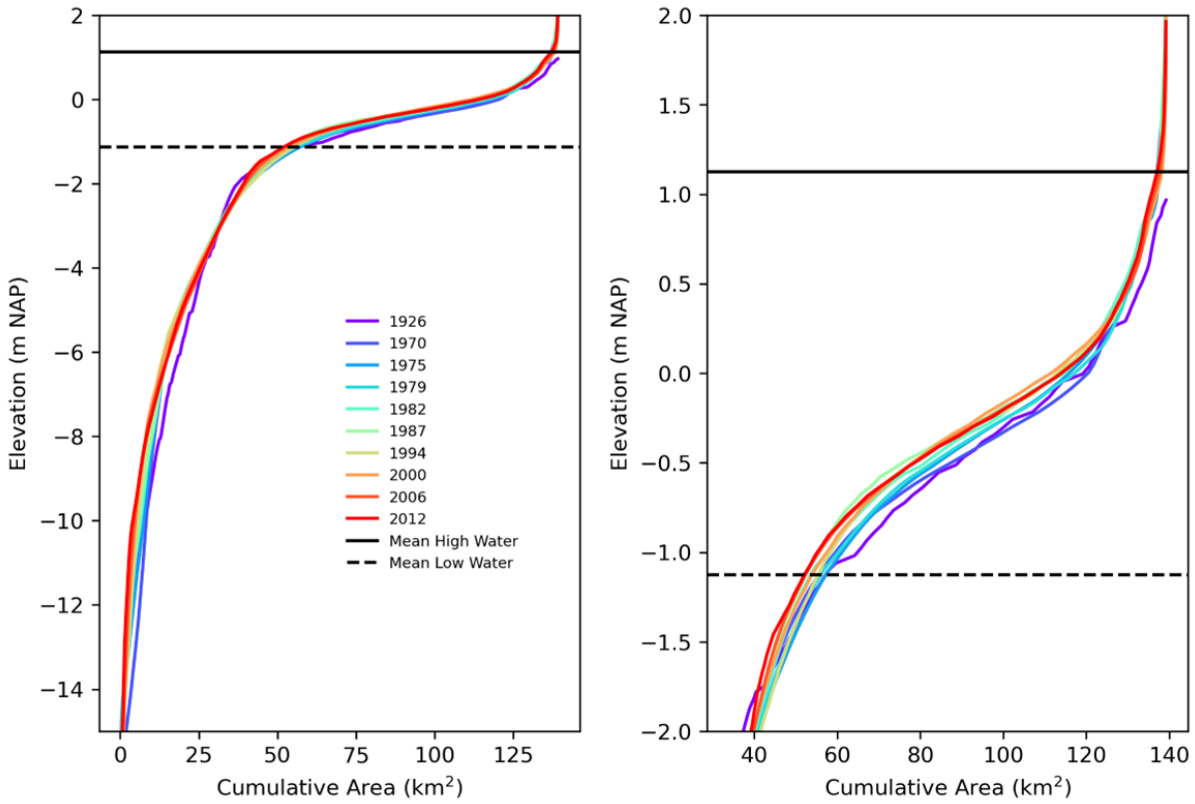

Figure A.17: Area hypsometric curve for the Zoutkamperlaag basin between -15m NAP and 2m NAP and between -2m NAP and 2m NAP.

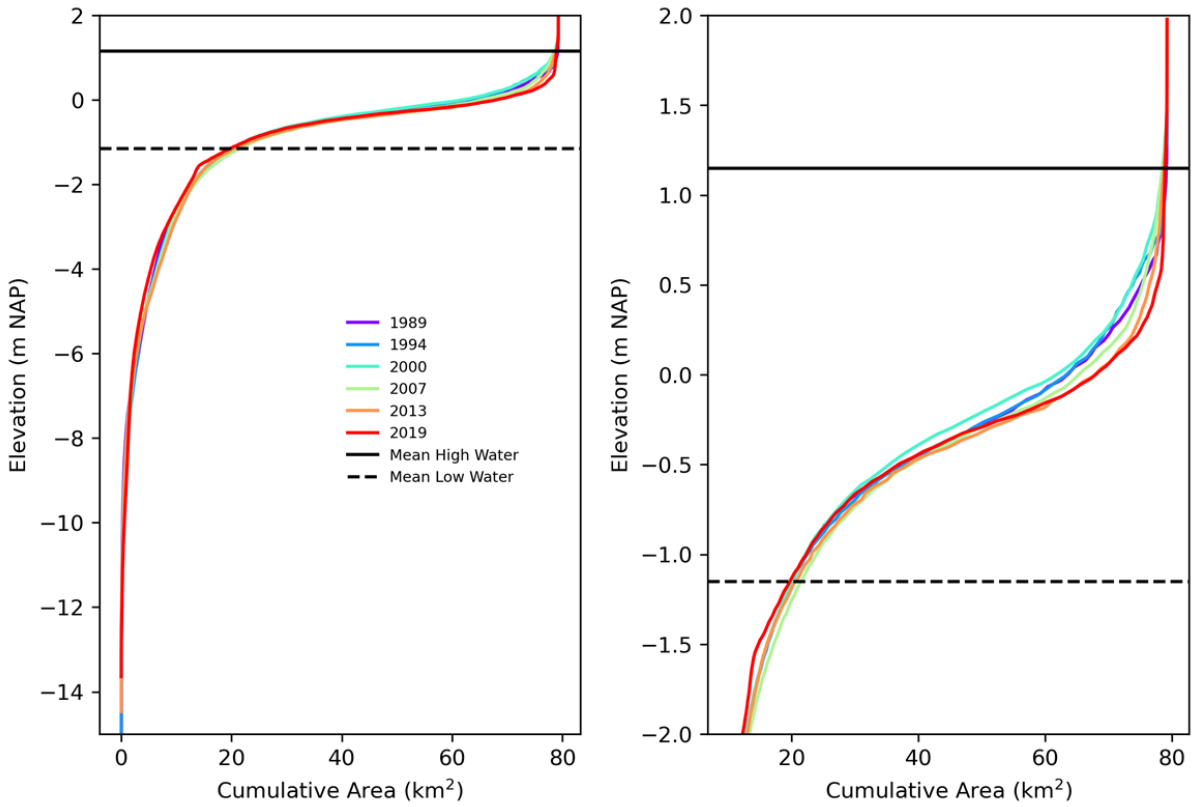

Figure A.18: Area hypsometric curve for the Eijlanderbalg basin between -15m NAP and 2m NAP and between -2m NAP and 2m NAP.

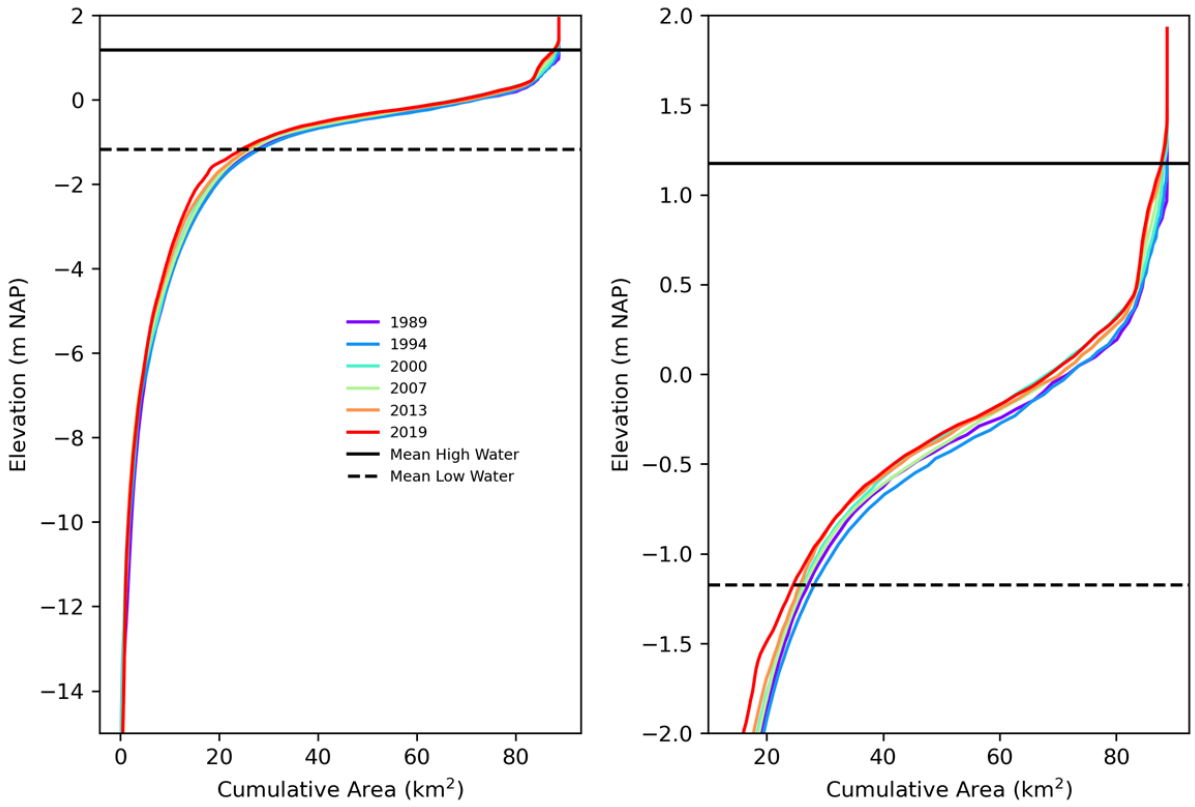

Figure A.19: Area hypsometric curve for the Lauwers basin between -15m NAP and 2m NAP and between -2m NAP and 2m NAP.

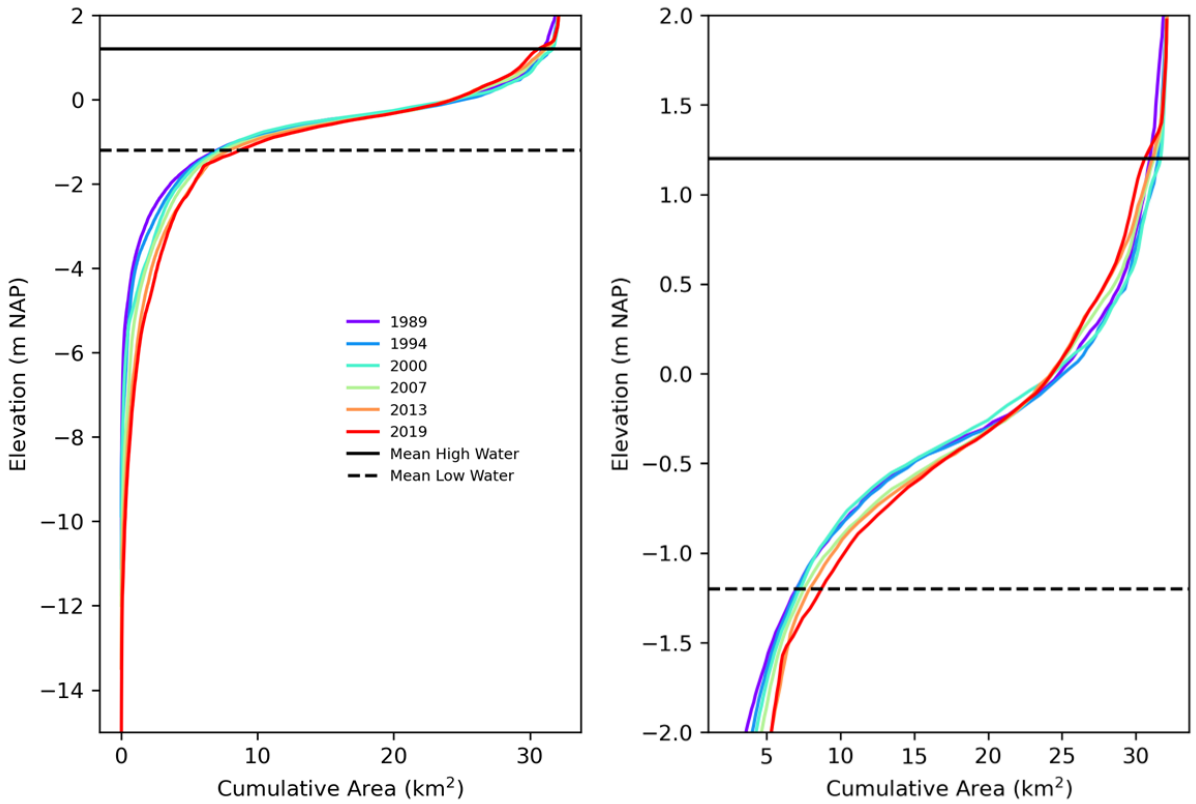

Figure A.20: Area hypsometric curve for the Schild Inlet basin between -15m NAP and 2m NAP and between -2m NAP and 2m NAP.

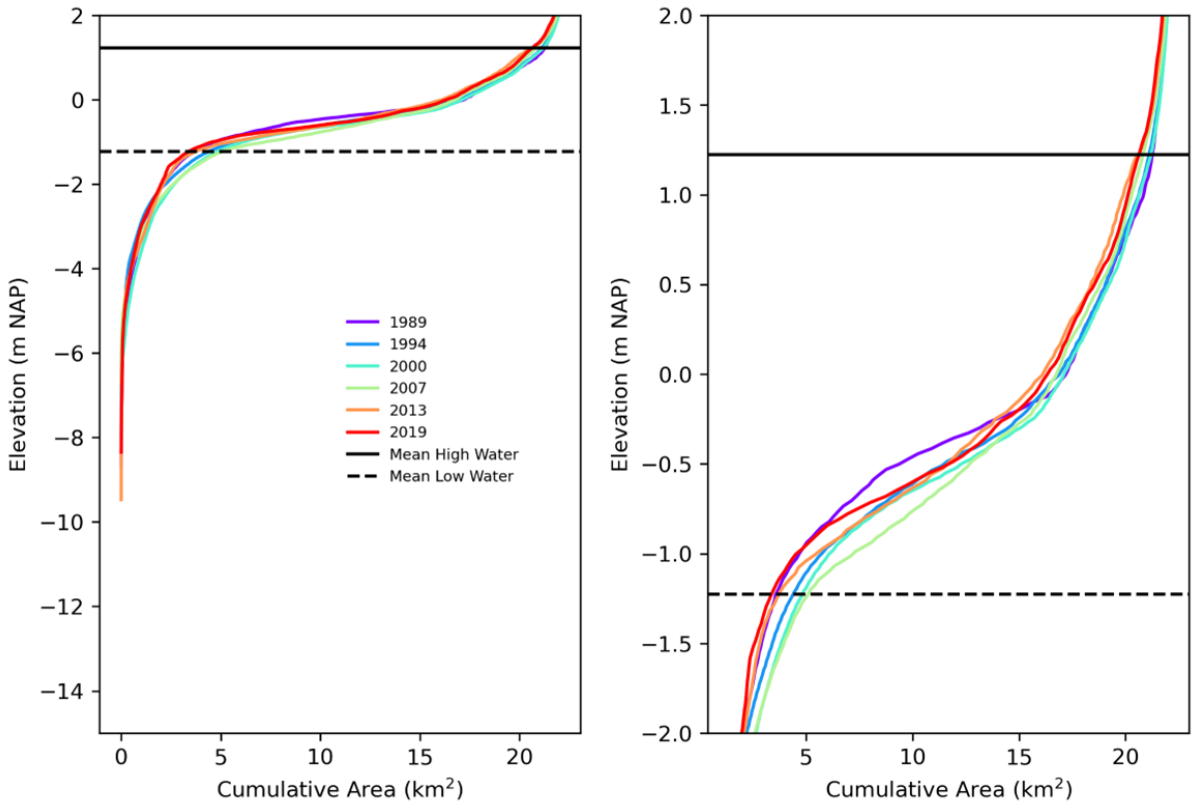

Figure A.21: Area hypsometric curve for the Sparregat basin between -15m NAP and 2m NAP and between -2m NAP and 2m NAP.

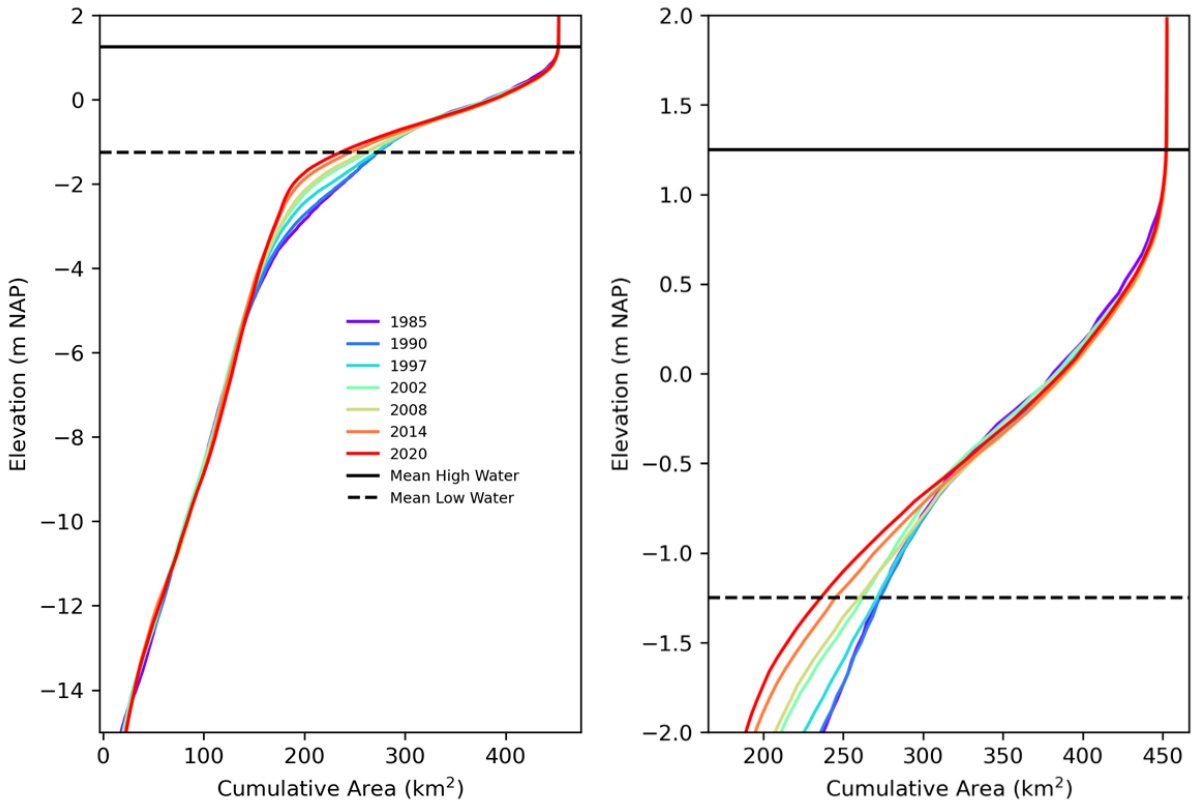

Figure A.22: Area hypsometric curve for the Ems-Dollard Estuary between -15m NAP and 2m NAP and between -2m NAP and 2m NAP.

A.3. Normalized hypsometric curves entire basins

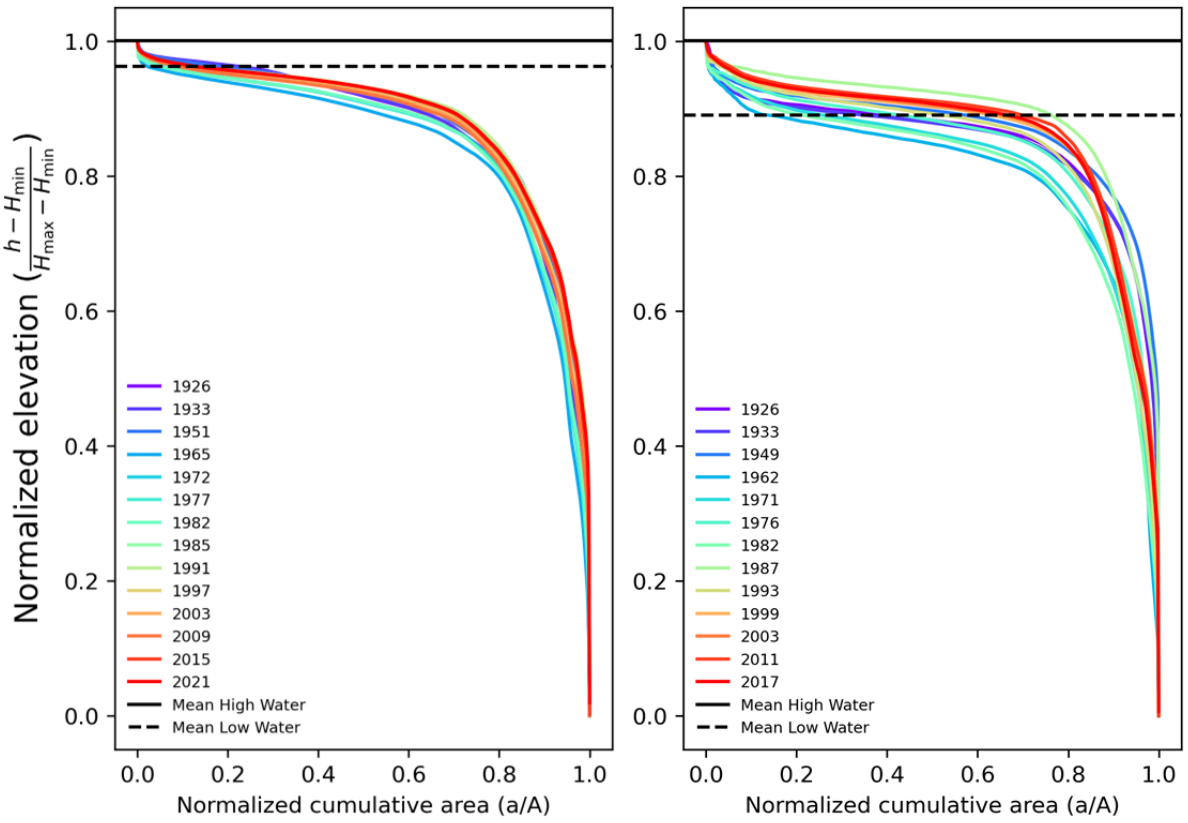

Figure A.23: Normalized hypsometric curves between MHW and -50m NAP for the Marsdiep basin (left) and the Eierlandse Gat basin (right).

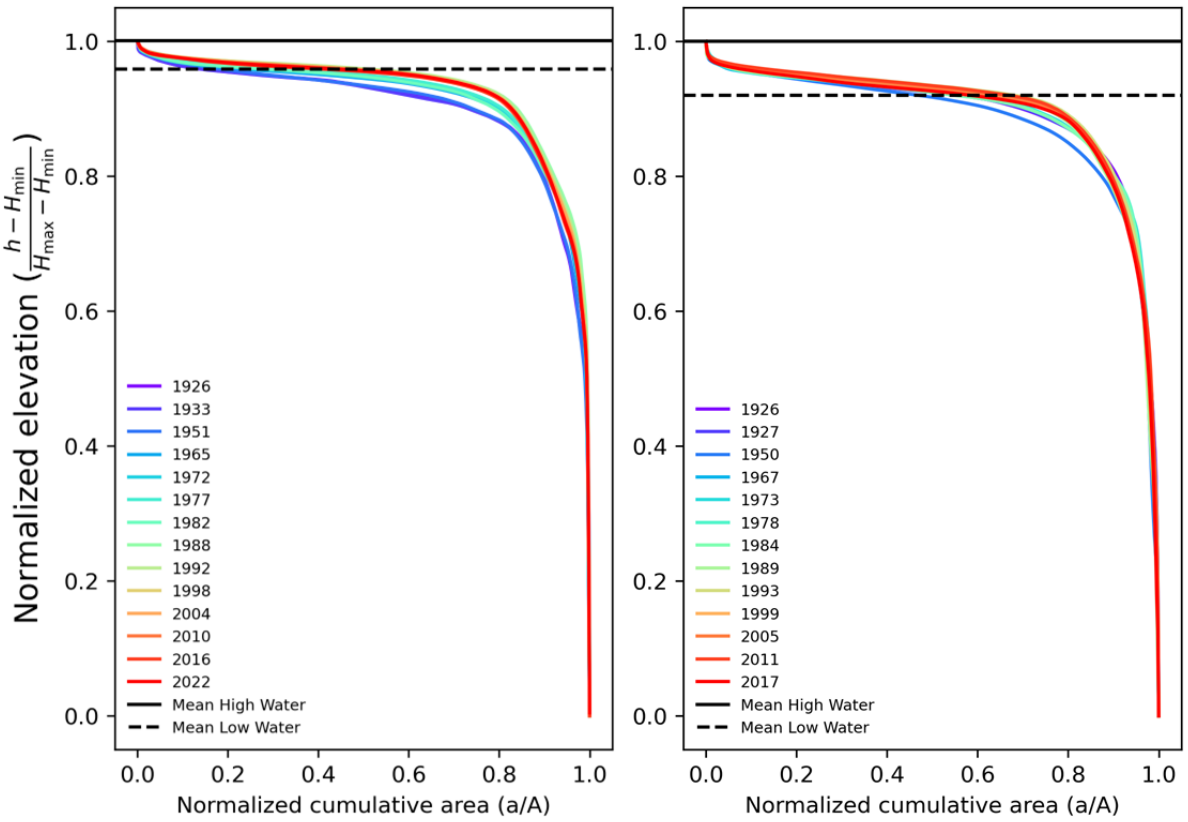

Figure A.24: Normalized hypsometric curves between MHW and -50m NAP for the Vlie Inlet basin (left) and the Ameland Inlet basin (right).

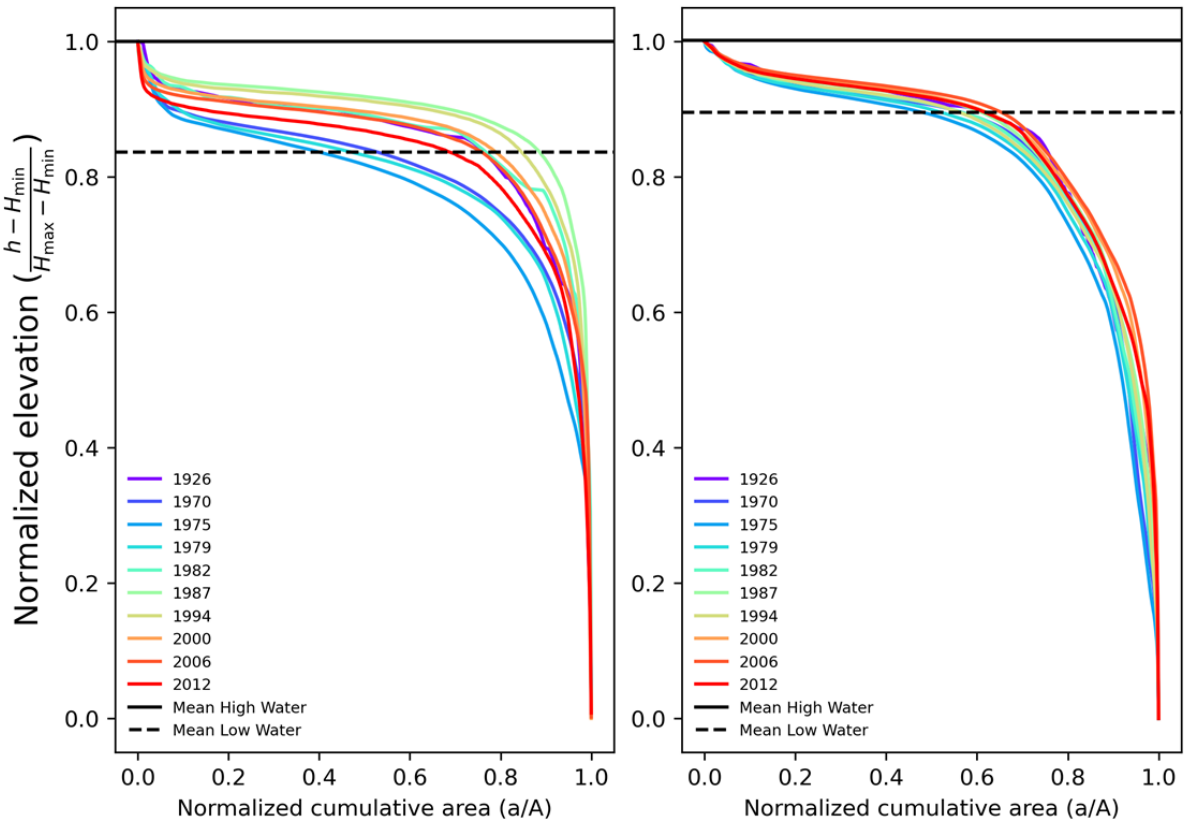

Figure A.25: Normalized hypsometric curves between MHW and -50m NAP for the Pinkegat basin (left) and the Zoutkamperlaag basin (right).

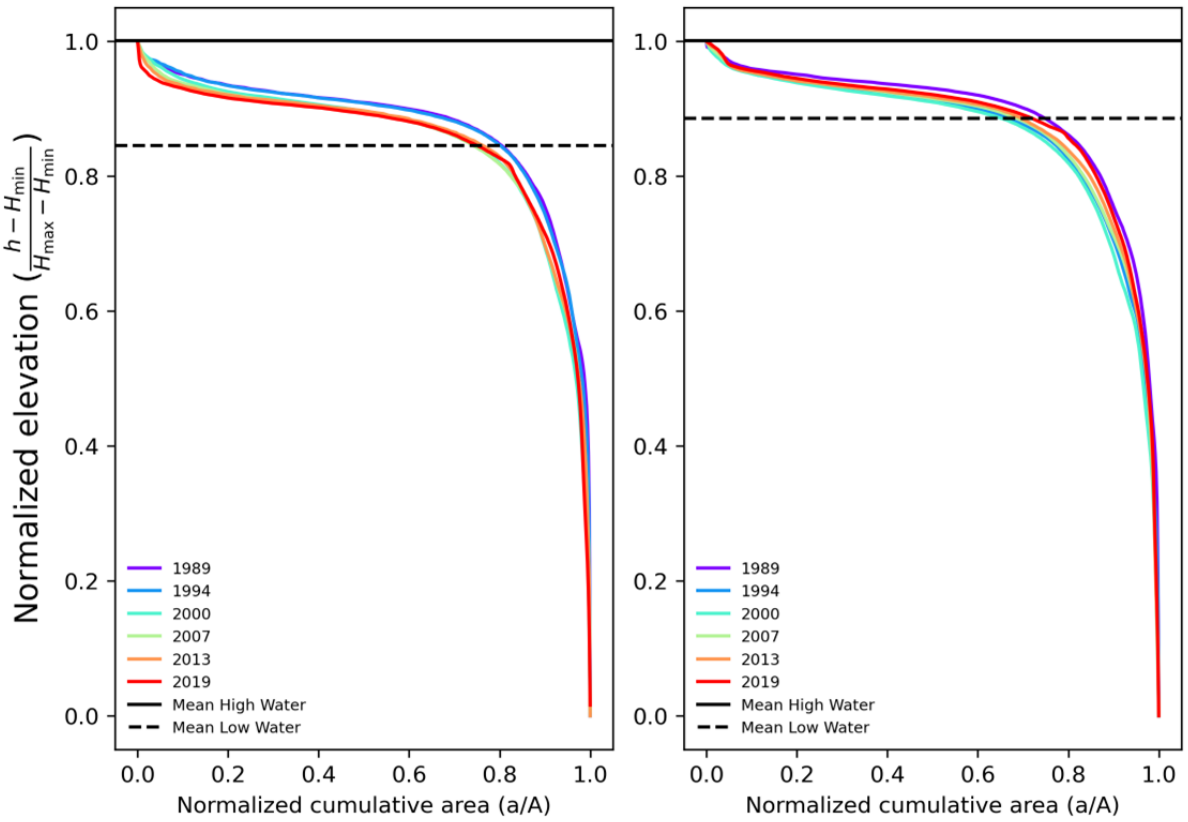

Figure A.26: Normalized hypsometric curves between MHW and -50m NAP for the Eijlanderbalg basin (left) and the Lauwers basin (right).

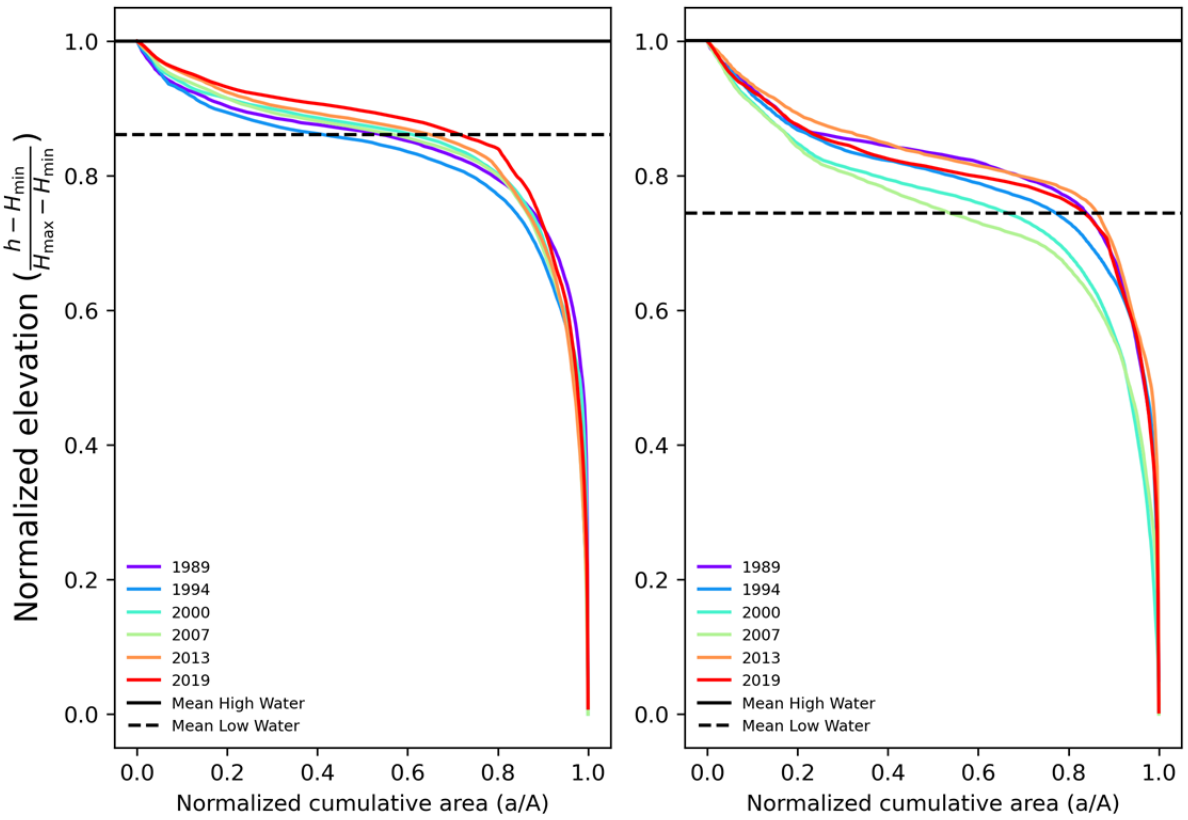

Figure A.27: Normalized hypsometric curves between MHW and -50m NAP for the Schild basin (left) and the Sparregat basin (right).

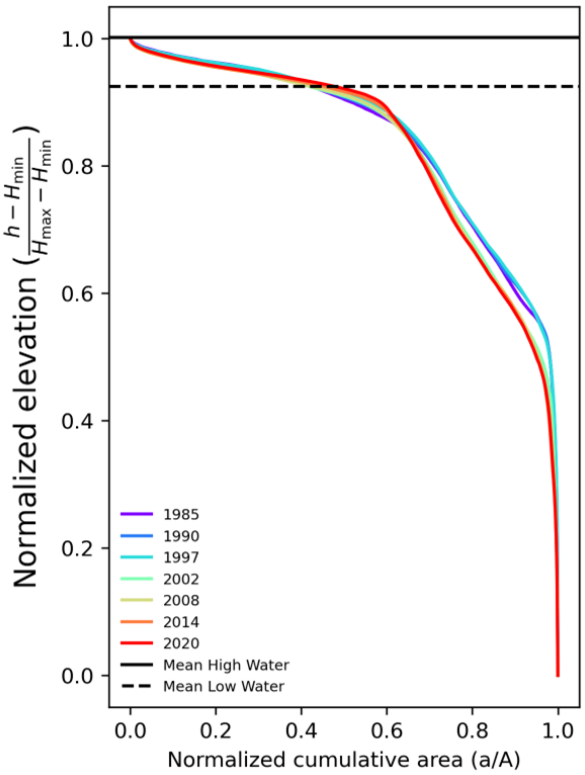

Figure A.28: Normalized hypsometric curve between MHW and -50m NAP for the Ems-Dollard estuary.

A.4. Influence of grid resolution on normalized hypsometric curve

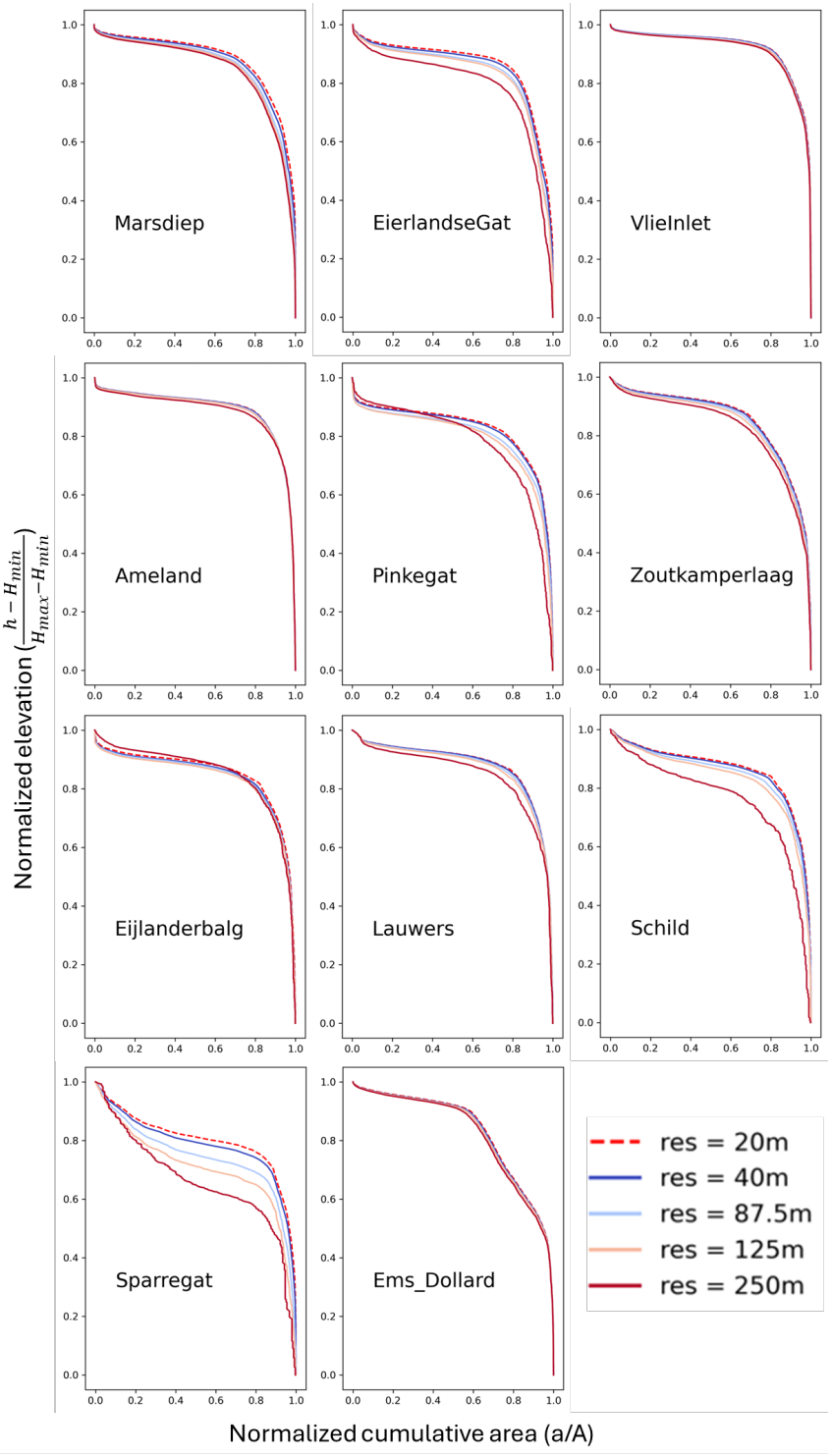

Figure A.29: Influence of down scaling high resolution grids for all considered full-basin grids. Based on most recent grids.

A.5. Fitting results for all theoretical curves

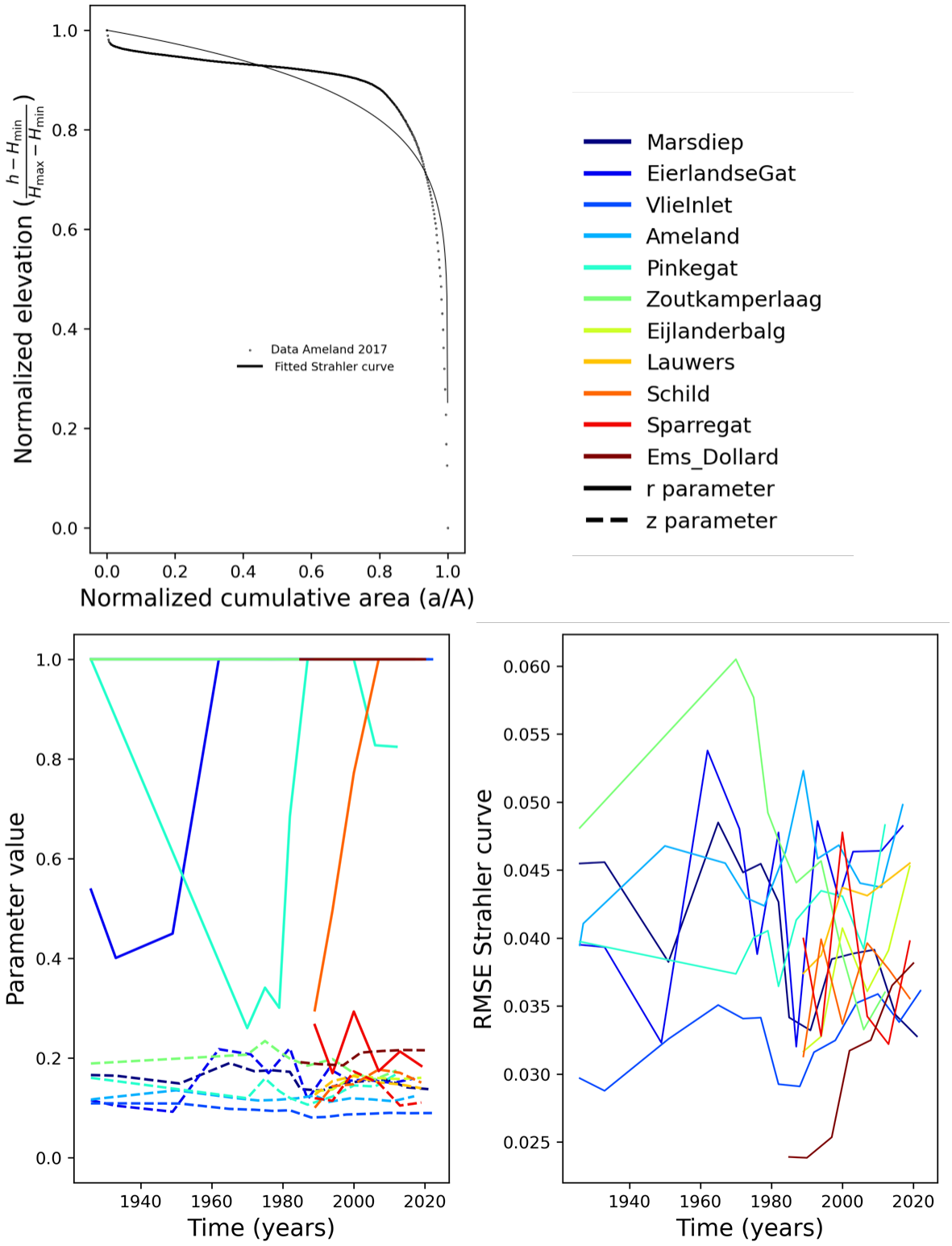

Figure A.30: Fitting results for the original Strahler function (Strahler, 1952).

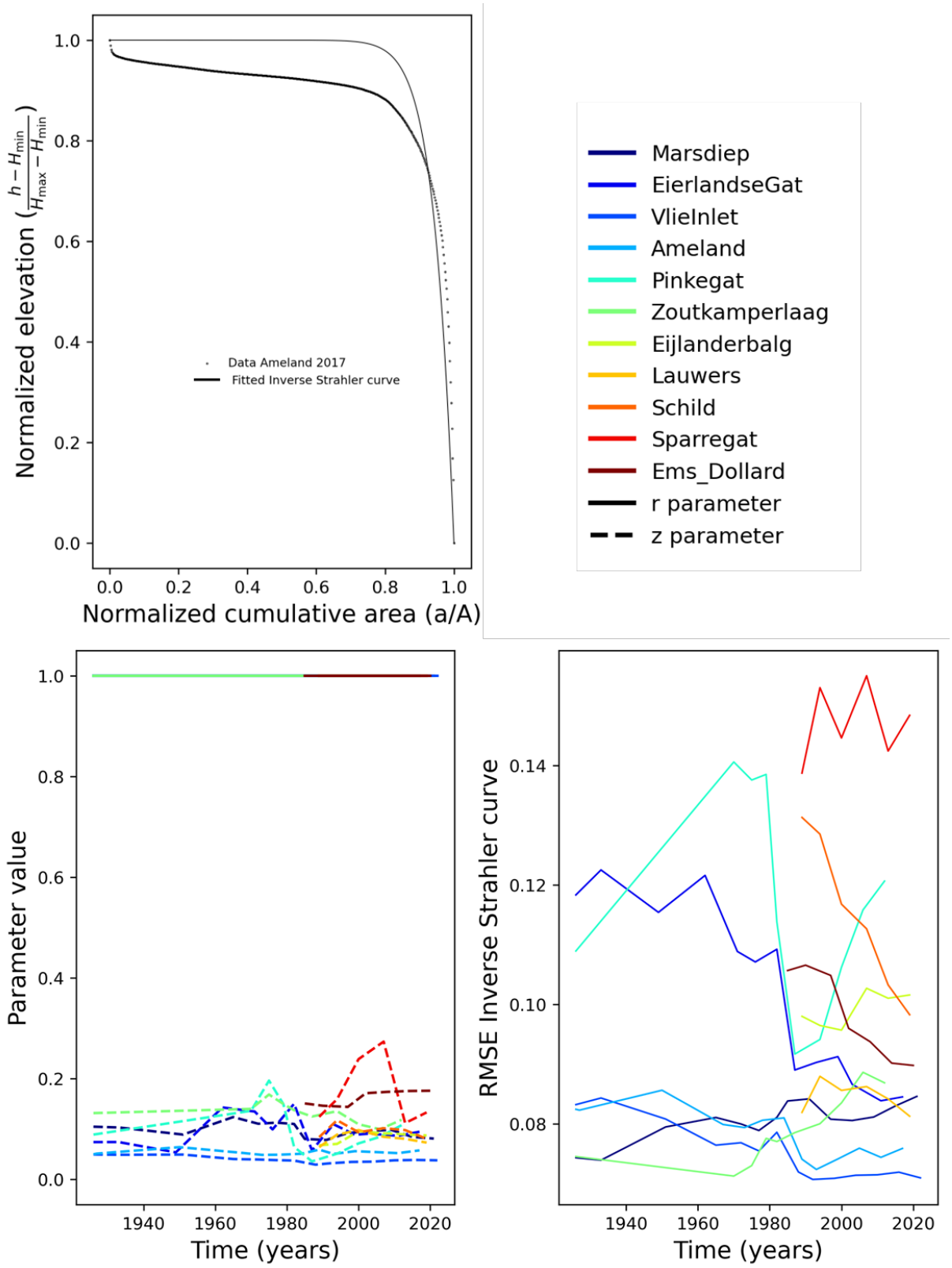

Figure A.31: Fitting results for the inverse Strahler function. (Leuven et al., 2018).

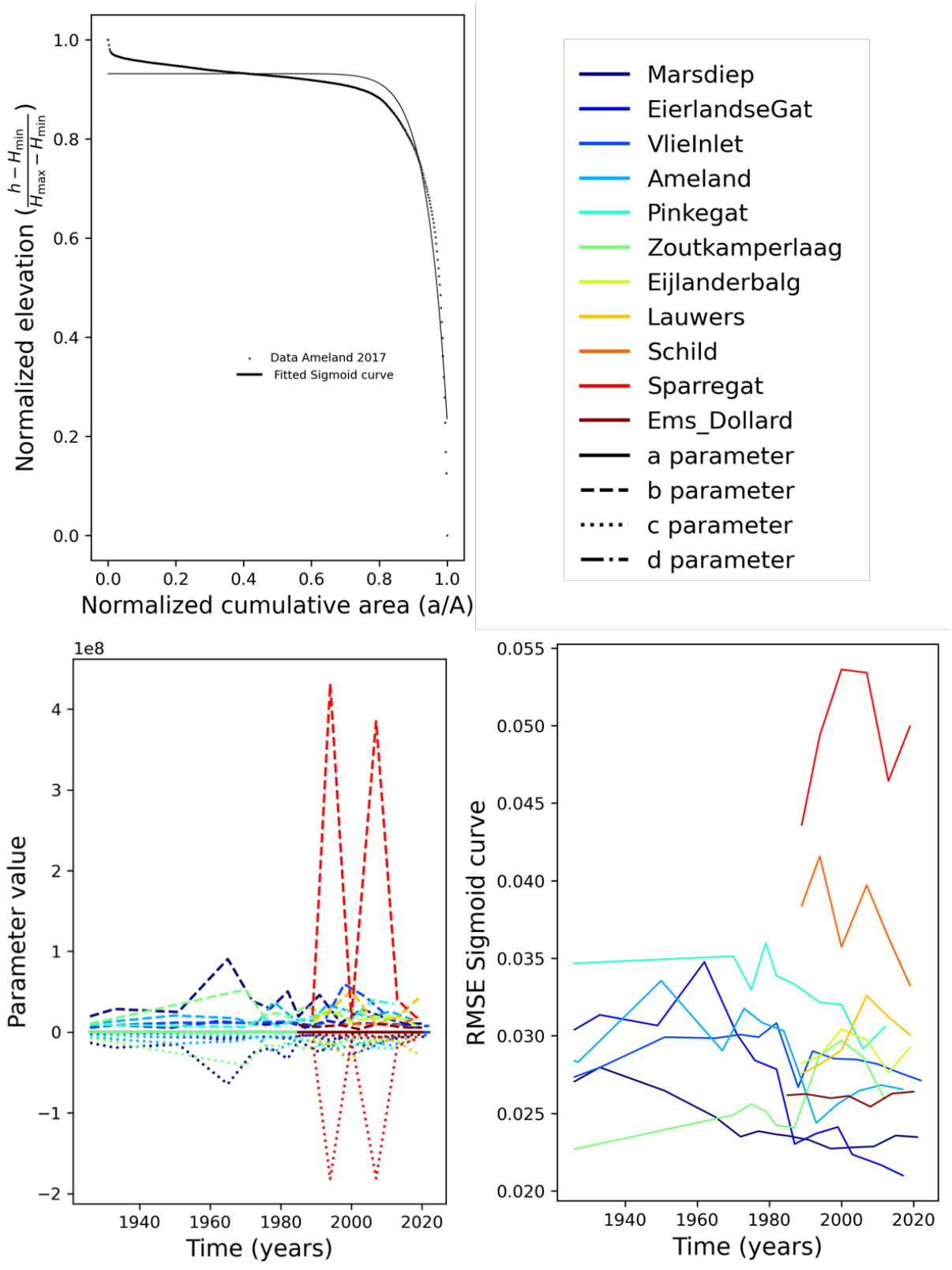

Figure A.32: Fitting results for the Sigmoid curve (Sarkar & Patel, 2011).

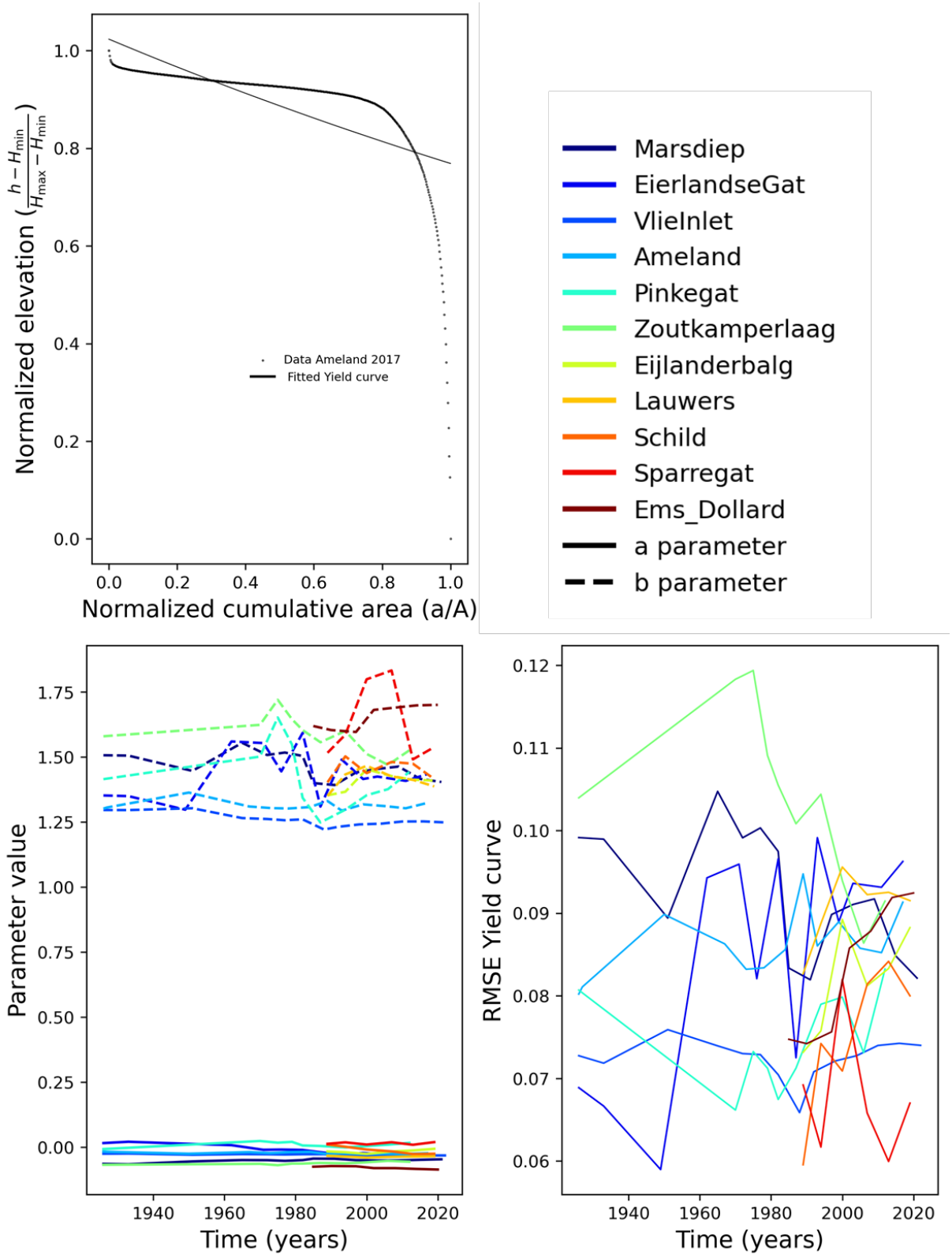

Figure A.33: Fitting results Yield curve (Sarkar & Patel, 2011).

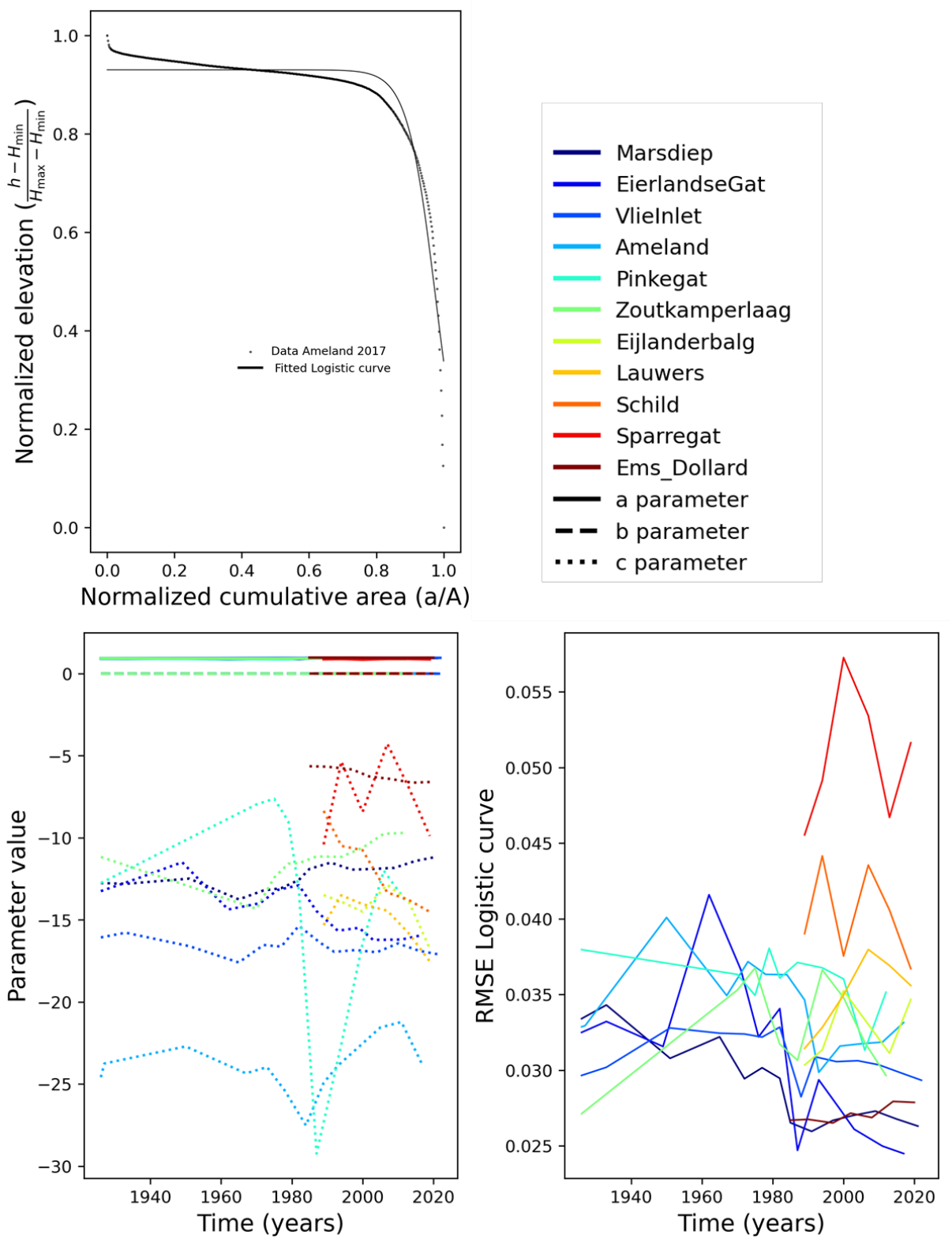

Figure A.34: Fitting results Logistic curve (Sarkar & Patel, 2011).

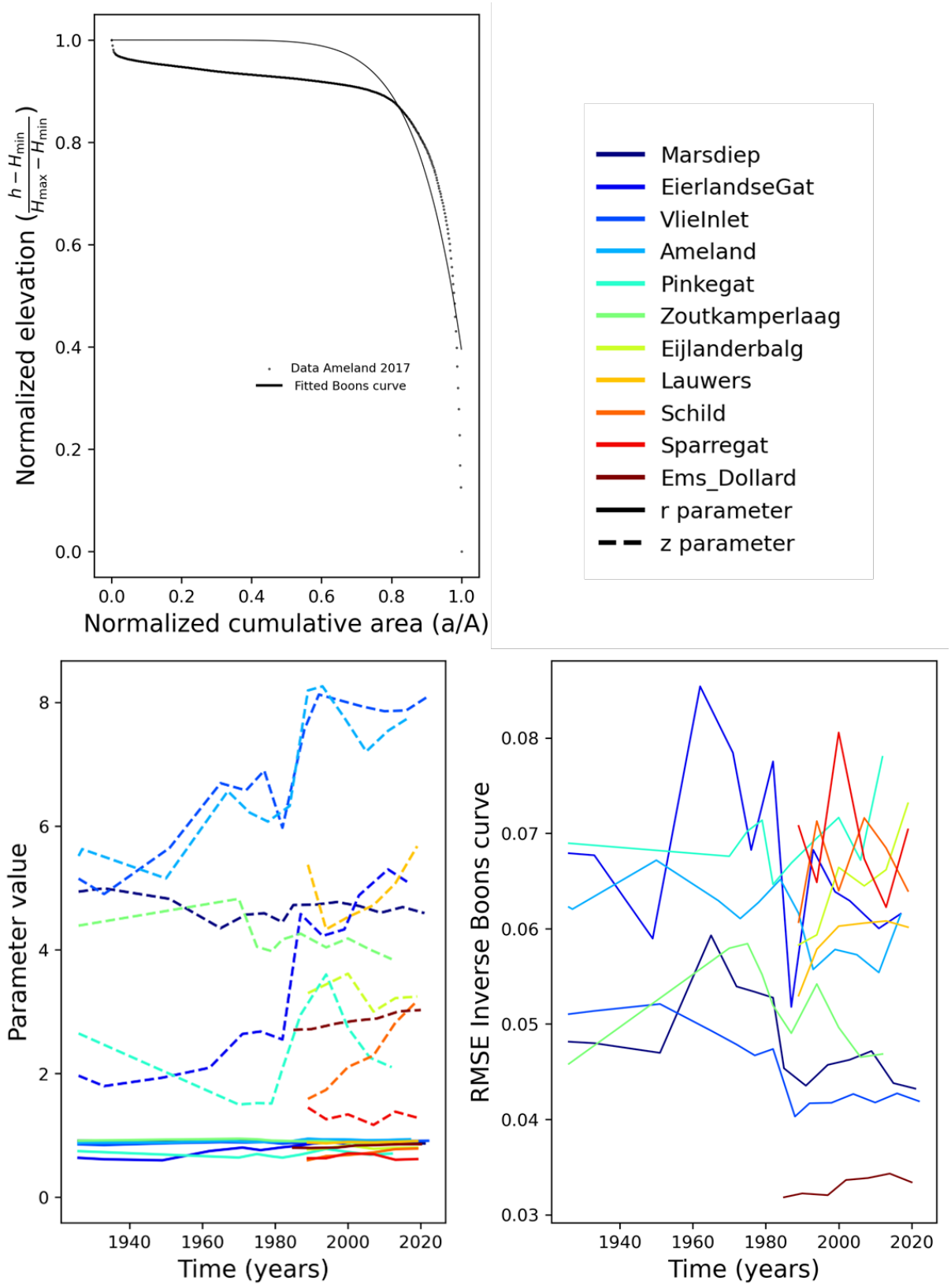

Figure A.35: Fitting results for the Boons curve (Boon III & Byrne, 1981).

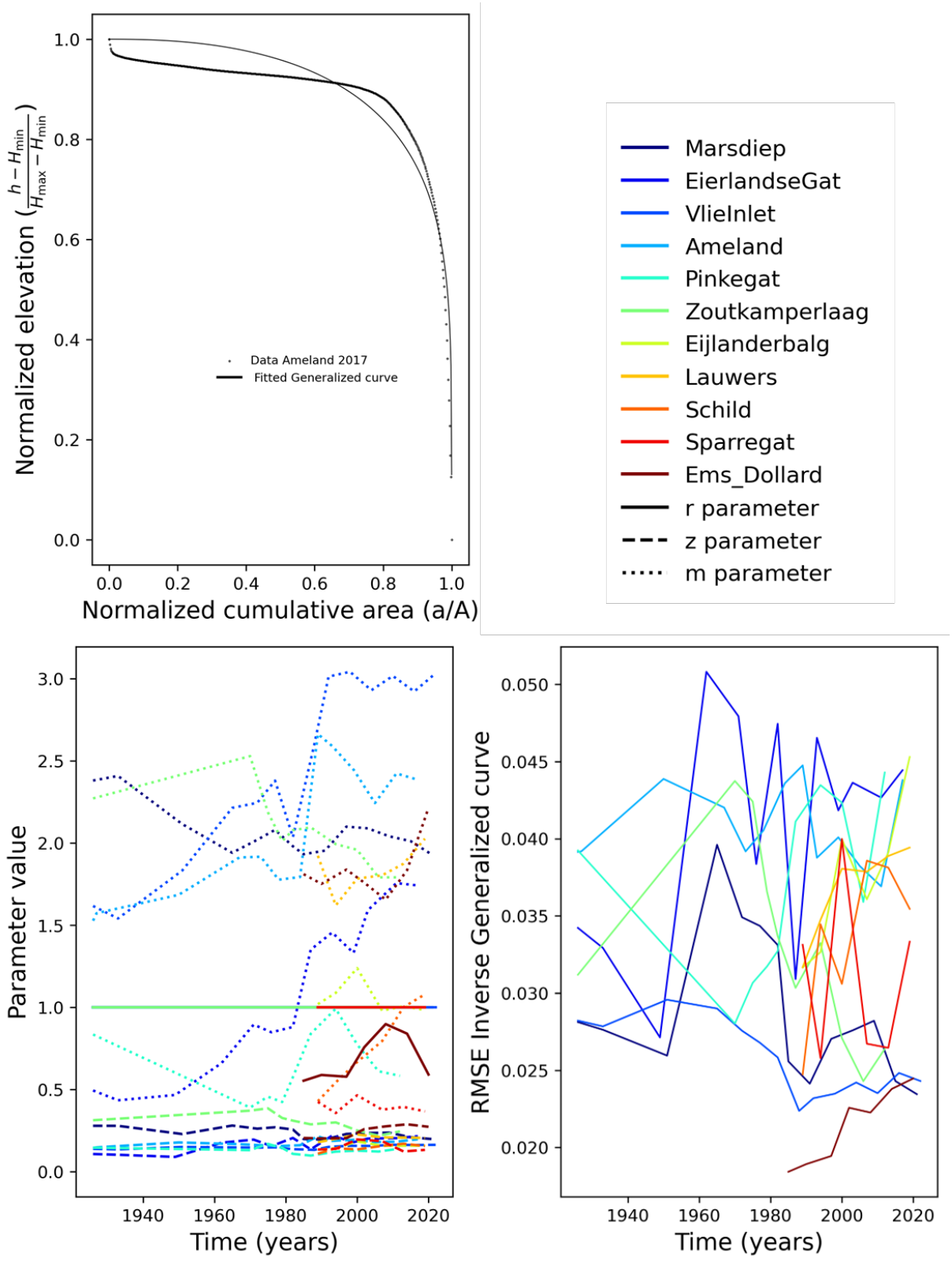

Figure A.36: Fitting results for the Generalized curve (Bajracharya & Jain, 2021).

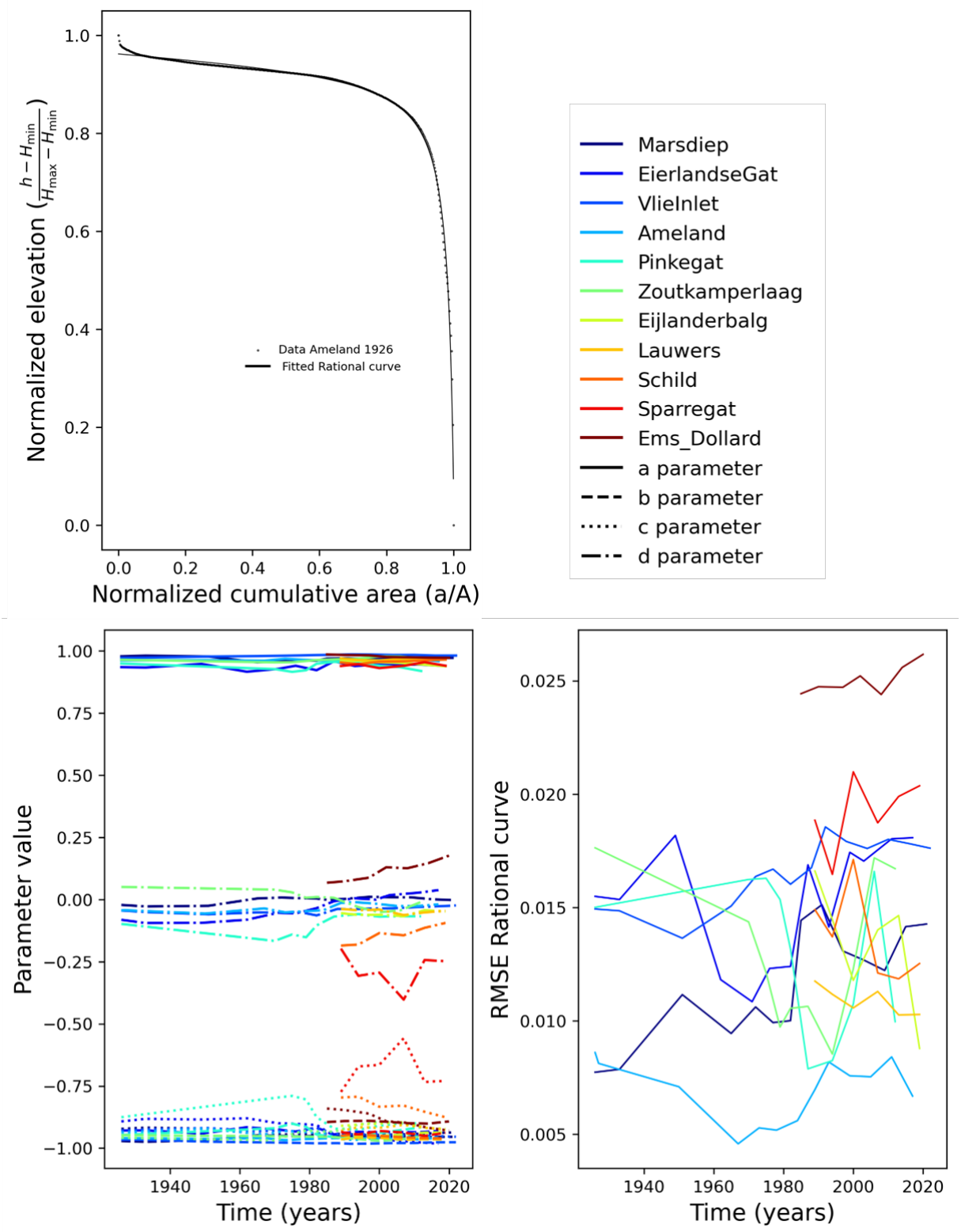

Figure A.37: Fitting results for the rational curve (Sarkar & Patel, 2011).

A.6. Simplification of the Rational curve

A.6.1. Fitting with constant parameters

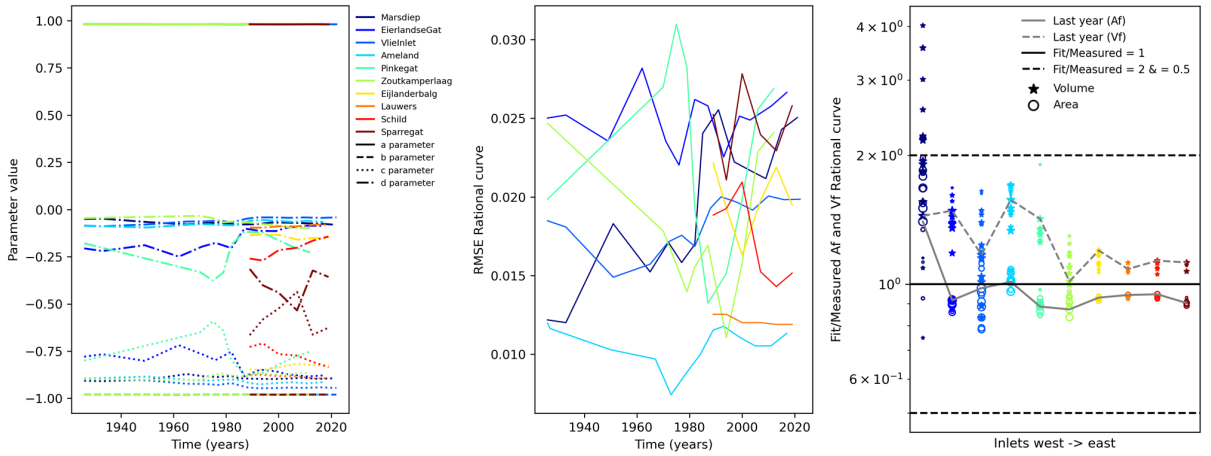

Figure A.38: Fitting results of the rational curve on the full-basin scale with constant values of 0.98 (+0.0001) and -0.98 (-0.0001) for the *a* and *b* parameter respectively.

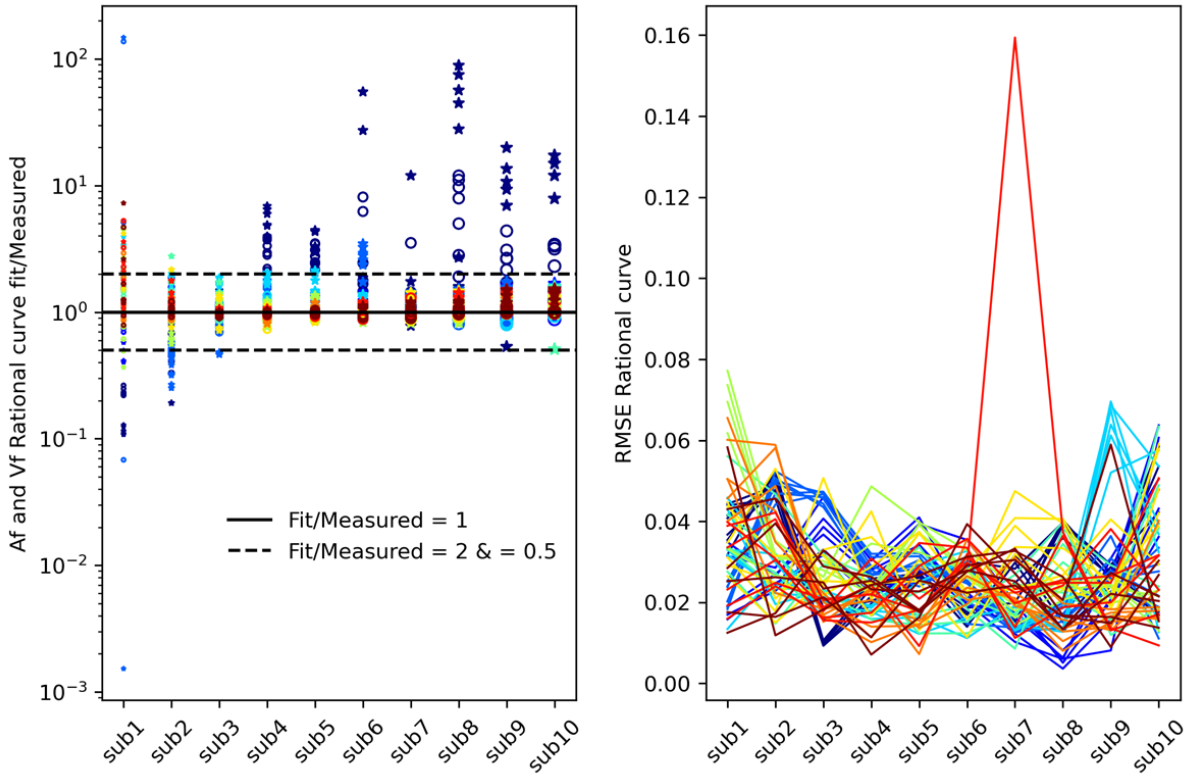

Figure A.39: Fitting results of the rational curve on the annular sub-section scale with constant values of 0.98 (+0.0001) and -0.98 (-0.0001) for the *a* and *b* parameter respectively.

A.6.2. First correlation simplification Rational curve

From the parameter correlations (Fig. A.40 - A.42), it is possible to simplify the curves to contain only three parameters. The resulting equations are listed below and the fitting quality for all fits is shown in figures A.43 - A.47.

For the tidal basins, excluding the Ems-Dollard estuary:

$$\frac{h - Hmin}{Hmax - Hmin} = \frac{a - 0.97ax - 0.02x}{1 + cx + dx^2} \tag{A.1}$$

And:

$$\frac{h - Hmin}{Hmax - Hmin} = \frac{a + bx}{1 + cx - 1.04cx^2 - x^2} \tag{A.2}$$

Figure A.43 shows that, compared to the rational fit with four parameters, the simplified curve containing only the a, c & d parameter leads to slightly higher values for the RMSE and increased variation in the approximated intertidal area and volume for some Marsdiep grids. With the substitution of c for d (Eq. A.2, Fig. A.44), the variability of the approximations for the Marsdiep is less, but the approximations for the Sparregat and Zoutkamperlaag curves are no longer reliable. As the variation resulting from Eq. A.1 is still mainly within a factor two for all basins, this simplification is preferable. Only for the Marsdiep the simplified curve is not able to approximate the area and volume of the intertidal zone within a factor of two.

For the Ems-Dollard estuary alone:

$$\frac{h - Hmin}{Hmax - Hmin} = \frac{a + bx}{1 + cx - 1.14cx^2 - 0.9x^2} \tag{A.3}$$

And:

$$\frac{h - Hmin}{Hmax - Hmin} = \frac{a + bx}{1 + 6.2ax - 6.95x + dx^2} \tag{A.4}$$

And:

$$\frac{h - Hmin}{Hmax - Hmin} = \frac{a + bx}{1 + cx - 7.04ax^2 + 7x^2} \tag{A.5}$$

For the Ems-Dollard estuary all three simplifications do not cause a strong increase in RMSE compared to the four-parameter rational curve. All three fitted curves lead to strong correlation between either a-c or a-d again (Fig A.49-A.51). For the simplification based on d-a correlation (Eq. A.5), the highest R^2 and r values are found for the a-c

correlation (Fig. A.51) and therefore this relation is used for a second simplification.

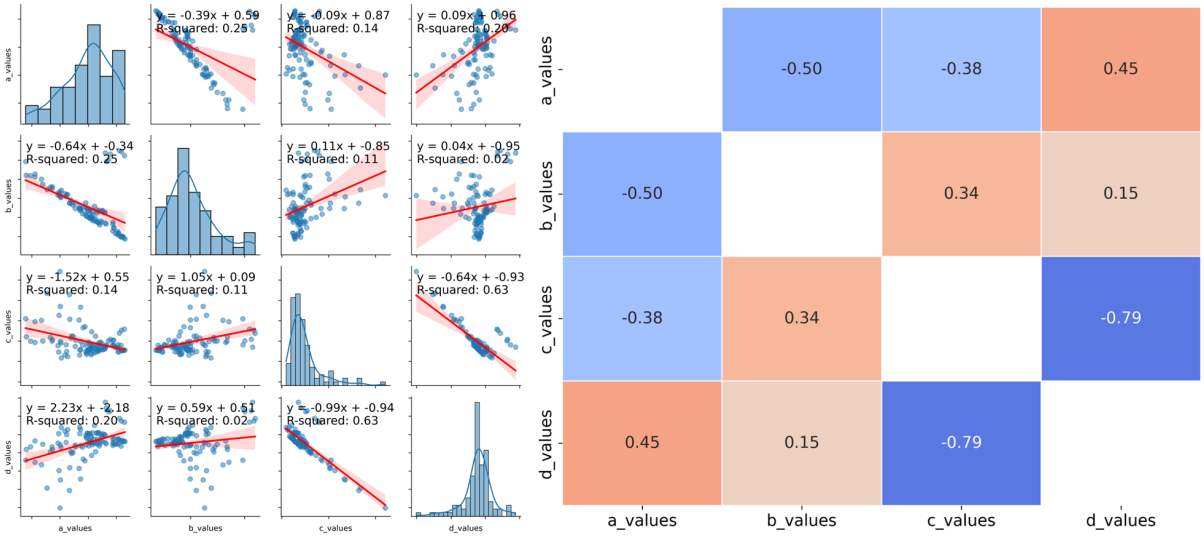

Figure A.40: Correlation fitting parameters (a,b,c,d) Rational curve on all full-basin grids.

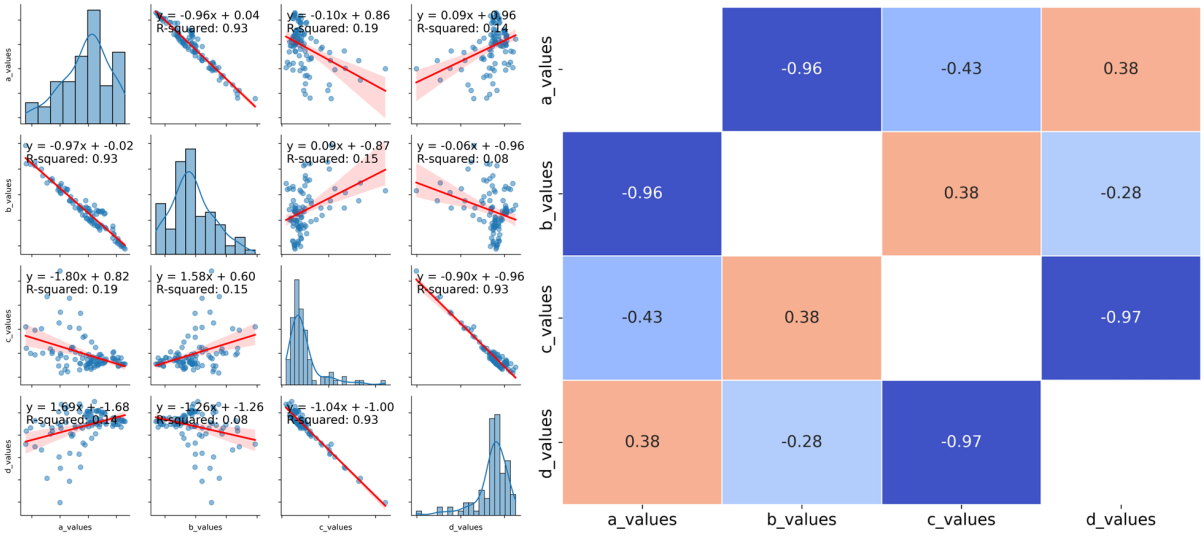

Figure A.41: Correlation fitting parameters (a,b,c,d) Rational curve when excluding the Ems-Dollard estuary on the full-basin grids.

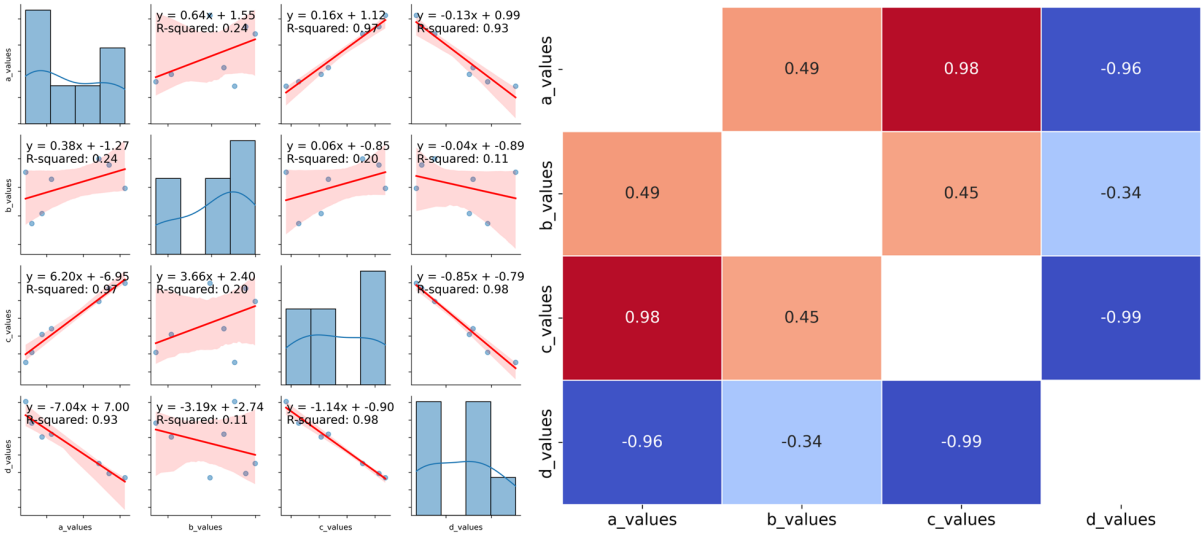

Figure A.42: Correlation fitting parameters (a,b,c,d) Rational curve for only the Ems-Dollard estuary on the full-basin grid.

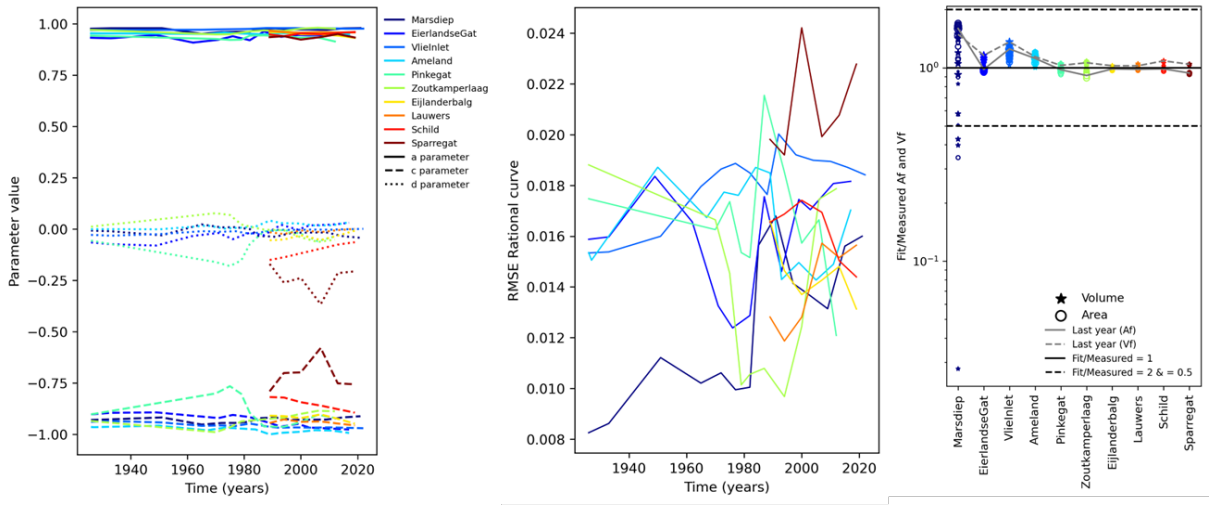

Figure A.43: Results of fitting the simplified rational curve containing a, c & d (based on b-a correlation, Eq. A.1) parameter to the tidal basin curves. Marker size increases with time.

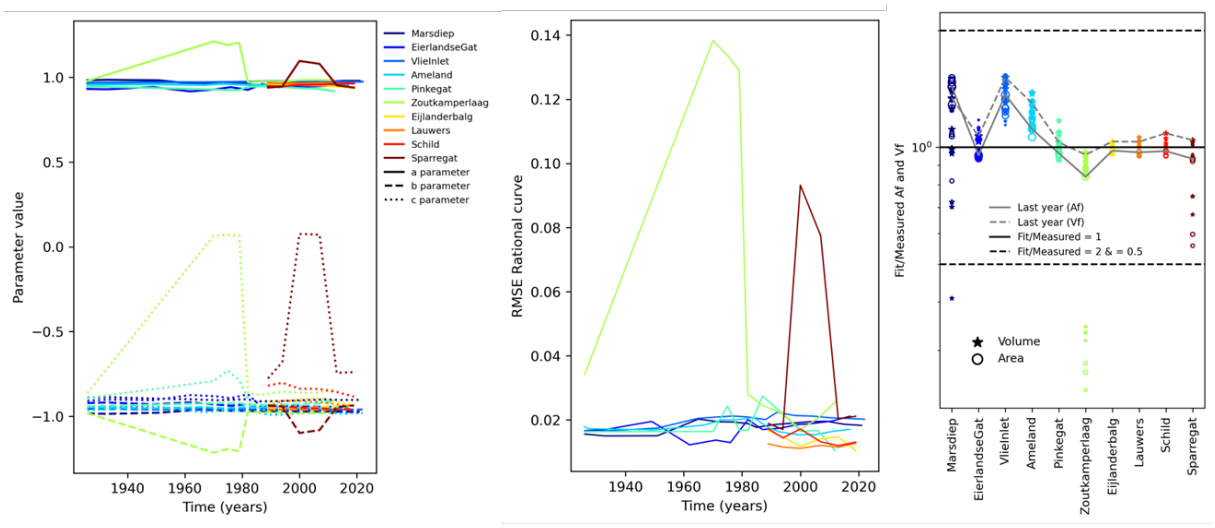

Figure A.44: Results of fitting the simplified rational curve containing a, b & c (based on d-c correlation, Eq. A.2) parameter to the tidal basin curves. Marker size increases with time.

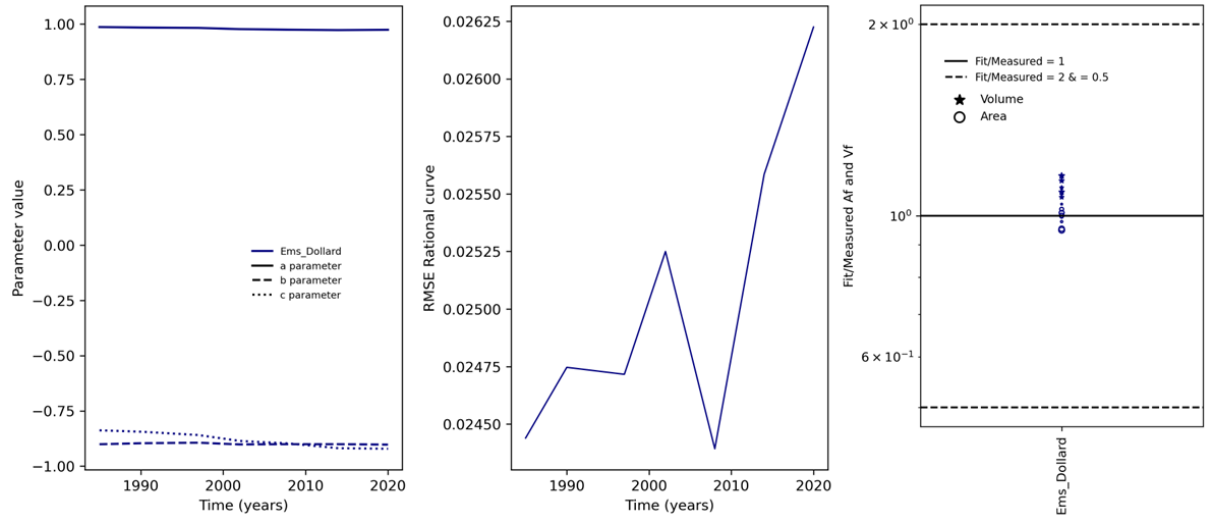

Figure A.45: Results of fitting the simplified rational curve containing a, b & c (based on d-c correlation, Eq. A.3) parameter to the Ems-Dollard estuary. Marker size increases with time.

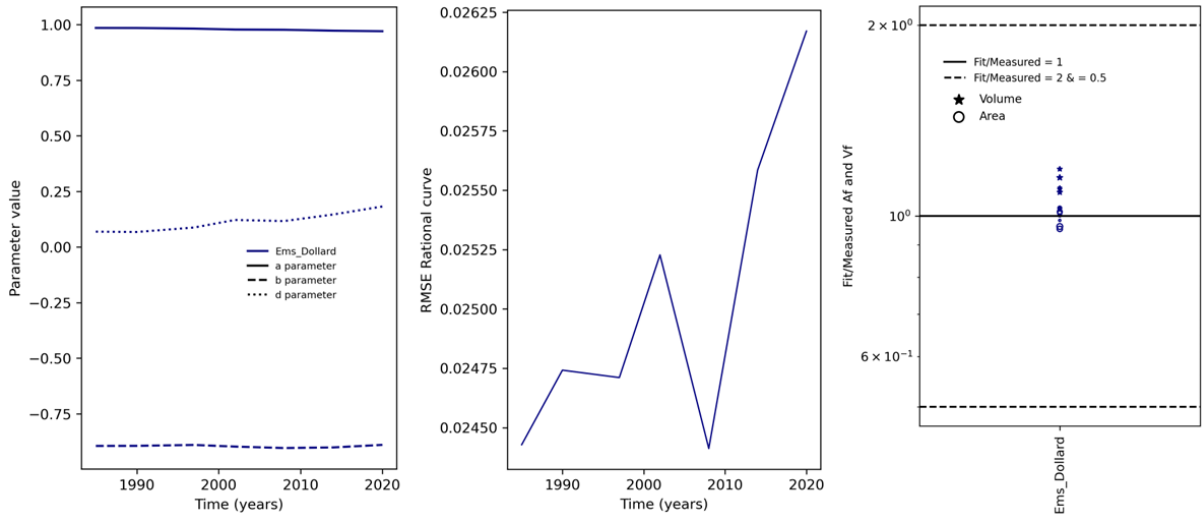

Figure A.46: Results of fitting the simplified rational curve containing a, b & d (based on c-a correlation, Eq. A.4) parameter to the Ems-Dollard estuary. Marker size increases with time.

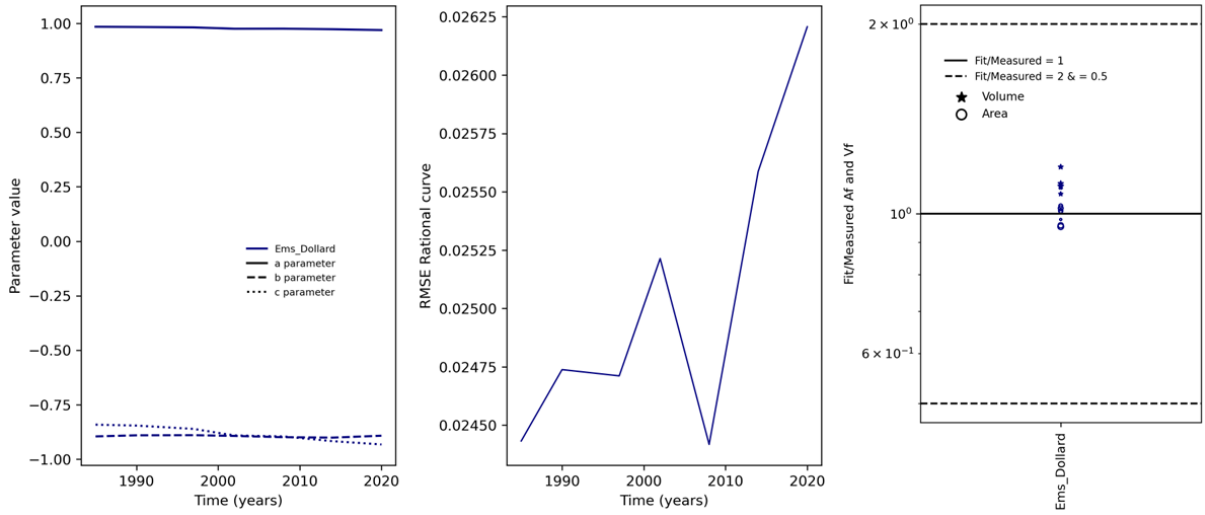

Figure A.47: Results of fitting the simplified rational curve containing a, b & c (based on d-a correlation, Eq. A.5) parameter to the Ems-Dollard estuary. Marker size increases with time.

A.6.3. Second correlation simplification Rational curve

Based on further correlation of the parameters of the most suitable simplified curves, a second simplification is possible for both the tidal basins and the Ems-Dollard estuary (Fig. A.48 & A.51). The equations can then be simplified to only contain two parameters:

For the tidal basins, excluding the Ems-Dollard estuary:

$$\frac{h - Hmin}{Hmax - Hmin} = \frac{a - 0.97ax - 0.02x}{1 + cx - 0.99cx^2 - 0.95x^2} \tag{A.6}$$

Simplifying the rational curve to contain only two parameters for the tidal basins still

results in RMSE values below 0.1 (Fig. A.52). For the Marsdiep, now all volume and area approximations are within a factor two and only for the Vlie Inlet the volume of the intertidal flats is overestimated up to three times (Fig. A.52).

For the Ems-Dollard estuary alone:

$$\frac{h - Hmin}{Hmax - Hmin} = \frac{a + bx}{1 + 6.15ax - 6.90x - 7.04ax^2 + 7x^2} \tag{A.7}$$

Fitting the curve from Eq. A.7 does not increase the RMSE values and leads to comparable fitting results (Fig. A.53).

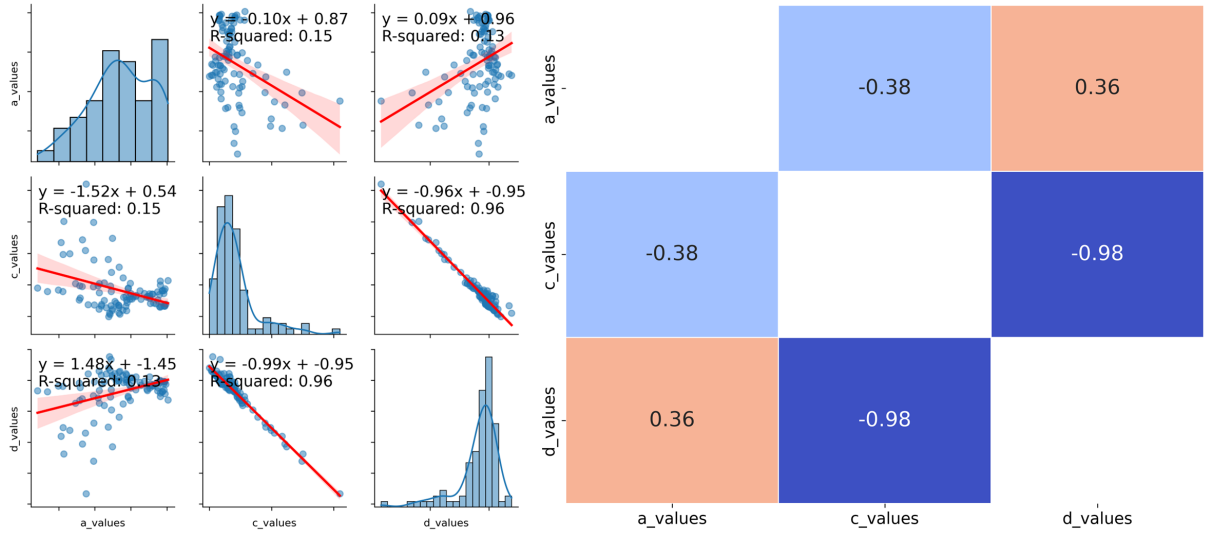

Figure A.48: Correlation fitting parameters (a,c,d) Rational curve when excluding the Ems-Dollard estuary on the full-basin grids

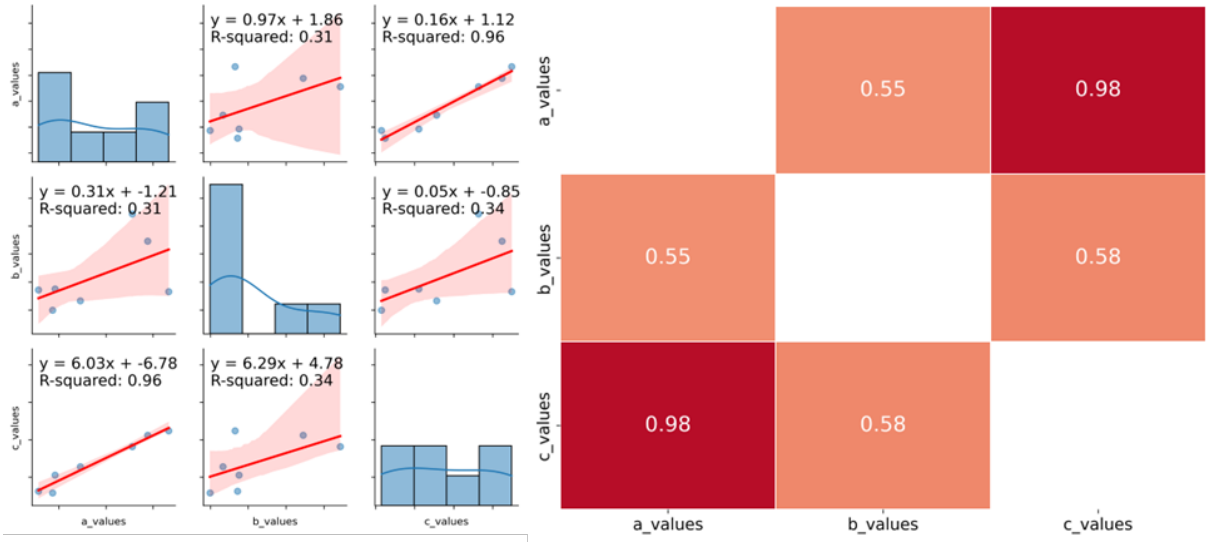

Figure A.49: Correlation fitting parameters (a,b,c) Rational curve for only the Ems-Dollard estuary on the full-basin grid. (Based on d-c correlation.)

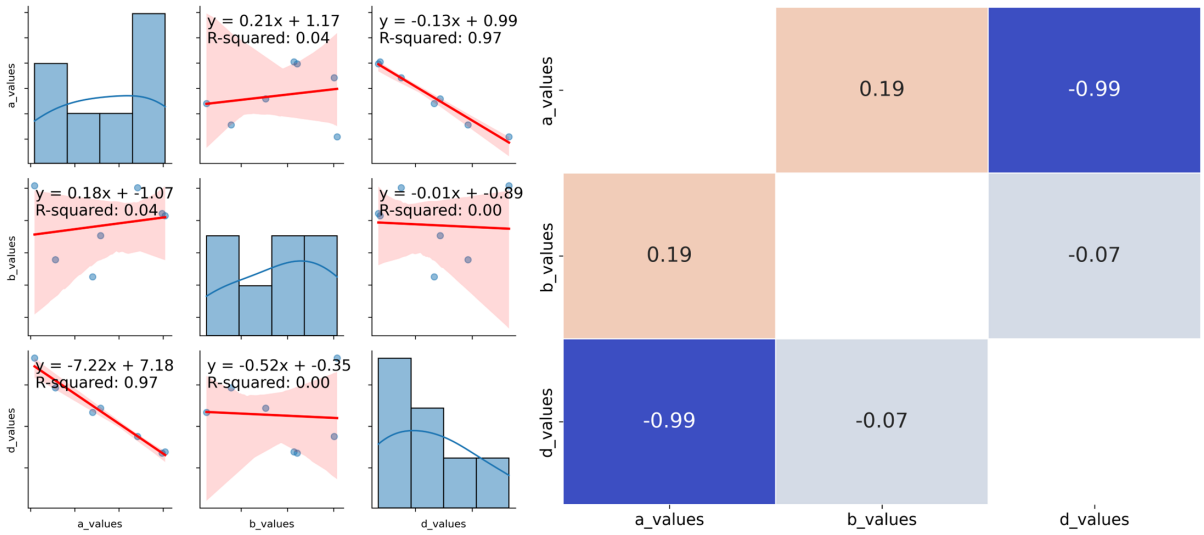

Figure A.50: Correlation fitting parameters (a,b,d) Rational curve for only the Ems-Dollard estuary on the full-basin grid.

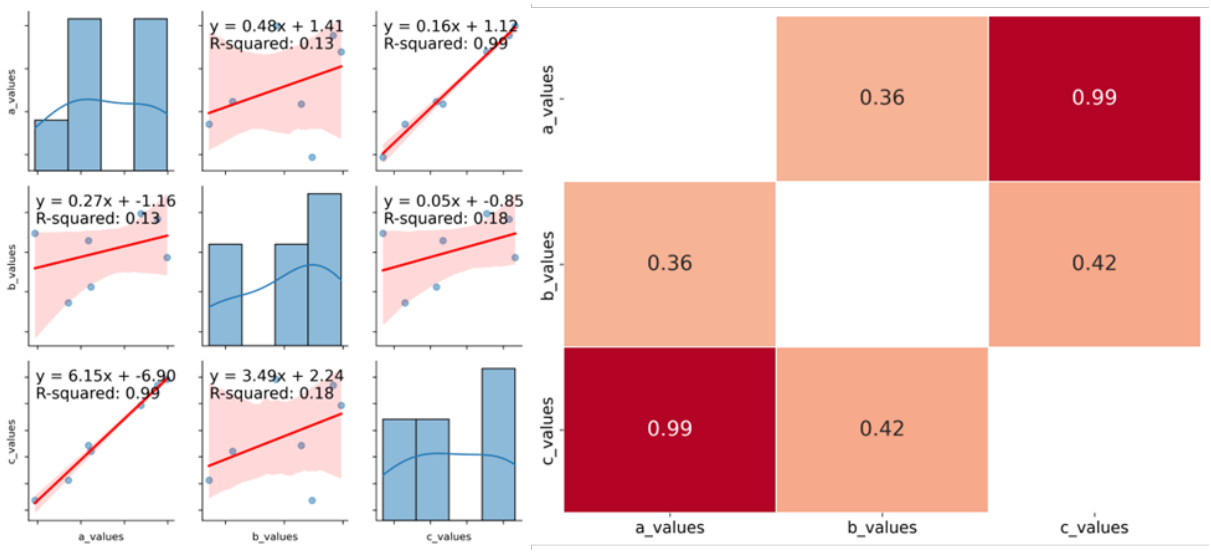

Figure A.51: Correlation fitting parameters (a,b,c) Rational curve for only the Ems-Dollard estuary on the full-basin grid. (Based on d-a correlation.)

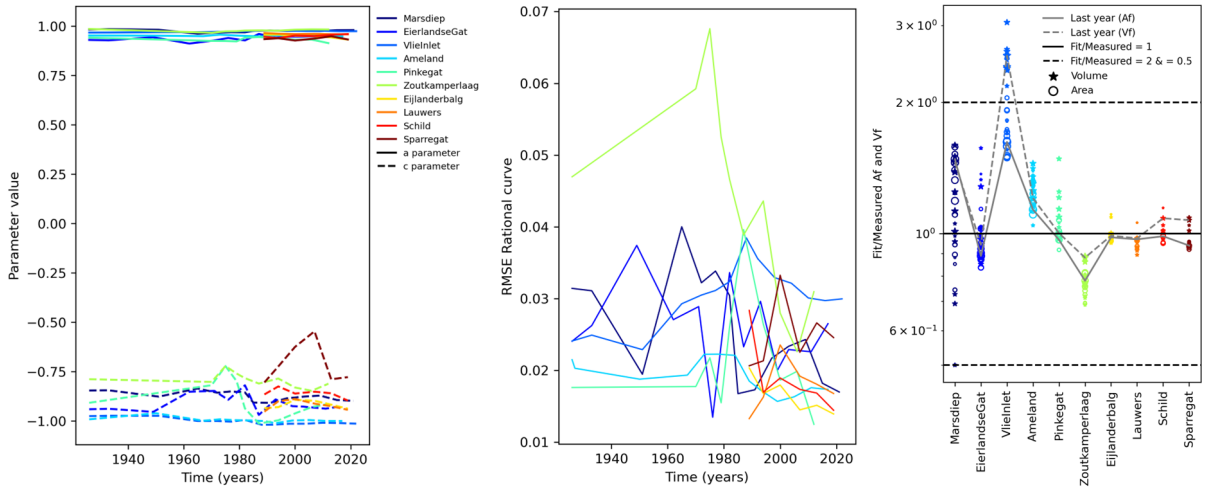

Figure A.52: Results of fitting the simplified rational curve containing a & c parameter (based on b-a & d-c correlation, Eq. A.6) to the tidal basin curves. Marker size increases with time

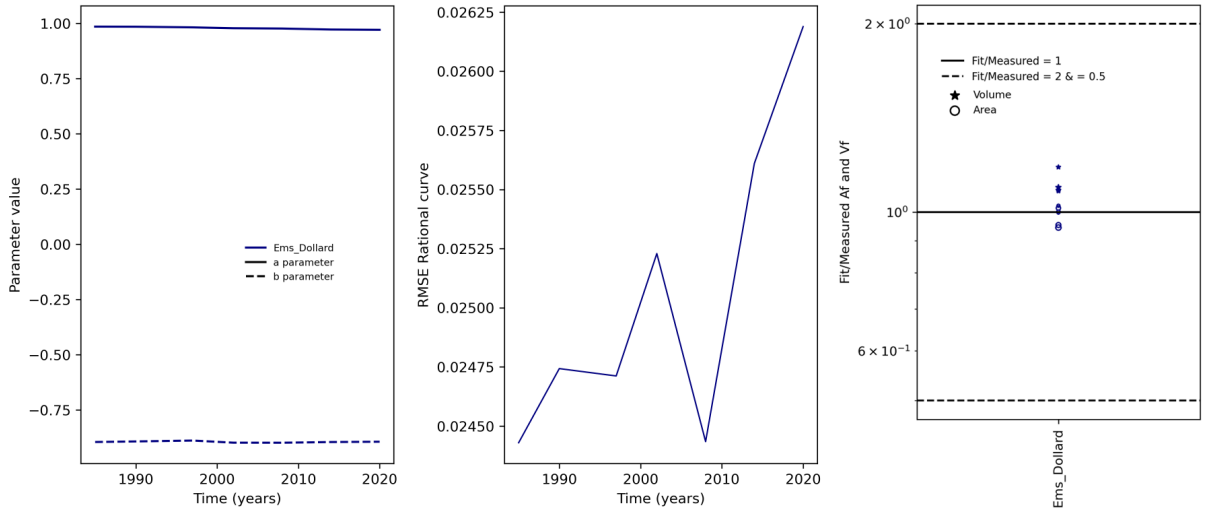

Figure A.53: Results of fitting the simplified rational curve containing a & b (based on c-a & d-a correlation, Eq. A.7) parameter to the Ems-Dollard estuary. Marker size increases with time.

Parameter influence simplified curve shape tidal basins

After simplification, the remaining parameters have different influences on the shape of the curve. For the tidal basin curve in equation A.6, the *a* parameter mainly influences the vertical displacement of the curve, whereas the *c* parameter mainly influences the horizontal displacement and the convexity-concavity (Fig. A.54). When fitted, both parameters can influence the shape of the curve and, therefore, cannot be interpreted separately.

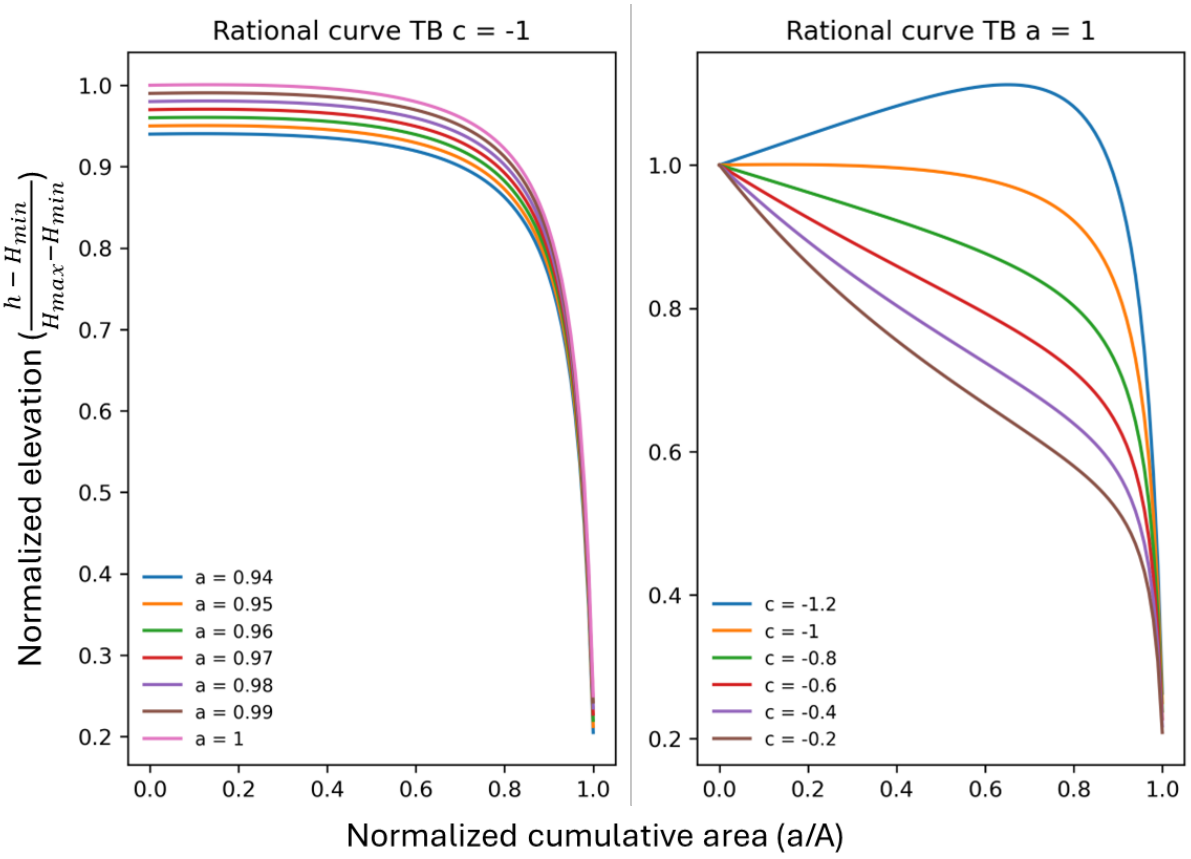

Figure A.54: Influence of *a* & *c* parameters on tidal basin curve shape for the simplified rational curve.

Parameter influence simplified curve shape Ems-Dollard estuary

For the Ems-Dollard estuary, the simplified curve creates curve shapes as shown in figure A.55. The *a* parameter influences convexity-concavity, and in addition changes the minimal and maximal extent of the curve on the x-axis. A decreasing value for *a* indicates increased convexity in the intertidal zone. The *b* parameter determines the vertical displacement of the curve on the y-axis and mainly affects the linear relationship between h/H and a/A. The impact on the convexity of the curve is minor compared to *a*.

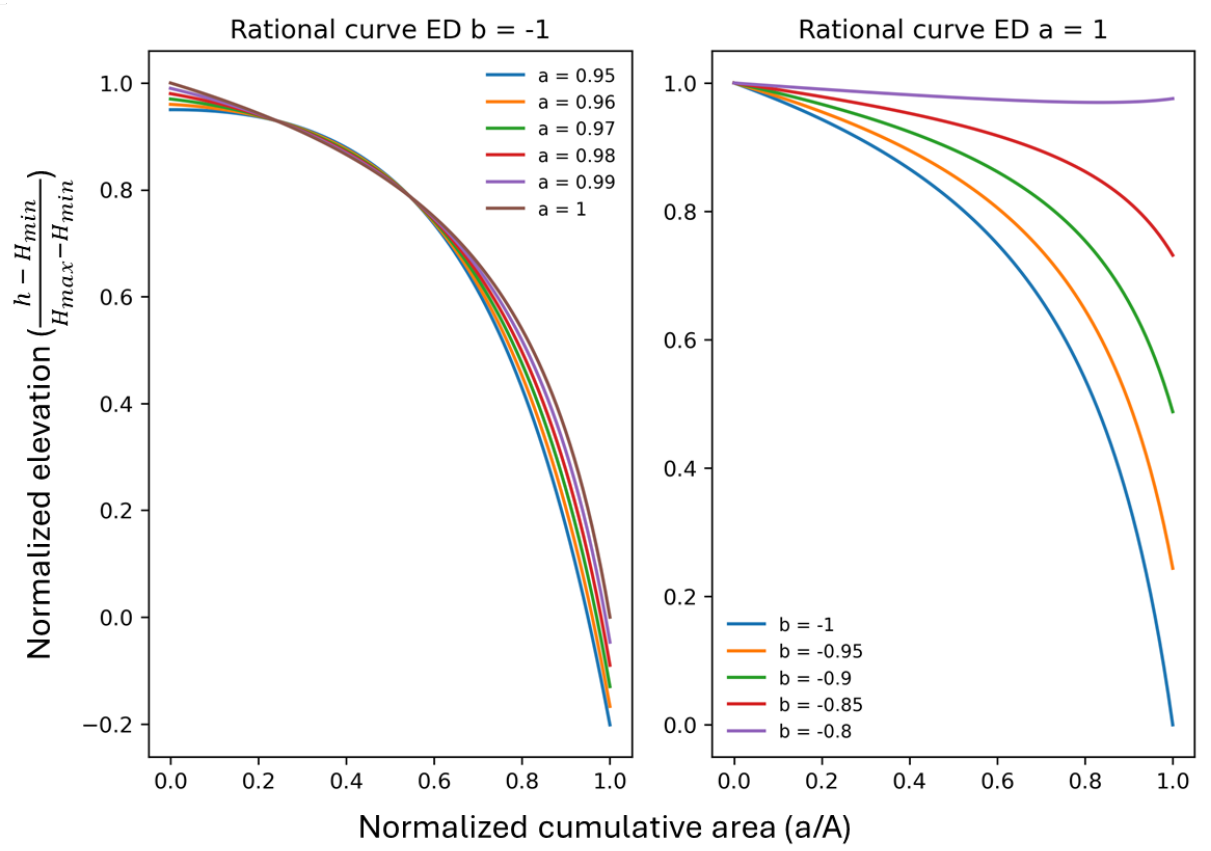

Figure A.55: Influence of a & b parameters on Ems-Dollard estuary curve shape for the simplified rational curve (Sarkar & Patel, 2011).

A.7. Quality of fit sub-section approach

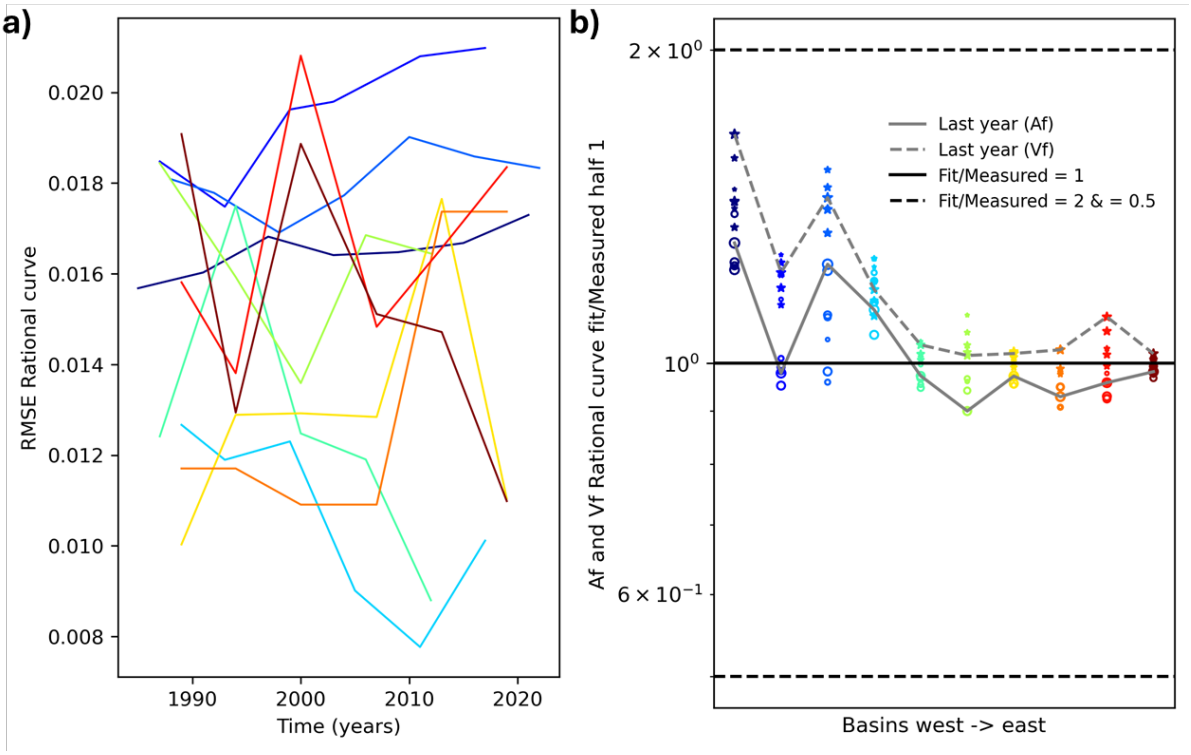

Figure A.56: RMSE values and comparison of fit and measured intertidal area and volume for the southern/western half basins.

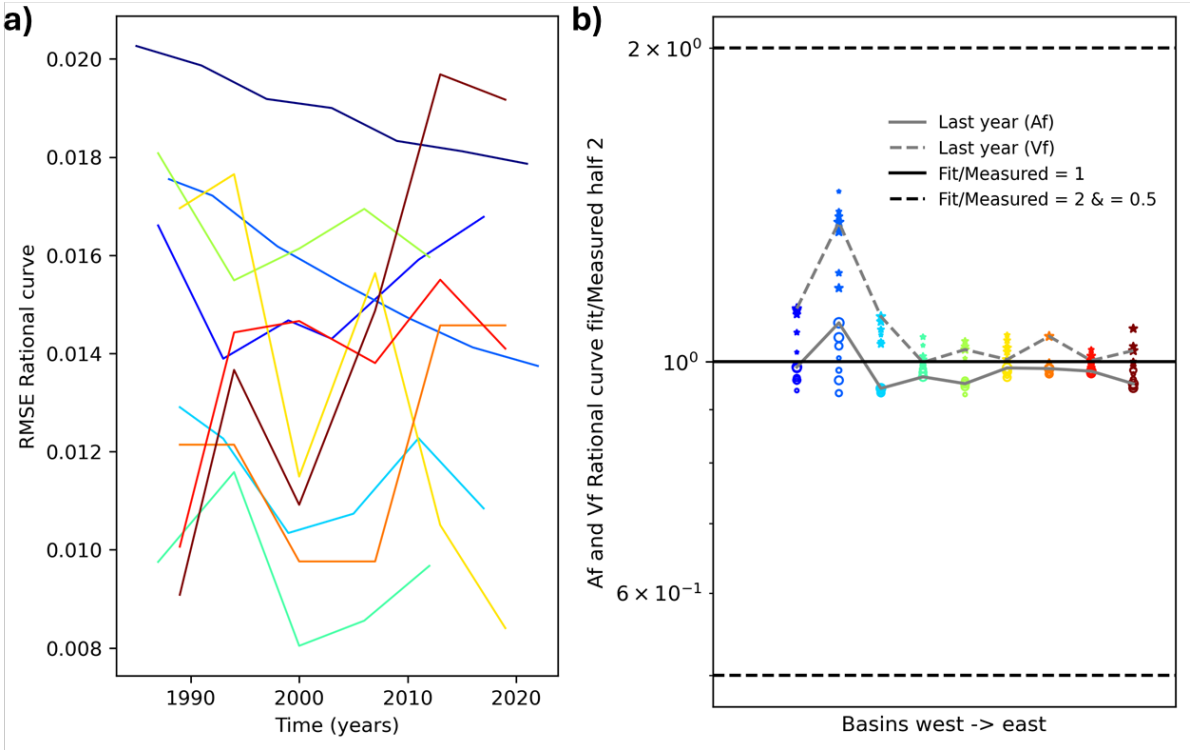

Figure A.57: RMSE values and comparison of fit and measured intertidal area and volume for the northern/eastern half basins.

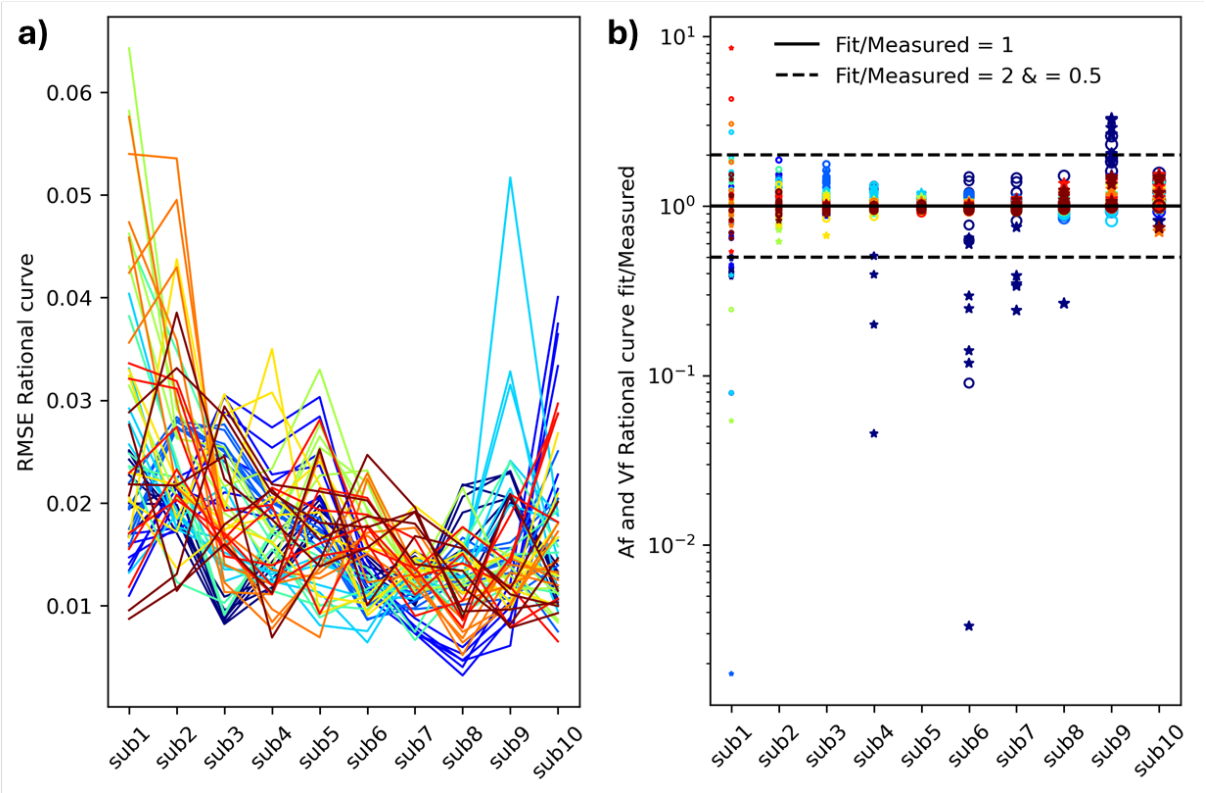

Figure A.58: RMSE values and comparison of fit and measured intertidal area and volume for the annular sub-sections.

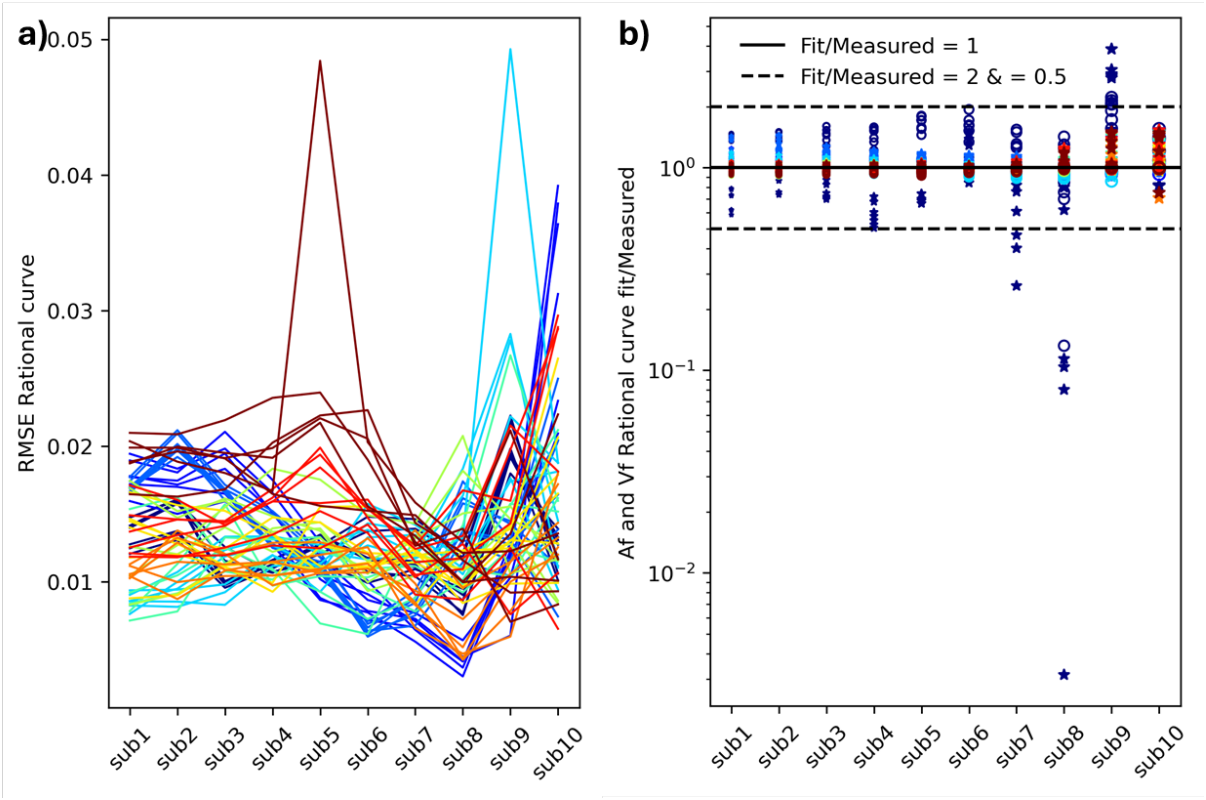

Figure A.59: RMSE values and comparison of fit and measured intertidal area and volume for the annular decreasing sub-sections.

A.8. Full figures annular decreasing basin size

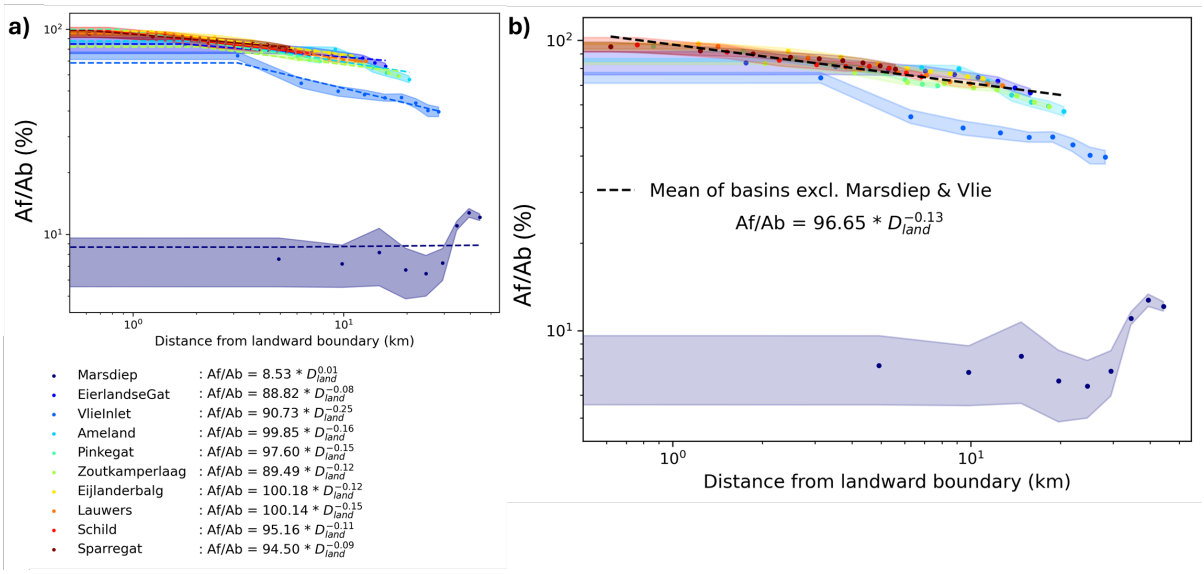

Figure A.60: Relative area of tidal flats as a function as a function of distance from the landward boundary for the annular decreasing basin sections. Temporally averaged for 1985-2022, shaded regions indicate standard deviations in time.

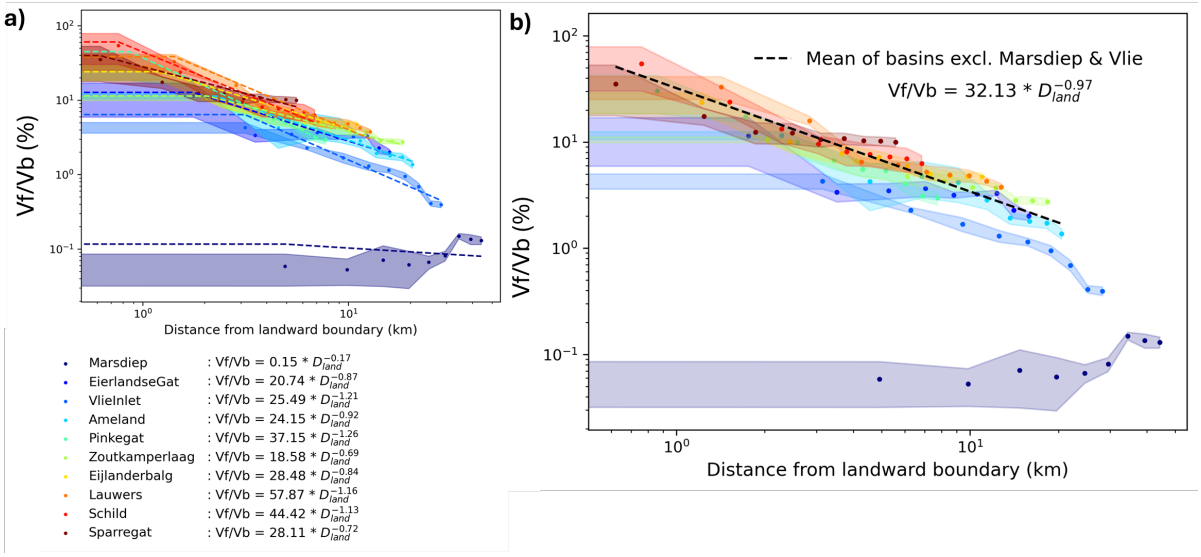

Figure A.61: Relative volume of tidal flats as a function as a function of distance from the landward boundary for the annular decreasing basin sections. Temporally averaged for 1985-2022, shaded regions indicate standard deviations in time.

A.9. Strahler curve Ems-Dollard sub-sections

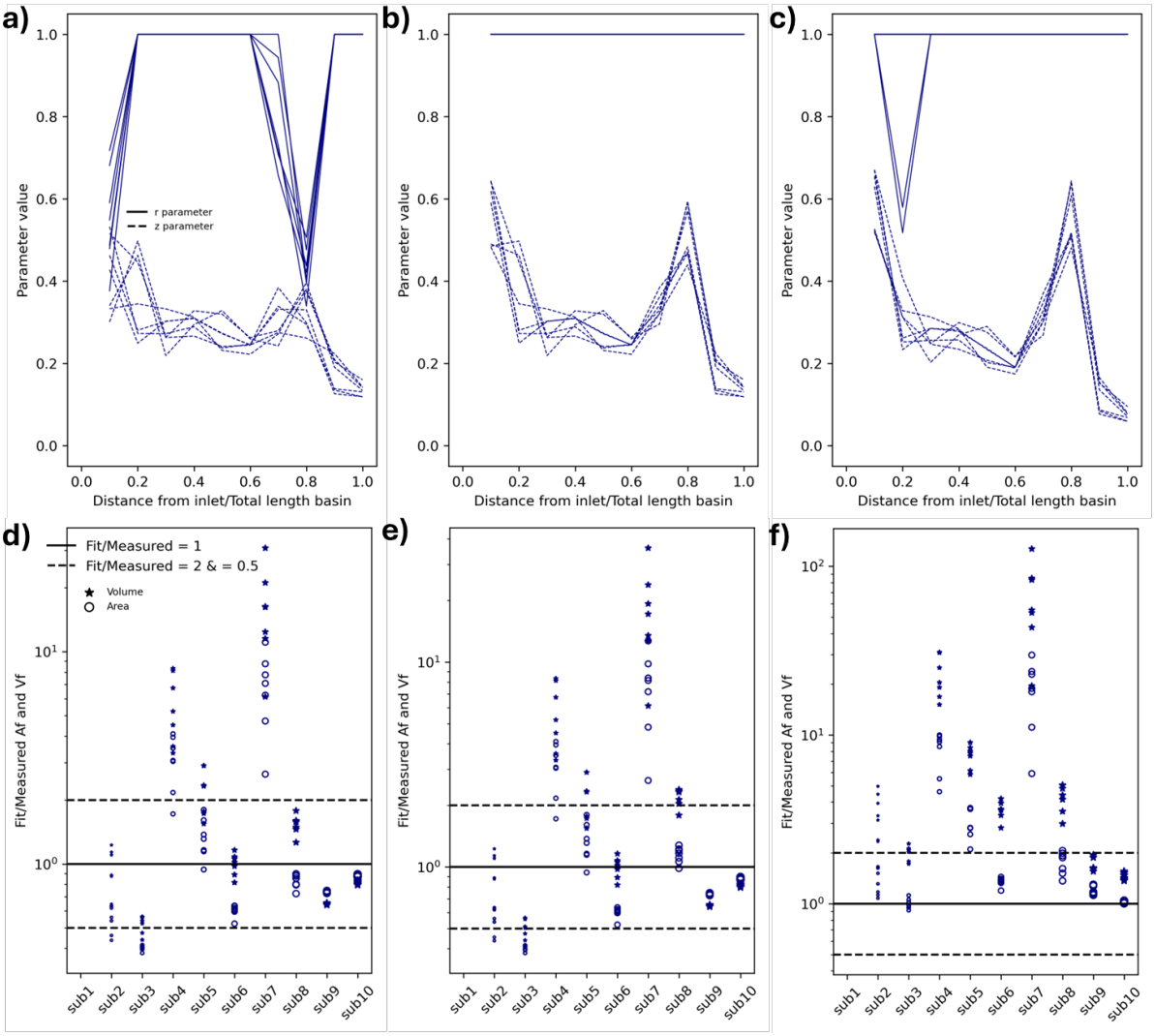

Figure A.62: Fitting results of the Strahler curve on the annular sub-sections of the Ems-Dollard estuary with free parameters (a), with constant r=1 (b), and inverse version as in Leuven et al. (2018).

B. Appendix

B.1. Package sources and description

List of packages used:

- os (Van Rossum, 2020)
- numpy (Harris et al., 2020)
- matplotlib (Hunter & Dale, 2007)
- gdal (GDAL/OGR contributors, 2024)
- rioxarray (GitHub, 2024)
- rasterio(.merge) (Gillies, 2019)
- pandas (McKinney & Team, 2015)
- scipy (Virtanen et al., 2020)
  - optimize.curve_fit
    - This function uses the Levenberg-Marquardt optimization algorithm for nonlinear least-squares fitting (Farber, 2011).
  - interpolate.interp1d
  - integrate.simps
    - Integrates y(x), using composite Simpson's rule.
- sklearn (Pedregosa et al., 2011)
- seaborn (Waskom, 2021)
- cartopy (Met Office, 2010 - 2015)
- math (Van Rossum, 2020)
- tempfile (Van Rossum, 2020)
- dask.array (Dask Development Team, 2016)